Experimental Study of Shock-train/Combustion Coupling and Flame Dynamics in a Heated Supersonic Flow

by

Matthew Leonard Fotia

A dissertation submitted in partial fulfillment
of the requirements for the degree of
Doctor of Philosophy
(Aerospace Engineering)
in The University of Michigan
2012

Doctoral Committee:

    Professor James F. Driscoll, Chair
    Professor Arvind Atreya
    Professor Margaret S. Wooldridge
    Associate Professor Luis P. Bernal

For Kristine and Violet,
I am here only because of their love.

ACKNOWLEDGEMENTS

TABLE OF CONTENTS

LIST OF FIGURES

Figure

LIST OF TABLES

Table

LIST OF APPENDICES

Appendix

NOMENCLATURE

Symbols

A	Cross-sectional Area
C_p	Specific Heat at Constant Pressure
D	Hydraulic Diameter of Duct
f	Frequency
H	Duct Height ($= 25.4$ mm)
h	Duct Half-height ($= H/2$)
L	Length
M	Mach Number
$\dot{m}$	Mass Flow-rate
P	Pressure
Pr	Prandtl Number
r	Fuel-jet Momentum Ratio
$\mathfrak{r}$	Recovery Factor
Re_θ	Reynolds Number based on Boundary-Layer Momentum Thickness
St	Strouhal Number
T	Temperature
u	Flow Velocity
w	Crocco Number ($= u/\sqrt{2C_pT_o}$)
w^*	Crocco Number at Sonic Condition ($= \sqrt{(\gamma - 1)/(\gamma + 1)}$)
x	Distance from Pseudo-shock Entrance or Axial Position

Greek

δ	Boundary-layer Thickness
δ^*	Boundary-layer Displacement Thickness
δ_T	Thermal Boundary-layer Thickness
γ	Ratio of Specific Heats
ϕ	Equivalence Ratio of Hydrogen and Oxygen
θ	Boundary-Layer Momentum Thickness

Subscript

1	Pseudo-shock Entrance Condition
2	Pseudo-shock Exit Condition
aw	Adiabatic Wall Condition
e	External Flow
F	Fuel-jet
I	Isolator Flow
o	Stagnation Value
u	Velocity Value
w	Wall Condition
∞	External Flight Condition

Superscript

$'$	Supersonic Core Value

CHAPTER I

Introduction

1.1 Dual-mode Scramjet Background

1.1.1 Isolator/Combustion Interactions and Pseudo-shock Behavior

Interest in the formation and behavior of shock-trains, and the pseudo-shock phenomena, has been persistent since the mid-1950's. As can be imagined, there are many instances in which a supersonic flow may become confined within a duct. Some examples are supersonic wind-tunnel diffusers and aircraft engine inlets.

However, much of the previous work has been performed using room temperature air and mechanical valves to create the back-pressure that produces the shock-trains. Matsuo et al. [29] provides a comprehensive review of many of these studies. For most of the potential applications this approach is suitable to accurately recreate the behavior of the pseudo-shock, which is defined to be the complete shock-train and subsequent pressure rise that is due to boundary-layer growth downstream of the shocks [38].

Only a few previous studies have considered isolator/combustor interactions for realistically heated airflows. The work presented here examines the coupling between the combustor and isolator sections in such devices. Bement et al. [1] studied an isolator with a downstream combustor at a stagnation temperature of 1028 K and duct flow Mach number of 2.2. A Pitot rake was used to characterize the flow profile across the isolator section. They found that their results compared favorably to those estimated by the experimental

1

correlation offered by Waltrup and Billig [49, 50]. Dessornes and Scherrer [12] examined the behavior of the JAPHAR dual mode ramjet engine under different forward/aft fuel scheduling conditions, making pressure field comparisons to computational results. Le et al. [28] examined the pressure response of an isolator shock-train to various fueling conditions, offering both a time-resolved temporal and frequency analysis of the unsteadiness present.

The current work focuses on the isolator/combustor interactions in a preheated airflow, which are more complex than isolator performance with a mechanical back pressure valve. A realistic hydrogen jet in a cross-flow provides the downstream combustion. To provide an adequate description of this coupled behavior, a new concept is proposed that explains the back pressure in terms of a fluid-mechanical blockage and a combustion-induced blockage. It has been found that by making this distinction an operating point approach can be used to describe the behavior of the interdependent isolator/combustor system. Assessments are made to determine the applicability of pseudo-shock models to the heated combustion induced case specific to the ramjet application.

The heated flow creates a challenging environment in which to characterize the behavior of such a complex and dynamic flow field. Optical access to the complete test-section can be limited by structural concerns. The difficulties associated with the use of seeding materials, as with techniques such as laser Dopper velocimetry, can be amplified so that their use can be ruled-out entirely. The influence of isolator geometry on the behavior of the pseudo-shock has been difficult to quantify. The coupling between the fuel injector operation and the response of the isolator is a key relationship that must be explored to better understand the influence of inlet conditions, isolator geometry and fuel injector design on the global operating point performance of a system.

The isolator/combustor interaction can be explained by simple gas dynamics equations.

During ram-mode operation of a dual-mode scramjet the combustor exit becomes thermally choked, so any increase in the fuel flow rate lowers the (subsonic) Mach number at the entrance to the combustor, and it also raises the static pressure at this location. Thus the low density burned gas can be considered to be a blockage to the subsonic flow field. The added mass of the fuel-jet acts as a blockage which also causes an increase in the pressure at the combustor entrance. Consider the gas dynamics equations of a constant area combustor in which the rise in stagnation temperature, dT_o/dx, in the x-direction is known. The mass flow-rate rise, $d\dot{m}/dx$, due to fuel addition also is known. Neglecting heat transfer and drag, Shapiro [46] shows that

$$(1.1) \qquad \frac{1}{M^2}\frac{dM^2}{dx} = \frac{1+\gamma M^2}{1-M^2}\frac{1}{T_o}\frac{dT_o}{dx} + \frac{2\left(1+\gamma M^2\right)\left(1+\frac{\gamma-1}{2}M^2\right)}{1-M^2}\frac{1}{\dot{m}}\frac{d\dot{m}}{dx}.$$

All terms on the right side of this equation are positive since the Mach number in the combustor is less than unity in the ram-mode. Thus adding more heat or more mass will cause the slope dM^2/dx to increase. Since $M = 1$ at the combustor exit, it follows that heat or mass addition must decrease the Mach number at the combustor entrance. The analysis of Heiser and Pratt [18] shows that the isolator static pressure ratio, P_2/P_1, will increase if the Mach number at the isolator exit, M_2, decreases, according to

$$(1.2) \qquad \frac{P_2}{P_1} = 1 + \gamma M_1^2 - \gamma M_1 M_2 \sqrt{\frac{1+\frac{\gamma-1}{2}M_1^2}{1+\frac{\gamma-1}{2}M_2^2}}.$$

The pseudo shock therefore is strengthened by increasing either the heat or the mass addition, since this forces M_2 to decrease and this increases the isolator pressure ratio, P_2/P_1. In reality there is an additional pressure rise and an additional blockage that is due to the three-dimensional nature of the fuel-jet. A wake region is formed behind the fuel-jet and the jet momentum deflects the local streamlines upward.

1.1.2 Ram-Scram Mode Transition and Flame/Shock-train Interaction

The motivation for this work is the fact that a ram-scram transition will occur at some time during the ascent of a hypersonic vehicle that is powered by a dual-mode propulsion system. During this transition the downstream boundary condition will abruptly change from a thermally choked condition, which always occurs in the ram-mode, to the unchoked flow which always occurs in the scram-mode. The ram-scram transition will cause a change in the wall static pressure profile. This causes a corresponding abrupt change in the thrust force and the moments on the vehicle that may result in loss of vehicle control. Therefore the ram-scram transition is an important and challenging research area. Previously, researchers have examined the isolator separately, by replacing the flame with a downstream valve [6, 7, 8, 39, 40, 50], or the flame separately, by studying a fuel-jet burning in a cross-flow [2, 16, 17, 42].

Many of the topics that have been considered by others involve single components of the combustor under steady conditions. Only a few previous studies have considered the interactions that involve both a shock-train and a downstream combustor that is thermally choked, including; Chun et al. [9], Rocci Denis and Kau [11], Kanda et al. [26] and Goyne et al. [14]. Chun et al. [9] used pressure measurements and images of chemiluminescence to examine the conversion between weak and strong instances of combustion in a scramjet engine. The method of fuel injection into the combustor is an active area of research, with many configurations being evaluated. Rocci Denis and Kau [11] evaluated the operational behavior of an in-flow wedge-injector and strut flameholder. They observed the effects of the physical blockage due to the injector on the system through pressure measurements. The impact of the position of fuel injection within a scramjet device was examined by Kanda et al. [26]. They found that by injecting fuel into the divergent section of the device the maximum static pressure recovered in the device could be lowered, while shift-

ing the location of the combustor pressure rise downstream. These previous studies only considered steady conditions and not the dynamics.

The computer simulation of scramjet devices has been approached by many. Goyne et al. [14] provides a comparison of one such simulation attempt to experimental results. Using silicon dioxide particles to image the fuel plume from a ramp injector. It was found that the computational code examined could adequately predict the non-reacting fluid mechanics, but not parameters such as fuel plume size, penetration, shape and axial growth under reacting conditions. In his review paper, Billig [4] discusses many of the other investigations that have been undertaken in the area of supersonic combustion.

A brief evaluation of the simulation capabilities of two commercially available computational fluid dynamics software packages has been provided in Appendix A. The strengths and weaknesses of both Ansys Fluent [24] and Metacomp CFD++ [33] are discussed.

Heltsley et al. [19] conducted a fundamental study where the behavior of a hydrogen fuel-jet is examined in an expansion tube experiment. Jet-to-freestream momentum-flux and cross-flow stagnation temperature are used to describe the regimes in which stable, unstable or non-combusting behavior of the fuel-jet is observed. They found that an increase in jet-to-freestream momentum-flux ratio tends to increase combustion stability, while increasing static temperature tends to slightly decrease combustion stability. The presence of autoignition in such devices was studied by Kanda et al. [27] as a function of fuel equivalence ratio, stagnation temperature and stagnation pressure. The effects of flow-transverse and flow-parallel hydrogen fuel injection was studied in a water-cooled combustor with a backward-facing step flame stabilizer.

Some relevant research issues are the following. How much does the axial wall static pressure profile change at transition due to the abrupt change in the downstream boundary condition from choked to unchoked flow? What is the measured ram-scram transition

boundary? Transition is normally caused by either increasing the free-stream stagnation conditions, both temperature and pressure, which occurs during accelerating flight, or by decreasing the fuel-air equivalence ratio, ϕ. A decrease in equivalence ratio reduces the effective blockage caused by combustion and unchokes the flow. The plot of equivalence ratio versus stagnation temperature at the transition boundary defines the regime boundary and was measured in the present work. Can other factors cause a transition? Changes in the wall temperature were found to be sufficient to cause an unexpected transition. Images were recorded to show the shock wave pattern in the combustor as the shock train is pushed downstream during the transition. A final issue involves the dynamics; if the flame position oscillates when the downstream flow is thermally choked, these flame oscillations will force pressure waves to travel upstream through the wall boundary-layer and cause oscillations in the strength and location of the upstream shock-train. Measurements of these dynamics are needed to understand the relevant time scales, phase differences and the correlation between flame and shock dynamics. The source of the low frequency flame oscillations is a research issue that was also investigated.

To understand the measurements presented in the next sections, the physical process is briefly reviewed using the low-order model of Torrez et al. [47]. Consider heat added by combustion to a duct that has a diverging area, such that dA/dx is positive. Shapiro [46] shows that the Mach number, M, varies according to

$$(1.3) \qquad \frac{1}{M^2}\frac{dM^2}{dx} = -\frac{2\left(1 + \frac{\gamma-1}{2}M^2\right)}{1 - M^2}\frac{1}{A}\frac{dA}{dx} + \frac{\left(1 + \gamma M^2\right)\left(1 + \frac{\gamma-1}{2}M^2\right)}{(1 - M^2)}\frac{1}{T_o}\frac{dT_o}{dx},$$

where the stagnation temperature gradient, dT_o/dx, is determined by the heat release rate of the flame. For this simple explanation we do not consider wall friction or mass addition and assume that the gas consists of a single species that is calorically perfect. The above equation is seen to have a singularity at any location where the Mach number approaches unity. Shapiro applies L'Hospital's rule to Equation 1.3 to show that thermal choking

occurs at the x-location, denoted x_c, where

(1.4)
$$\frac{1}{A}\frac{dA}{dx}\bigg|_{x=x_c} = \frac{1+\gamma}{2}\frac{1}{T_o}\frac{dT_o}{dx}\bigg|_{x=x_c}.$$

After using Equation 1.4 to determine the location of the downstream thermal choking location, Equation 1.3 then can be solved in the negative x-direction to determine the Mach number profile, M(x), in the combustor. Location 1 is the entrance to the isolator, and 2 is the entrance to the combustor. The solution to Equation 1.4 determines the Mach number, M_2, at the inlet to the combustor. In the isolator section, the low-order model of Heiser and Pratt [18] can be used to determine the pressure recovered, $(P_2 - P_1)/P_o$, across the isolator, which is predicted to be:

(1.5)
$$\frac{P_2 - P_1}{P_o} = \frac{\gamma M_1^2 - \gamma M_1 M_2 \left(\frac{1+\frac{\gamma-1}{2}M_1^2}{1+\frac{\gamma-1}{2}M_2^2}\right)^{1/2}}{\left(1+\frac{\gamma-1}{2}M_1^2\right)^{\frac{\gamma}{\gamma-1}}}.$$

The isolator model of Heiser and Pratt assumes that the isolator flow consists of a central core that contains a shock-train, and a surrounding boundary-layer. Conservation equations for mass and momentum are applied to each region. To compute P_2 the value of M_2 is inserted into Equation 1.5 that was determined from Equations 1.3 and 1.4, as stated above. The values of M_1 and P_1 also are known; they are determined from the upstream conditions (flight Mach number, altitude and the strengths of the inlet shocks). Once P_2 is computed from Equation 1.5, the entire pressure profile downstream in the combustor is computed by solving

(1.6)
$$\frac{1}{P}\frac{dP}{dx} = \frac{\gamma M^2}{1-M^2}\frac{1}{A}\frac{dA}{dx} - \frac{\gamma M^2 \left(1+\frac{\gamma-1}{2}M^2\right)}{1-M^2}\frac{1}{T_o}\frac{dT_o}{dx}.$$

The low-order model of Torrez et al. is based on the above concepts but it includes real gas mixtures and finite-rate combustion chemistry. Instead of solving the simple equations 1.3, 1.4 and 1.6, it replaces them with equations that represent the conservation of mass, momentum, energy and individual species, and an equation of state. It considers hydrogen

or ethylene fuel combustion involving 15 species and 22 reactions. It also includes heat transfer to walls, frictional losses and mass addition by the fuel-jet. Some results of the model are reported by Torrez et al.. The model will be used to help to explain the present measurements.

CHAPTER II

Experimental Facilities

2.1 University of Michigan Dual-mode Combustor Experiment

The University of Michigan Dual-mode Combustor (MDMC) experiment was used to obtain the current set of results. The experiment allows for the examination of the internal flows of a supersonic isolator coupled to a cavity-stabilized combustor, with wall-normal fuel injection. The inlet air can be heated to stagnation temperatures between 1050-1450 K through a combination of a 250 kW electric resistance heater and H_2-O_2 combustion. Additional Oxygen was injected to maintain a 0.21 O_2 mole fraction in the heated products, with the mole fraction of H_2O varying between 0.12-0.18. The air enters the isolator section of the experiment at a Mach number of 2.2. This enables the experiment to operate under both ram- and scram-jet combustion modes with equivalence ratios between 0 - 0.42. A schematic of the experiment can be found in Figure 2.1.
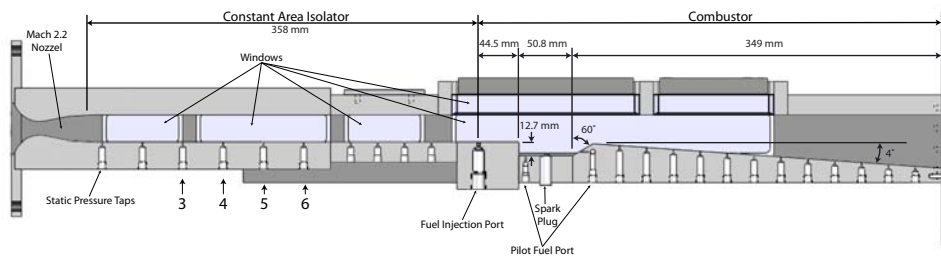
Figure 2.1: Schematic of the University of Michigan Dual-mode Combustor experiment. Static pressure tap locations 3 through 6 are labeled.

The MDMC is constructed of stainless steel and inconel alloys. The pre-combustion section consists of a planar inlet nozzle to accelerate the inlet gases and a constant area isolator of 25.4 mm (height) x 38.1 mm (width) cross-section. The combustor section includes a wall-normal fuel injector, cavity flame-holder with angled rear wall, and a $4°$ diverging combustor exit. The fuel injector is choked to provide injection at sonic conditions. The experiment is not water cooled, limiting the run time to 15 seconds. This allows for 4 seconds of data acquisition time after the establishment of steady flow behavior. The design methodology used in the construction of the test-section is detailed by Micka [34].

There are two major alterations that were made to the test-section described by Micka. The first is the addition of a set of mid-isolator viewports to allow for more convenient imaging of the leading edge of the isolator pseudo-shock. Detailed drawings of these alterations, including window blank dimensions, can be found in Appendix B. These alterations were machined by Apex Manufacturing L.L.C. of Clinton, Michigan.

The second alteration was the change in the angle of the rear wall of the cavity. This was done to mitigate excessive heating due to the stagnation of the flow at the rear cavity-wall location. In the original design a right-angled rear wall was used. The excessive heat transfer to the lip of the cavity due to flow stagnation resulted in material degradation and the propagation of stress fractures into the steel component.

Gruber [15] provides a thorough discussion of the merits of various cavity configurations. A 60° down-sweep of the rear wall was chosen to balance two requirements. One was to allow for the formation of as large a primary recirculation zone within the cavity as possible when compared to any secondary recirculation zones that may also be present. According to Gruber, this provides the largest interchange of mass between the cavity and core flow, and better circumstances for flame stabilization. The second requirement was the need to be able to install any altered geometry into the pre-existing test-section, with

a minimum of alteration and the dimensional limitations this created. The new geometry was found to greatly reduce the heating loads subjected to the cavity lip, and mitigate the issues surrounding excessive heating.

The MDMC is installed in the University of Michigan Supersonic Combustion Laboratory, which was designed to allow the study of dual-mode scramjet combustion at flight inlet conditions of up to a flight Mach number of 6.5. A schematic of the laboratory is provided in Figure 2.2. A blow-down system configuration is used, in which an Ingersoll Rand compressor pressurizes building-external air tanks up to 13.8 MPa. The high-pressure air is fed into the laboratory and regulated by a dome-valve. The air is then heated by a 250 kW Hynes electric heater and a hydrogen-oxygen vitiator. The vitiator was added to the laboratory by Micka [34] for his work, while previous studies conducted in the laboratory by Yoon [52], Huh [21], Bryant [5], Nakagawa [37] and Rasmussen [41] made use of only the electric heater, achieving air stagnation temperatures up to 800 K. The products of the experiment are removed from the building through a dedicated exhaust. An operational checklist for the experiment is provided in Appendix C.

The operation of the laboratory is controlled through a Labview program and a National Instruments 6229 data acquisition card. The timings used for the various fuel, oxidizer and spark ignition signals are shown in Figure 2.3. The vitiator was operated for 7 seconds prior to the injection of fuel into the test-section to allow for the establishment of steady flow behavior. This allowed for 4 seconds of observations to be made before requiring the heating elements to be turned off to reduce thermal damage to the uncooled heat-sink test-section. The inlet air flow was maintained between runs to provide active cooling to the experiment.

The vitiated air heater is capable of supplying the test-section with air heated up to 1500 K. This upper limit is due to material degradation concerns, in particular the softer, sili-
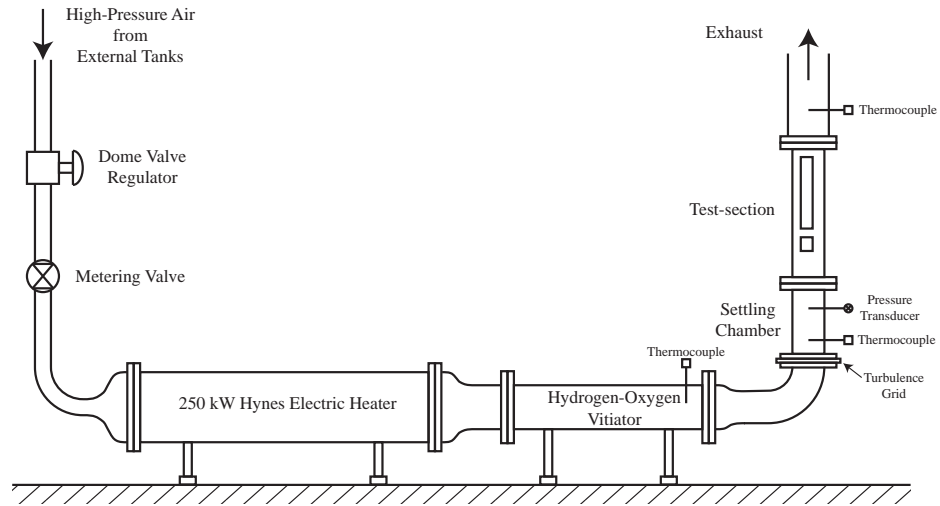
Figure 2.2: Michigan Supersonic Combustion Laboratoty experimental facilities layout.
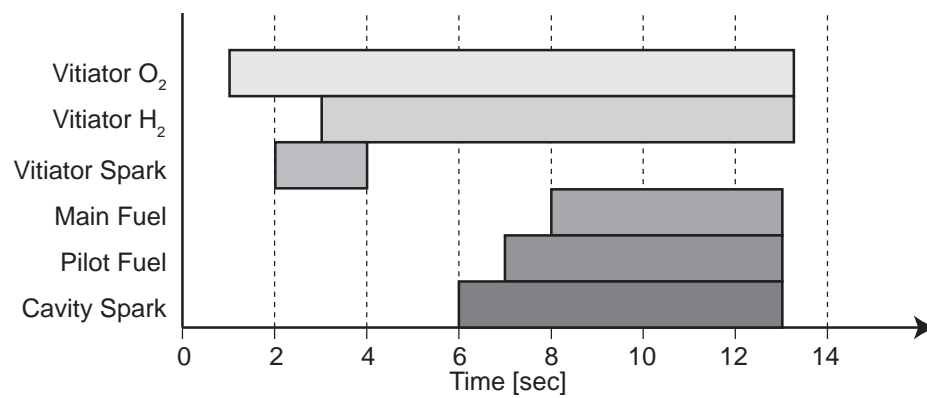
Figure 2.3: Fuel, oxidizer and spark ignition timing diagram for a test run of the Michigan Dual-mode Combustor experiment.
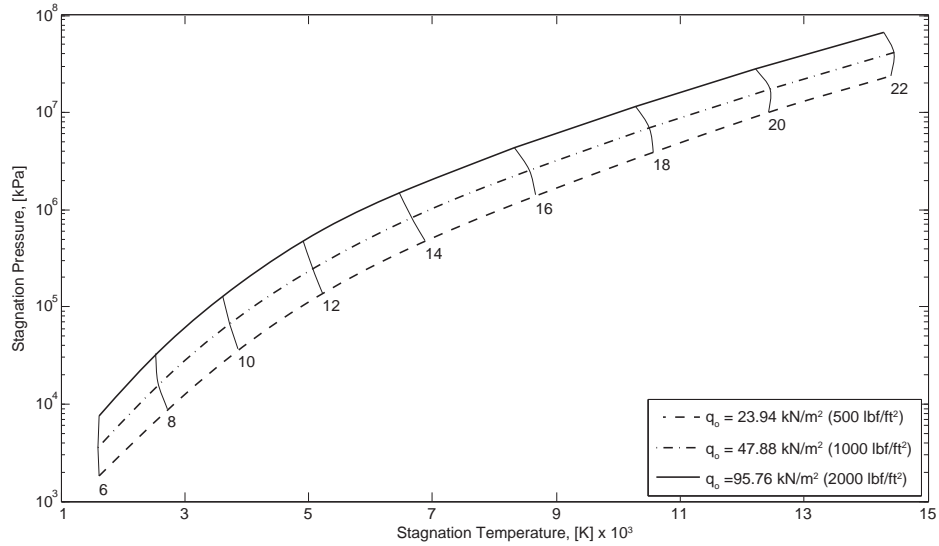
Figure 2.4: Free-stream stagnation conditions as a function of flight Mach number [18].

cone sealants used between the stainless steel test-section components. On one occasion a voltage spike, caused by a solenoid failure, locked-up the laboratory control computer while the feed lines were operating. The thermal limits of the silicone sealant between the flange and test-section inlet nozzle were exceeded and a small fire ensued. This is the location of maximum stagnation heating loads within the experiment. A brief news article on this event is included in Appendix D.

In the case of an actual flight vehicle, the deceleration of the external air flow will create a particular stagnation temperature, T_o, and stagnation pressure, P_o, condition. For a vehicle trajectory of a specific dynamic pressure, $q_o = \frac{1}{2}\rho_\infty u_\infty^2$, the stagnation conditions recovered are a function of flight Mach number. Figure 2.4 shows this relationship.

The current test-section is designed to operate below stagnation pressure conditions of 700 kPa. This, coupled with the limit on stagnation temperature, creates a range of flight conditions just below the lower left-hand corner of Figure 2.4 which can be readily simulated in the laboratory. The Laboratory can simulate flight Mach numbers as high as approximately 6.5, on a dynamic pressure trajectory of 10 kN/m^3.

Table 2.1: Pressure transducers: Uses, ranges & errors

Transducer	Quant.	Pressure Range	Error	Manufacturer	Part #
		psig	% F.S.		
Settling Chamber	1	-14.7-100	0.1%	Cooper Instr.	PTG-404-B-100-P-3-D
Vitiator Fuel	1	-14.7-500	0.25%	Cooper Instr.	PTG-403-B-500-P-3-D
Test-section Pilot Fuel	1	-14.7-200	0.25%	Cooper Instr.	PTG-404-B-200-P-3-D-O
Test-section Main Fuel	1	-14.7-200	0.1%	Cooper Instr.	PTG-404-B-200-P-3-D
Test-section Static Ports	16	-14.7-50	0.25%	Cooper Instr.	PTG-403-B-0050-P-3-A-O

2.2 Diagnostics

2.2.1 Pressure Measurements

Static pressure measurements were used to characterize the behavior of many aspects of the experiment. Table 2.1 provides a breakdown of the pressure transducers used to collect the pressure data from various location in the experimental set-up. All of the transducers were manufactured by Cooper Instruments. An in-house calibration check was performed on each to verify proper behavior prior to use. In all cases, the voltages supplied from the transducers were recorded using the National Instruments PCI-6229 data acquisition card installed in the experimental control computer.

The physical locations of the test-section static pressure taps are given in Figure 2.1, while the settling chamber transducer location in indicated in Figure 2.2. The relative locations of the other transducers, with respect to the various flow control components, are provided in Appendix E.

2.2.2 Temperature Measurements

During operation of the experiment, the internal gas temperature is monitored in three locations using K-type thermocouples. The information was recorded using a National Instruments 9211 data acquisition device, with a USB interface to the experimental control

Table 2.2: Thermocouples: Uses, ranges & errors

Thermocouple	Max. Temp.	Calibration	Error	Manufacturer
	K		% F.S.	Part #
Vitiator Exit	1610	K Type	$\pm$ 2.5% for 233-648 K $\pm$ (0.0075 x (T-273.15) for 648-1475 K	Omega Engin. Inc. KQXL-14G-12
Settling Chamber	1610	K Type	$\pm$ 2.5% for 233-648 K $\pm$ (0.0075 x (T-273.15) for 648-1475 K	Omega Engin. Inc. KMQXL-062G-6
Exhaust	1610	K Type	$\pm$ 2.5% for 233-648 K $\pm$ (0.0075 x (T-273.15) for 648-1475 K	Omega Engin. Inc. KQXL-18G-12
External	2475	8-14 μm IR	$\pm$ (1.0%rdg+1°) for 367-478 K	Extech Instr. Model 42570

computer. The thermocouples are located at the exit of the H_2-O_2 vitiator, in the settling chamber prior to entrance into the test-section nozzle and downstream of the test-section in the exhaust. These locations are also shown in Figure 2.2.

External temperature measurements were taken of the test-section during operation using a infer-red thermometer in the 8-14 μm range. This information was used solely as a basis of comparison for the unsteady modeling of the test-section wall heating, which is discussed in Section 2.2.4.1. Table 2.2 provides a breakdown of the transducers used in the experiment.

2.2.3 Schlieren Imaging

The injection of fuel into the test-section, and its subsequent combustion, creates a back pressure that propagates forward from the combustion section of the experiment. For sufficiently large back pressures the test-section will operate in a ram-jet mode, in which a shock-train is created upstream of the location of fuel injection. Schlieren images of these shocks were captured using an apparatus arranged as shown in Figure 2.5. Settles [45] dis-
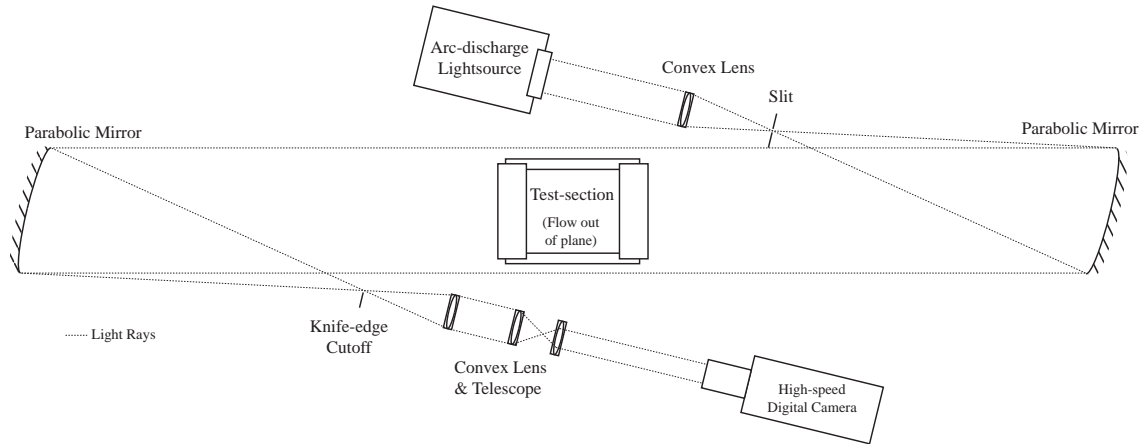
Figure 2.5: Schematic of the Schlieren imaging apparatus.

cusses the relative merits of the various arrangements that have been used in other imaging studies, and provides a good description of the operating principles of such systems.

The apparatus was based on a standard Z-configuration with two wall-mounted and leveled 8 inch. parabolic Aluminum-oxide mirrors with 1.575 m (62 inches) focal lengths. A convex lens was used to focus the strobe light at the focal point of the first mirror, at which a sheet-metal slit was placed to set the area of illumination on the first mirror. The mirror was set at a slight angle to allow the light source to be placed out of the test-section field-of-view. The light was then transferred across the laboratory, and test-section, to the second parabolic mirror which was again offset at a slight angle. The field-of-view of the Schlieren apparatus is shown in Figure 2.6. A knife-edge cutoff was placed at the focal point of the second mirror and can be used to adjust image contrast. A convex lens was used after the knife-edge to pick off the desired image size from the diverging beam, which was then sent through a telescope arrangement to focus the image directly onto the CMOS chip in the high-speed camera.

The light source used to illuminate the test-section was a Perkin Elmer model MVS-2613 flashlamp/strobe system. The light source emits white light and the specifications
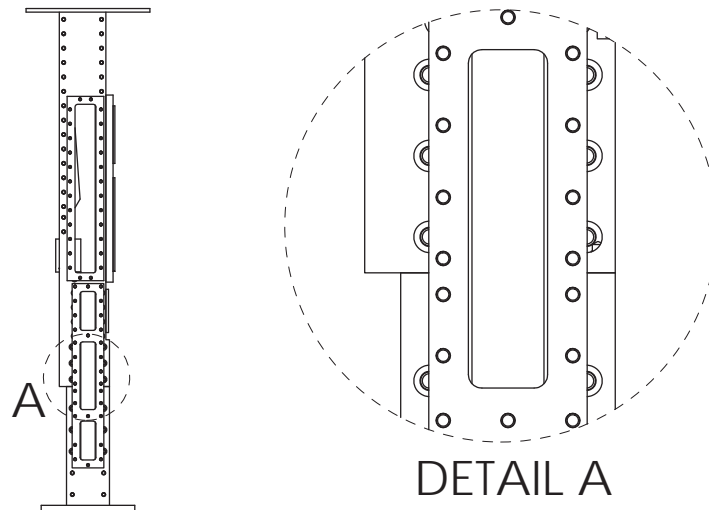
Figure 2.6: Schlieren imaging field-of-view.

state a 1 KHz maximum flash rate with a 0.04 Joule per flash intensity. In practice, the maximum flash rate was found to be approximately 600 Hz and is believed to be due to equipment age and prolonged use. A Stanford Research Systems Inc. DG-535 external time source was used to trigger the system.

A Phantom 9.1v high-speed camera was coupled to the DG-535 time source to allow accurate camera gating relative to the light source strobes. The camera was operated without a mated lens, relying on the telescope in the Schlieren optical train to focus and adjust the image size. Recordings were made at both 100 Hz and 500 Hz, with the exposure set directly at the camera to be 2 μs and a flash duration of the light source of 1 μs. An image resolution of 1632 x 376 pixels was used so that the maximum chip surface area was covered by the image.

2.2.4 Schlieren Boundary-layer Analysis

The light amplitude variations created by the Schlieren technique are due to gradients in the index-of-refraction, n, of the gas inside the test-section, through which the light rays

have passed. These gradients are then proportional to the angular light ray deflection by

$$(2.1) \qquad \epsilon_x = \frac{L}{n_o}\frac{\partial n}{\partial x}, \qquad \epsilon_y = \frac{L}{n_o}\frac{\partial n}{\partial y},$$

where L is the width of the test-section and n_o the base index-of-refraction of the gas. These deflection angles are related to the gas density gradients by $n - 1 = k\rho$, with k being the Gladstone-Dale Coefficient for the gas ($\approx 0.23 cm^3/g$ for air in visible light). The image intensity contrast can then be related back to the density gradients via these deflection angles,

$$(2.2) \qquad \frac{\Delta E}{E} \propto \epsilon_y \propto \frac{\partial \rho}{\partial y},$$

assuming that the knife-edge cut-off has been oriented parallel to the flow direction. The reader is referred to Settles book on this technique for a more complete description [45].

The gradient in density also is proportional to the gradient in static temperature through the ideal gas law. A relative measure of the thermal boundary-layer profile is now attainable. The first quantity that must be identified from this gradient profile is the thickness of the velocity boundary-layer. This can be done by identifying the thickness of the thermal boundary-layer, δ_T, from the Schlieren images, that have been collapsed from a two-dimensional image to a one-dimensional profile of image intensity. As demonstrated in Figure 2.7, the thermal boundary-layer thickness can be identified by the change in the gradient of the temperature profile, or rather the image contrast information as they are proportional. A 25% change in slope was used as a guide to identify the two layers of different slope.

Differing regions of a single image were used to provide a number of estimates of the boundary-layer thickness. This provided several samples from which to describe the statistical error associated with this method of boundary-layer measurement.
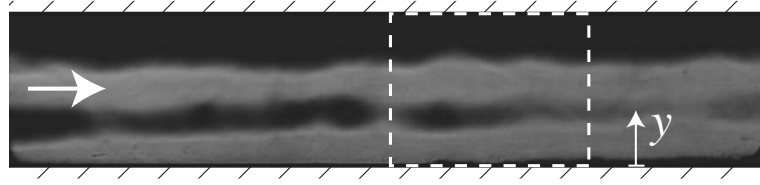
(a) Example of region taken from Schlieren images for boundary-layer thickness calculation.
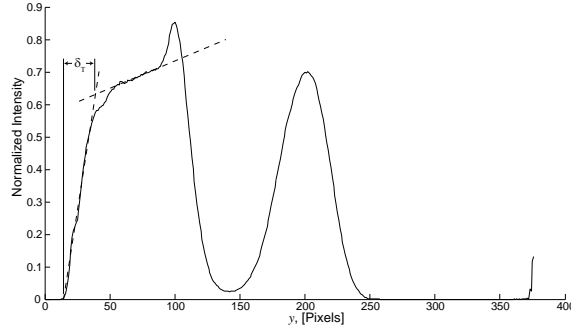
(b) Example of density gradient profile averaged over image region.

Figure 2.7: Example of boundary-layer thickness determination from Schlieren imagery.

The thermal boundary-layer thickness was combined with the Prandtl number, Pr, to obtain an estimate of the velocity boundary-layer thickness, $\delta = \delta_T \cdot Pr^0.4$. The rest of the image contrast information, between the thermal boundary-layer thickness point and the wall, is used to estimate the profile of the velocity distribution in a similar manner.

The integral boundary-layer thicknesses could then be calculated numerically for all instances from

$$(2.3) \qquad \delta^* = \int_0^\delta \left(1 - \frac{\rho u}{\rho_e u_e} \right) dy$$

and

$$(2.4) \qquad \theta = \int_0^\delta \frac{\rho u}{\rho_e u_e} \left(1 - \frac{u}{u_e} \right) dy,$$

noting that these equations require a knowledge of the wall-normal density profile of the flow. An unsteady finite difference model was developed to provide information about the static wall temperature that can be used to reconstruct the density profile. This model is described in Section 2.2.4.1. The results of the boundary-layer thickness calculations are

discussed further in Section 3.4.

2.2.4.1 Unsteady Thermal Model of Wall Heating

A wall-normal density profile is required information if an accurate calculation of the integral boundary-layer thicknesses, Equations 2.3 and 2.4, is to be made. To supply this information an adequate estimate of the interior static wall temperature of the test-section is needed. This measurement is complicated by the harsh thermal environment inside the test-section. The internal gas temperatures are high enough to damage a surface-mounted thermocouple, and rule out direct measurement via infra-red thermometry.

An unsteady finite difference model was created to describe the evolution of heat transfer through the wall of the test-section over the length of a test-section run. The finite difference stencils that were used to create the model are given in Table 2.3, where superscripts denote indices in time and subscripts indices in space. The non-dimensional Biot number is defined as

$$Bi = \frac{h\Delta x}{k},$$

(2.5)

and the Fourier number is

$$Fo = \frac{\alpha\Delta\tau}{(\Delta x)^2},$$

(2.6)

with h being the convective heat transfer coefficient, k the conductive heat transfer coefficient, α the thermal diffusivity, and Δx and $\Delta \tau$ the spacial and temporal step sizes respectively.

It should be noted that the two-dimensional stencil equations in Table 2.3 may be converted to one-dimensional by simply replacing the factor of "4" in each equation with a factor of "2".

Temperature-dependent material properties were implemented in the model to account in part for the high thermal gradients present in the experiment. The Nusselt number of

Table 2.3: Node stencils used for unsteady thermal model of test-section wall.

Stencil	Equation	Stability Requirement
Convection Boundary Node		
	$$T_{m,n}^{p+1} = Fo\left[2Bi\left(T_\infty^p - T_{m,n}^p\right) + 2T_{m-1,n}^p + T_{m,n+1}^p + T_{m,n-1}^p - 4T_{m,n}^p\right] + T_{m,n}^p$$	$Fo\left(2 + Bi\right) \le \frac{1}{2}$
Interior Node		
	$$T_{m,n}^{p+1} = Fo\left[T_{m-1,n}^p + T_{m,n+1}^p + T_{m+1,n}^p + T_{m,n-1}^p - 4T_{m,n}^p\right] + T_{m,n}^p$$	$Fo \le \frac{1}{4}$
Insulated Boundary Node		
	$$T_{m,n}^{p+1} = Fo\left[.T_{m-1,n}^p + T_{m,n+1}^p + T_{m,n-1}^p\right] + \left[1 - 4Fo\right]T_{m,n}^p$$	$Fo \le \frac{1}{4}$

the convective flow inside the test-section was calculated using the empirical relation

$$(2.7) \qquad Nu_{D_H} = \frac{(f/8)\,Re_{D_H}Pr}{1.07 + 12.7\,(f/8)^{1/2}\,(Pr^{2/3} - 1)} \left(\frac{\mu_b}{\mu_w}\right)^n ,$$

where D_H is the hydraulic diameter of the test-section, μ is the dynamic viscosity of the flow, $n = 0$ for gases and all quantities are evaluated at the film temperature, $T_f = (T_w + T_b)/2$, or the average of the static wall and bulk flow temperatures. The friction factor, f, may be obtained from

$$(2.8) \qquad f = (1.82 log_{10} Re_{D_H} - 1.64)^{-2} .$$

For a Prandtl number in the range $0.5 < Pr < 200$ this equation is stated to give 6% accuracy. Much of this material was taken from Holman [20], where a more complete description of heat transfer in a forced-convection environment can be found.

The interior wall was subjected to a convective boundary condition based on the Nusselt number calculation above. The exterior wall, the room temperature heat-sink, was modeled as an insulated surface. This assumption is justified by the relatively short test duration, approximately 4.5 seconds, and the fact that internal static wall temperature is not given sufficient time to completely penetrate the test-section wall.

The interior test-section static wall temperature is estimated through a fixed point iteration in which an initial static wall temperature is guessed, the unsteady evolution of temperature through the test-section wall is modeled and the results used to refine the initial value of the static wall temperature until a desired level of convergence is reached, typically an absolute difference less then 10^{-5}. To satisfy the stability requirements listed in Table 2.3 a total of 100 interior points was used across the test-section wall, and a time step of $4 \cdot 10^{-4}$ seconds.

The model results for a number of test conditions were evaluated by comparing the exterior test-section wall temperature indicated in the model to the actual temperature

obtained from infra-red thermometer measurements taken during operation of the test-section. They were found to agree to within 8.5% and as such there is confidence that the convective and thermal diffusion effects present were being modeled in an appropriate manner to provide a reliable estimation of the isolator inner wall temperature.

2.2.5 Pitot Stagnation Tube

The boundary-layer thicknesses are required to provide a more complete description of the shock phenomena present in the isolator portion of the test-section. These values feed into such analyses as the confining influence of the boundary-layer on the pseudo-shock structure, outlined in Section 3.6, its influence on the physical arrangement of shocks and as a variable used by others to approximate the behavior of the pseudo-shock, discussed further in Section 3.5.

A Schlieren method has been used to obtain estimates of these boundary-layer quantities. In an effort to provide a source of comparison to assess these results, a second method was required to describe the boundary-layer within the isolator of the test-section. The high temperatures and flow speeds within the test-section create a difficult environment to measure such quantities. Some of the more advanced methods for measuring velocity profiles in a flow, such as particle image velocemetry, involve seeding particles into the flow. The behavior of these particles in such a high temperature environment makes such methods very difficult to apply, mostly due to particle clumping and caking onto the interior surfaces of the test-section.

To avoid these prohibitive complications, a simple Pitot stagnation pressure tube was employed to take these measurements. The Pitot tube was mounted to a computer controlled traverse allowing the tube to take measurements across the isolator, at multiple locations, during a single test run. A 1.19 mm (3/64 inch) ASME 316 steel tube, with an inner diameter of 0.069 mm (0.027 inch), was inserted through one of the pre-existing

Figure 2.8: Picture of Pitot stagnation tube apparatus.

static pressure measurement ports in the isolator wall. The stagnation pressure was measured by the same pressure transducer used for the main test-section fuel line. The tube was coated with a high-emissivity coating, Aremco 840-M, to provide a measure of protection from the hot inlet gases. A picture of the Pitot tube is given in Figure 2.8.

The traverse was of the stepper-motor linear translation type, connected to a Velmex 8300 Series motor controller which has the ability to be coupled to the laboratory control computer via a RS-232C port. BASIC scripts were sent to the controller through Labview to control the position of the Pitot tube during testing.

To calculate the Mach number of the flow through the test-section isolator, a ratio of stagnation pressure to static pressure is required. The Pitot tube was used to supply the stagnation pressure while the next-nearest upstream static pressure port was used to supply

the static information. The Rayleigh-Pitot equation, taking the form

$$(2.9) \qquad \frac{P_{oy}}{P_x} = \frac{\left(\frac{\gamma+1}{2} M_x^2\right)^{\frac{\gamma}{\gamma-1}}}{\left(\frac{2\gamma}{\gamma+1} M_x^2 - \frac{\gamma-1}{\gamma+1}\right)^{\frac{1}{\gamma-1}}},$$

can then be used to calculate the Mach number at a particular position in the flow. The ratio of specific heats, γ, was computed from the known amounts of hydrogen and oxygen injected into the vitiator.

A velocity profile can be constructed from this measured Mach number profile only if an adequate temperature profile can be defined. The Crocco-Busemann relation is used to define a suitable static temperature profile across the isolator based on the static wall temperature and the local flow velocity,

$$(2.10) \qquad T = T_w + \frac{T_{aw} - T_w}{u_e} u - \frac{\mathfrak{r}}{2C_p} u^2,$$

where the recovery factor, $\mathfrak{r}$, can be taken to be equal to $Pr^{1/3}$. Making the appropriate substitutions for $u = M\sqrt{\gamma R T}$ and $C_p/R = \gamma(\gamma - 1)$, the velocity distribution as a function of wall temperature and local Mach number takes the form

$$(2.11) \qquad u = \frac{M^2 \gamma R}{2u_e} \left[\frac{(T_{aw} - T_w) + \sqrt{(T_{aw} - T_w) + \frac{4u_e^2 T_w}{M^2 \gamma R}\left(1 + \mathfrak{r}\frac{\gamma-1}{2} M^2\right)}}{1 + \mathfrak{r}\frac{\gamma-1}{2} M^2} \right].$$

As can be seen, the interior static wall temperature is a required parameter in this equation and was found using the unsteady finite difference method described in Section 2.2.4.1. A similar method to that described here was used by Bement et al. [1] to characterize the boundary-layers in the NASA/Langley - Generic High Speed Engine model. An assessment of these measurements is given in Section 3.4.

2.2.6 Shearing Interferometry

A laser interferometry apparatus was used to gain insight into the behavior of the of the main fuel flame during the operation of the test-section. This imaging method allows
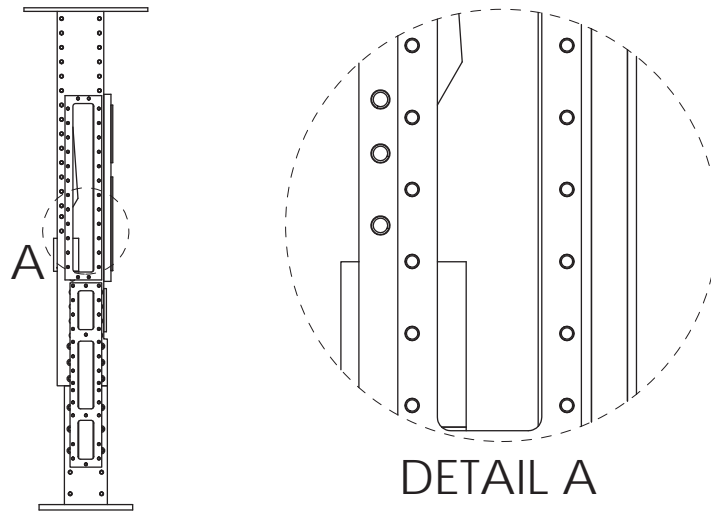
Figure 2.9: Shearing interferometry imaging field-of-view.

for the identification of the mechanism providing flame stabilization within the combustor, as well as the location and behavior of any shock waves that may be present. Figure 2.9 shows the field-of-view of the interferometry apparatus.

The laser interferograms were recorded at 1000 Hz using a Phantom v9.1 high-speed digital camera. A 532 nm ORC-1000 high-speed YAG laser from Clark-MXR Inc. functioned as the coherent light source. The experimental arrangement of the imaging system is given in Figure 2.10 and consists of a Wollaston prism placed between two crossed polarizers. A 532 nm laser line filter is added to remove the chemiluminescence emitted from within the combustor from the image. The images constructed by this apparatus are shearing interferograms. Good descriptions of this process can be found in the texts by Settles [45] and Merzkirch [32] or the articles by Merzkirch [30, 31]. A number of alternative optical arrangements are also discussed in the later Merzkirch paper.

The interferograms allow for the visualization of the phase difference generated between two beams of light due to the presence of a phase object, in this case the flow inside the test-section. The two beams both traverse the test-field where they are sepa-

26
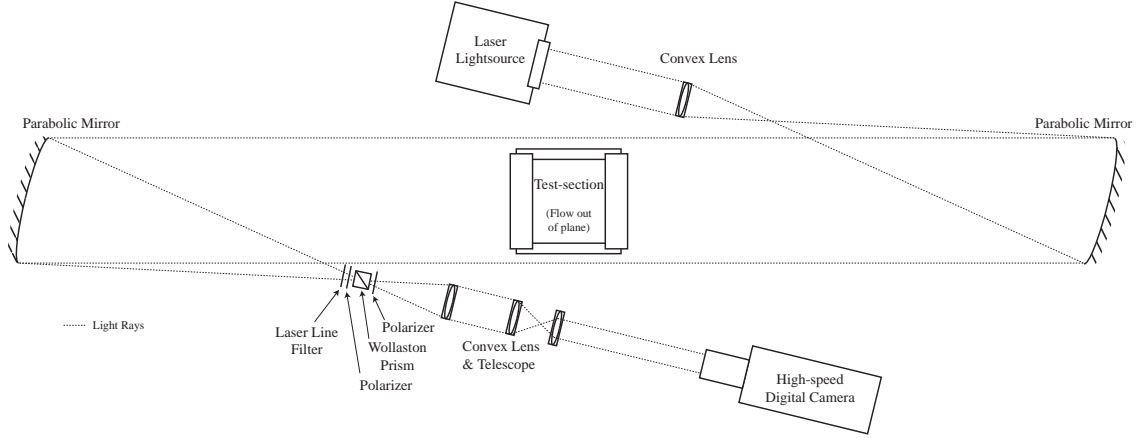
Figure 2.10: Schematic of the shearing interferometry imaging apparatus.

rated, or sheared, by a small distance, d. The interferogram is produced after the beams pass through the interferometer unit and are superposed. If the conjugate rays of the two beams traverse through the test object along different optical pasts, an interference pattern is created in the recording plane.

A ray of light will take an optical path given by

$$(2.12) \qquad l = \int_{\zeta}^{\zeta'} n(x,y,z)dz$$

through the test-section, where $n = n(x,y,z)$ described the spatial distribution of the refractive index in the test-section, and the test-object is confined by the planes $\zeta(x,y)$ and $\zeta'(x,y)$. If the two rays traverse through the test-field in a plane $y = \text{Const.}$, and at positions $x + (d/2)$ and $x - (d/2)$, the optical path length different becomes

$$(2.13) \qquad \Delta l = \int_{\zeta_1}^{\zeta_1'} n\left(x + \frac{d}{2}, y, z\right) dz - \int_{\zeta_2}^{\zeta_2'} n\left(x - \frac{d}{2}, y, z\right) dz$$

$$(2.14) \qquad \approx \int_{\zeta}^{\zeta'} \left[n\left(x + \frac{d}{2}, y, z\right) - n\left(x - \frac{d}{2}, y, z\right)\right] dz.$$

The second line above can be written as the shearing distance, d, is assumed to be small.

Expanding this as a Taylor series, keeping only the linear terms, yields

$$(2.15) \qquad \Delta l = d \int_{\zeta}^{\zeta'} \frac{\partial n(x, y, z)}{\partial x} dz$$

$$(2.16) \qquad = kd \int_{\zeta}^{\zeta'} \frac{\partial \rho(x, y, z)}{\partial x} dz,$$

once the Gladstone-Dale formula, $n - 1 = k\rho$, has been used to relate the refractive index to the gas density. k is the Gladstone-Dale constant specific to the gas in question, and in strict terms is also a function of temperature. This optical path length difference is then related to a phase difference between the two rays of

$$(2.17) \qquad \phi = \frac{2\pi}{\lambda} \Delta l,$$

given an incident plane wave of light to the test-section of wavelength λ.

The two rays of light can be described in terms of their electric fields as

$$(2.18) \qquad E_1 = E_o \sin(\omega t)$$

$$(2.19) \qquad E_2 = E_o \sin(\omega t + \phi),$$

where ω is the angular frequency of the waves and E_o the amplitude. The superposition of these fields gives

$$(2.20) \qquad E = E_1 + E_2 = E_o (\sin(\omega t) + \sin(\omega t + \phi))$$

$$(2.21) \qquad = 2E_o \cos \frac{1}{2}\phi,$$

which is expressed as an intensity via

$$(2.22) \qquad I = \frac{1}{c\mu_o} E_{rms}^2 = \frac{1}{c\mu_o} \frac{E^2}{\sqrt{2}},$$

with μ_o being the permeability of vacuum and c the speed of light. This provides an
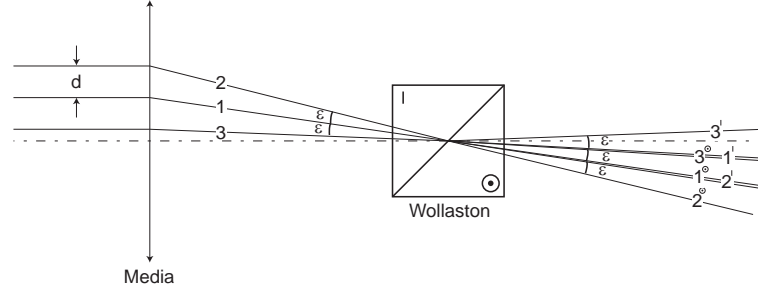
Figure 2.11: Principle of the Wollaston crystal [30].

intensity contrast ratio of

$$(2.23) \qquad \frac{I}{I_o} = \frac{E^2}{E_o^2} = 4\cos^2\frac{1}{2}\phi$$

$$(2.24) \qquad = 4\cos^2\left(\frac{\pi K d}{\lambda}\int_\zeta^{\zeta'}\frac{\partial\rho(x,y,z)}{\partial x}dz\right)$$

in the recorded image.

A Wollaston crystal, sometimes called a prism, is used in the current work to create the superposition of light rays. Figure 2.11 shows the principle behind the prism. Ray 1 is separated by the Wollaston prism into two polarized rays, $1^|$ and $1^\odot$, forming an angle ϵ with each other. The symbols $|$ and $\odot$ indicate the polarization directions in the plane and perpendicular to the plane of the figure, respectively. Ray 2 undergoes a similar separation process. Ray $2^|$ coincides with $1^\odot$, allowing both rays to interfere, provided they have equal direction of polarization. This condition is met by the addition of a polarizer, post Wollaston prism. The procedure is repeated for the other coincident rays exiting the prism, i.e. rays $1^|$ and $3^\odot$, etc.

In the preceding description it was assumed that each ray passed through the center of the crystal. This arrangement produces the effect of a constant illuminated background in the recorded images, or what is called an infinity fringe width adjustment. A finite fringe width adjustment is also possible, where the crystal is purposely positioned aft of the focal point of the incident light rays. This produces a set of finite width fringes that, based on

the known crystal offset, can be used to quantitatively investigate the properties of the gas flow. The reader is referred to the three Merzkirch references for a more complete description of this arrangement [30, 31, 32].

The apparatus takes a similar form as the Schlieren system in Section 2.2.3, with only two major alterations. The first is the replacement of the arc-discharge light source with the high-speed laser source, while the second is the replacement of the knife-edge cutoff with the interferometry unit consisting of the polarizers, Wollaston crystal and laser-line filter. As with the earlier Schlieren system, the images are projected directly onto the CMOS imaging chip of the camera without the use of a camera lens.

Since the intensity contrast in the recorded image is proportional to the gradient of the gas density in the test-section, the laser interferometry technique will register any disturbance in the flow field that creates density grandients. Through the ideal gas law,

$$(2.25) \qquad \frac{\partial \rho}{\partial x} = \frac{1}{RT} \frac{\partial P}{\partial x} + \frac{\rho}{T} \frac{\partial T}{\partial x}$$

and any pressure and temperature variations within the field-off-view will be visible in the resulting image. This allows for both shock waves and combustion phenomena to be imaged, noting that the chemiluminescence from the combustor flame has been blocked by the laser-line filter. Across the boundaries of these structures a gradient in either static pressure or static temperature exists creating a region of increased contrast in the interferograms.

Shocks can be identified in the interferograms by the presence of interference/diffraction fringe patterns in the images. These patterns are caused by the interaction of the coherent, monochromatic laser light with the step-increase in density associated with a shock wave. If the density were to take an infinitely large step-increase across the shock, this pattern can be seen to be the exact same phenomenon that creates the diffraction of laser light around a knife edge, or through a slit aperture. Since this is not the case, the light travers-

ing this denser downstream fluid will take a longer optical path through the test-section, and as such obtain a shift in phase compared to the light that traverses the test-section upstream of the shock. This phase difference between adjacent rays of light will add a layer of interference to the recorded image as well.

For all of the images presented, the light was sheared in the flow-parallel orientation to allow for the best visualization of the density gradients present. The shearing axis and the required orientation of the Wollaston crystal is shown in Figure 2.11. The images presented are constructed by calculating the absolute gradient of the recorded intensity field, $\nabla^2 I(x, y)$. This removed most of the imaging effects created by inhomogeneities in the illumination field of the laser.

2.2.7 Flame Tracking from Interferograms

The images produced by this shearing interferometry can be used to track the location of the flame within the combustor. The mean axial position of the flame inside the combustor can be identified by averaging the recorded image intensity across each vertical slice of an image to create a one-dimensional axial image intensity profile. From the interferograms, the flame front is identified as being the location of the inflection point in this one-dimensional profile. More formally this is the most forward location along the intensity profile where

(2.26)
$$\frac{\partial^2 I}{\partial x^2} = 0.$$

A floor value is used to remove any local peaks that may be present, such as in the vicinity of the fuel injector. An example of this procedure is given in Figure 2.12 showing the reduction of the two-dimensional image to a one-dimensional intensity profile and the identification of the flame front position.
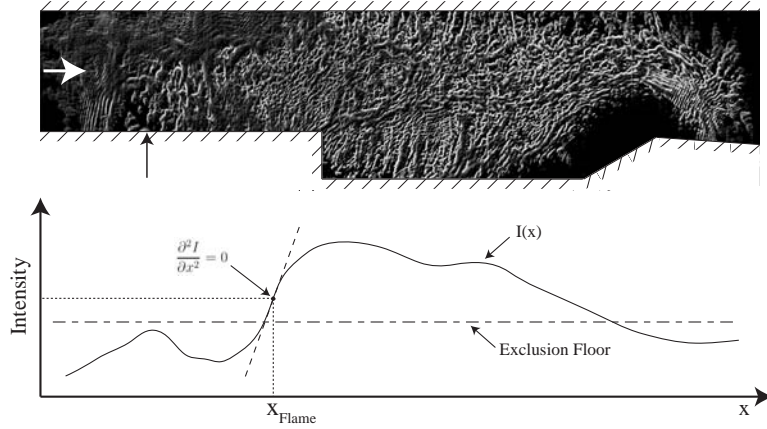
Figure 2.12: Illustration of the procedure used to identify the flame front from an interferogram.

2.3 Experimental Conditions

The experimental cases that will be discussed constitute a variation of the inlet stagnation temperature, T_o, inlet stagnation pressure, P_o, and pressure applied to the fuel injector, P_F. The stagnation pressures are quoted as gauge measurements. The pre-pseudo-shock Mach number, M_1, is a function of the inlet stagnation conditions for the fixed nozzle geometry used in this work. The fuel-oxidizer equivalence ratio, ϕ, and the fuel-jet momentum-flux ratio, r, are a function of both the inlet stagnation conditions and fuel injector pressure, as well as the geometry of the injector itself. These parameters will be used to quantify the blockages that can be associated with the fluid-mechanics and combustion present in the flow. This is further detailed in Section 3.1.

The remaining chapters of this work can be divided into two sets of investigations. The first looks to examine the interactions between the isolator and combustor, with an emphasis on the development of blockage in the device through fuel injection and combustion, and can be found in Chapter III. The cases that will be presented and discussed as part of this study are given in Table 2.4, and are denoted by a subscript 1.

The boundary-layer momentum thickness, θ, and the boundary-layer momentum thick-

Table 2.4: Experimental conditions for Cases A_1-W_1: Isolator/Combustor Interaction Study

Case	Mode	M_1	P_o	T_o	ϕ	r	Re_θ	θ
			kPa	K			10^3	mm
A_1	Ram	2.14	310.3	1000	0.30	1.452	2.50	0.248 ± 0.014
B_1	Ram	2.14	310.3	1000	0.25	1.354	2.66	0.247 ± 0.015
C_1	Scram	2.14	310.3	1200	0.30	1.417	1.79	0.198 ± 0.005
D_1	Ram	2.14	310.3	1200	0.25	1.342	1.83	0.198 ± 0.004
E_1	Scram	2.14	310.3	1400	0.30	1.374	1.11	0.128 ± 0.018
F_1	Scram	2.14	310.3	1400	0.25	1.331	0.92	0.120 ± 0.023
G_1	Ram	2.17	448.2	1000	0.30	1.519	2.15	0.191 ± 0.050
H_1	Ram	2.17	448.2	1000	0.25	1.436	2.10	0.190 ± 0.050
I_1	Ram	2.17	448.2	1200	0.30	1.476	1.72	0.162 ± 0.024
J_1	Ram	2.17	448.2	1200	0.25	1.400	1.61	0.170 ± 0.020
K_1	Ram	2.17	448.2	1400	0.30	1.440	0.62	0.074 ± 0.040
L_1	Ram	2.17	448.2	1400	0.25	1.367	0.61	0.073 ± 0.040
M_1	Ram	2.18	586.1	1200	0.30	1.510	0.96	0.082 ± 0.054
N_1-U_1	Ram	2.15	379.2	1200	0.2-0.3	1.18-1.49	1.7-2.0	$0.186\text{-}0.189 \pm 0.012$
V_1	Scram	2.15	379.2	1200	0.215	1.253	1.91	0.187 ± 0.012
W_1	Scram	2.15	379.2	1200	0.198	1.183	1.83	0.188 ± 0.012

ness based Reynolds number, Re_θ, are influenced by the inlet stagnation conditions and the geometric, and material, characteristics of the test-section. The operating mode of the test-section, either Ram or Scram, for each condition is provided for the reader's convenience.

Chapter IV contains an investigation of the ram-scram mode transition behavior and flame/shock-train interactions present in the test-section. A focus is given to the role of the flame in creating combustor blockage, and its interaction with the rest of the system. Five Cases, A_2 through E_2, were selected for study. Case A_2 represents a ram-scram transition that was caused by decreasing the equivalence ratio between steady conditions. Case B_2 was a ram-scram transition caused by rapidly decreasing the equivalence ratio over a 90

Table 2.5: Experimental Conditions for Case A_2: Ram-scram transition by decreasing equivalence ratio, ϕ, for steady conditions. For all cases; inlet stagnation temperature, T_o, of 1400 K, inlet stagnation pressure, P_o, of 448.2 kPa gauge and inlet Mach number, M_1, of 2.17.

Case	Mode	T_o	ϕ	r
	kPa	K		
A_2^1	Ram	1400	0.337	1.421
A_2^2	Ram	1400	0.286	1.285
A_2^3	Ram	1400	0.257	1.210
A_2^4	Ram	1400	0.224	1.109
A_2^5	Scram	1400	0.187	0.990
A_2^6	N/A	1400	0	0

Table 2.6: Experimental Conditions for Case B_2: Ram-scram transition by rapid decrease in equivalence ratio, ϕ. For all cases; inlet stagnation temperature, T_o, of 1000 K, inlet stagnation pressure, P_o, of 448.2 kPa gauge and inlet Mach number, M_1, of 2.17. Frame timing, t, is given for reference.

Case	Mode	T_o	ϕ	r	t
	kPa	K			sec
B_2^1	Ram	1000	0.210	1.110	5.80
B_2^2	Ram	1000	0.196	1.080	5.82
B_2^3	Ram	1000	0.182	1.050	5.84
B_2^4	Scram	1000	0.168	1.020	5.86
B_2^5	Scram	1000	0.14	0.990	5.88

msec time duration. Case C_2 was a scram-ram transition that was caused by increasing the wall temperature, and Case D_2 represents several ram-mode conditions during which the flame and the shock train underwent oscillations. Case E_2 examines the relationship between flame penetration and inlet stagnation temperature while operating in a cavity shear-layer combustion stabilized regime. The experimental conditions presented as part of this study are provided in Tables 2.5 through 2.9.

Table 2.7: Experimental Conditions for Case C_2: Ram-scram transition by increasing wall temperature, T_w. For all cases; inlet stagnation temperature, T_o, of 1000 K, inlet stagnation pressure, P_o, of 448.2 kPa gauge and inlet Mach number, M_1, of 2.17. Frame timing, t, is given for reference.

Case	Mode	T_o	$(T_w)^*$	ϕ	r	t
		kPa	K	K		sec
C_2^1	Scram	1000	556	0.185	1.111	6.61
C_2^2	Scram	1000	567	0.185	1.111	6.62
C_2^3	Ram	1000	577	0.185	1.111	6.63
C_2^4	Ram	1000	589	0.185	1.111	6.64
C_2^5	Ram	1000	608	0.185	1.111	6.65

*Estimate from unsteady finite-difference simulation of heat transfer through test-section walls. External wall temperature predictions were found to agree to within 8.5% with measured values. See Section 2.2.4.1.

Table 2.8: Experimental Conditions for Case D_2: Dynamics of ram-mode flame oscillations. For all cases; inlet stagnation pressure, P_o, of 448.2 kPa gauge and inlet Mach number, M_1, of 2.17.

Case	Mode	T_o	ϕ	r
		kPa	K	
D_2^1	Ram	1200	0.322	1.433
D_2^2	Ram	1400	0.286	1.285

Table 2.9: Experimental Conditions for Case E_2: Flame penetration angle. For all cases; inlet stagnation pressure, P_o, of 448.2 kPa gauge and inlet Mach number, M_1, of 2.17.

Case	Mode	T_o	ϕ	r
		kPa	K	
E_2^1	Ram	1000	0.213	1.160
E_2^2	Ram	1200	0.211	1.116
E_2^3	Ram	1400	0.224	1.109

CHAPTER III

Investigation of Isolator/Combustor Interactions

3.1 The Description of Combustor Blockage

In the past, the blockage creating the isolator back pressure has been near-universally thought of as the equivalent of a simple valve. Many shock-train studies have been undertaken with this physical arrangement as a substitute for a combustion-induced back pressure. The back pressure inducing blockage created by a combusting fuel-jet in a cross-flow will have contributions from two sources. The first source is fluid-mechanical in nature, and is in fact the exact same as that found in the non-reacting case. This mechanical blockage is defined as the component of the isolator back pressure created by the fluid-mechanical structure of the fuel-jet alone and is described by the momentum-flux ratio, formally defined as

$$(3.1) \qquad r = \left(\frac{\rho_F u_F^2}{\rho_I U_I^2} \right)^{1/2} = \left(\frac{\rho_F u_F^2}{\gamma P_1 M_1^2} \right)^{1/2},$$

where the relation $\rho u^2 = (P/RT)u^2 = (P/\gamma RT)\gamma u^2 = \gamma P M^2$ has been used. The isolator flow quantities in this definition will be evaluated at the pre-pseudo-shock condition, denoted by a subscript 1, to provide the momentum ratio between the obstructing fuel jet and the unobstructed cross-flow. This definition is the supersonic analog to the subsonic instance where the cross-flow quantities are measured external to the influence of the impinging jet. The fundamental gas dynamics equation, Equation 1.1, shows that the addition

36

of mass has an effect that is similar to the addition of heat. Therefore, combustor blockage is due to a combination of both heat and mass addition.

The wall-normal fuel injection will create a region of momentum deficit in the cross-flowing air. This jet-wake structure, created through the acceleration of the fuel, decelerates the cross-flow, increasing the static pressure at the location of the injector. As the momentum-flux ratio is increased, the fuel plume will penetrate further into the cross-flow, creating a larger region of momentum deficit in the jet-wake and a proportionally larger rise in static pressure.

The jet-wake structure influences the nature of the flame stabilization in the combustor. Micka and Driscoll [35] found that the jet-wake allowed for the anchoring of the flame forward of the cavity, impacting the heat-release distribution within the combustor.

The additional mass-flow of fuel through the combustion, and the deformation of the near-injector flow field to create a flow-area constriction, are two of the driving factors influencing the effectiveness of the mechanical blockage developed under any set of conditions. These factors create a situation similar to that observed in the converging segment of a supersonic diffuser, where the flow velocity decreases through the area constriction and is accompanied by a rise in static pressure. This static pressure rise then contributes to the back pressure being applied to the isolator section of the device.

The combustion of the fuel in the jet is the second source of blockage, and will be quantified by the equivalence ratio, which is defined for this investigation as

$$(3.2) \qquad \phi = \frac{\dot{m}_F}{f_s \dot{m}_{I,O_2}} = \frac{\dot{m}_F}{f_s Y_{O_2} \dot{m}_I},$$

where f_s is the stoichiometric fuel-oxygen mass ratio and the subscript I refers to the isolator flow which is not pure air, but contains additional water vapor from the vitiated air heater. The combustion blockage is defined as the component of the isolator back pressure created by the chemical reaction of the fuel and oxidizer, the structure of the induced flame

front and the expansion of the downstream products. These two blockage parameters are calculated for a number of operating conditions in Table 2.4. Inlet Stagnation Pressures, P_o, are quoted as gauge measurements. The reader will note that the two blockage variables described here are not independent, but are coupled through the geometry of the fuel injector. This fact is discussed further in Section 3.3.

3.2   The Steady Shock-train

One of the most informative observations that can be made about the operation of the test-section is the profile of the static pressure inside the device, along its front-to-rear axis. These measurements provide basic information about the pseudo-shock, such as the total pseudo-shock length and maximum isolator pressure rise. However, they also provide more subtle information about the blockage creating the pseudo-shock itself.

Figure 3.1(a) shows pressure measurements for six experimental conditions, with the same upstream stagnation pressure but three different stagnation temperatures, $T_o = 1000$, 1200 & 1400 K, and two equivalence ratios, $\phi = 0.25$ & 0.30. The stagnation temperature change between Cases A_1, C_1 & E_1, each having the same equivalence ratio of $\phi = 0.30$, is found to effectively lower the mechanical blockage in the combustor. This allows the flow to transition from subsonic(ram) to supersonic(scram) operation. This transition to scram mode can be attributed to a resultant increase in the cross-flow momentum-flux through the isolator, relative to that of the wall-normal fuel-jet. This is due to an increase in the velocity of the isolator flow which also offsets the reduction in gas density due to static temperature increase.

The location of thermal choking is marked as the shaded region in Figure 3.1. This was determined using the standard criterion, [18]

$$(3.3) \qquad \frac{1}{A}\frac{dA}{dx} = \frac{1+\gamma}{2}\frac{1}{T_o}\frac{dT_o}{dx}.$$

Values of dT_o/dx were measured previously by Micka and Driscoll [36].

The ram-to-scram mode transition is also seen in Cases B_1, D_1 & F_1, for a lower equivalence ratio. A lower equivalence ratio is coupled to a lower value of momentum ratio as less fuel is being injected into the combustor. However, as can be seen from the ram-mode operation of both Cases B_1 & D_1, where one would expect both cases to operate in scram-mode based on the behavior of Case C_1 at a higher equivalence ratio, the interaction of the mechanical blockage with the combustion induced blockage can have unexpected results. The obstruction present in the combustor does indeed operate like a valve, however one in which there are two coupled components.

The mechanical blockage influences the effectiveness and location of the combustion blockage. This creates a situation in which the relationship between the mechanical and combustion blockage can be either reinforcing, as with the mode transition between Cases C_1 & D_1, or destructive, as with the lack of transition between Cases B_1 & D_1. The fixed combustor geometry is thought to play a role in influencing the form of this interaction between the mechanical blockage, provided by an increase in momentum ratio, relative to that of the combustion induced blockage, provided by an increase in equivalence ratio. A discussion of the influence of isolator geometry on the pressure recovery is provided later in Section 3.3.

This coupling between the mechanical and combustion blockages can also be seen in Figure 3.1(b), where six cases are again provided for a set stagnation pressure, three different stagnation temperatures, T_o = 1000, 1200 & 1400 K, and two equivalence ratios, ϕ = 0.25 & 0.30. The variation in stagnation temperature between Cases G_1, I_1 & K_1 again reduces the mechanical blockage, momentum ratio, present between each case. This reduction, instead of creating a ram-to-scram mode transition, as in Figure 3.1(a), causes a shift in the pseudo-shock downstream anchor point, which is the location of maximum
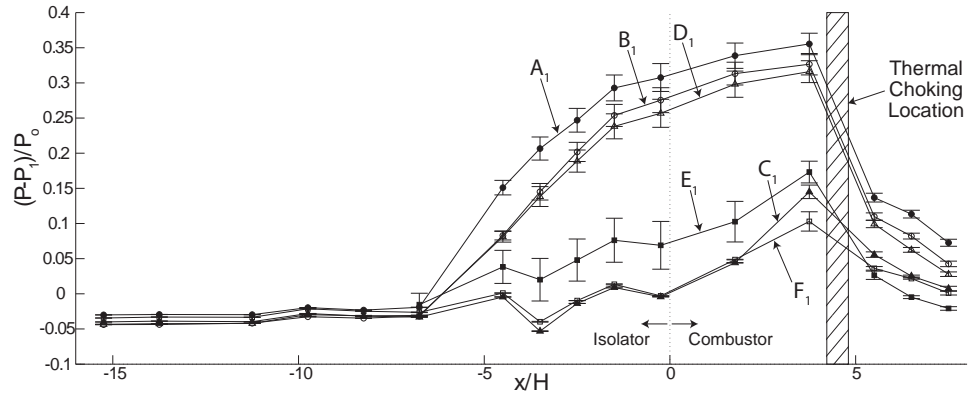
(a) Ram- and Scram-mode combustion
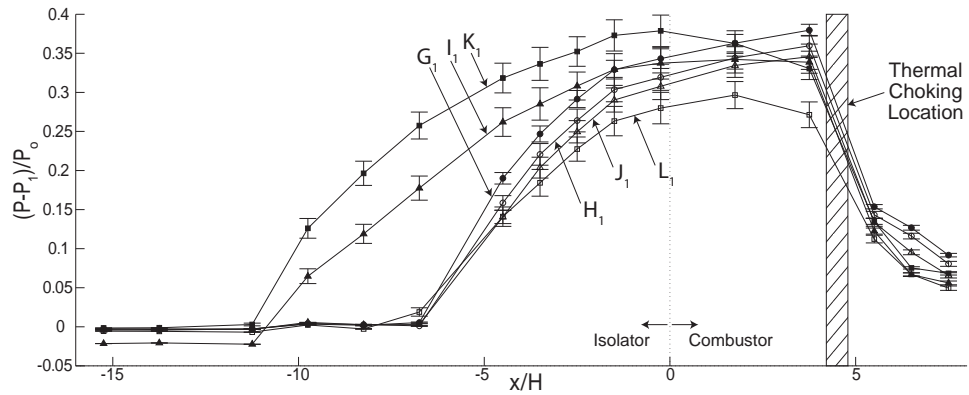
(b) Pseudo-shock downstream anchor point variation

Figure 3.1: Pressure distribution across pseudo-shock showing (a) Ram- and Scram-mode combustion and (b) variation in the downstream anchor point, which is the x-location of the maximum pressure. $x = 0$ is the location of the fuel injector. See Table 2.4 for test case conditions.

pressure recovery. The anchor point is seen to move from the thermal throat in Case G_1, forward to an intermediate position in Case I_1 and forward again to the location of the fuel injector in Case K_1.

This is counterintuitive, as a decrease in momentum ratio would be expected to move the point of maximum pressure recovery further downstream from the location of the fuel injector. The reduction in momentum ratio, between Cases G_1, I_1 & K_1, has been achieved by an increase in stagnation temperature. The static temperature at the fuel injector will increase accordingly, allowing a smaller fluid obstruction, i.e. the wake of the fuel-jet, to provide the residence time required to stabilize the flame in a more forward position. This behavior is consistent with the findings of Micka and Driscoll [35]. The geometry of the isolator and fuel injector, and the inlet stagnation conditions, play a key role in determining the form of interaction between mechanical and combustion blockage.

Changes to the stagnation pressure also will impact the behavior of the pseudo-shock. Figure 3.2(a) gives longitudinal pressure profiles for a single stagnation temperature, T_o = 1200 K, three different stagnation pressures, P_o = 310.3, 448.2 & 586.1 kPa and two equivalence ratios, ϕ = 0.25 & 0.30. For a fixed value of equivalence ratio, an increase in stagnation pressure, Cases C_1, I_1 & M_1, causes the pseudo-shock to grow in length. The entrance to the pseudo-shock of Case M_1 is actually seen to be further downstream relative to the lower stagnation pressure in Case I_1 due to the shift in anchoring location. The Case M_1 pseudo-shock is still anchored at the thermal throat, while the Case I_1 pseudo-shock is anchored forward of this location due to the difference in flame anchoring characteristics between these two cases. The higher stagnation pressure in Case M_1 provides a longer pseudo-shock but this is disguised by the offsetting variation in anchor location, resulting in a similar isolator length requirement but a higher density through-put at the same equivalence ratio. An increase in equivalence ratio also is found to result in a longer shock-train

(Cases I_1 & J_1) or a combustion mode transition (Cases C_1 & D_1) as previously discussed.

Alternatively, an increase in equivalence ratio can drive an increase in the demanded maximum pressure recovered in the isolator, and required pseudo-shock length, without pushing the downstream pseudo-shock anchor point upstream, as in Figure 3.2(b).

As expected, the smallest equivalence ratios, $\phi = 0.198$ and 0.215, and smallest momentum ratios, $r = 1.183$ and 1.253, corresponding to Cases W_1 and V_1, led to scram-mode operation of the test-section. Scram-mode is identified by small pressure rises in the isolator, which extends from $x/H = $ -15 to $x/H = 0$. Fuel is injected at $x/H = 0$ and thermal choking occurs near where the wall begins to diverge at $x/H = 4.5$. For all other cases plotted in Figure 3.2(b), the large pressure rise indicates that ram-mode occurs. It is seen that as equivalence ratio and momentum ratio increase, the maximum pressure recovered, $(P_2 - P_1)/P_o$, in the isolator increases. As the recovered pressure increases, Figure 3.2(b) shows that the length of the pseudo-shock increases as well.

This continues until the maximum pressure recovered reaches a plateau, as seen in a zero rise in the recovered pressure between Cases O_1 & N_1 for a rise in equivalence ratio from $\phi = 0.290$ to 0.301. This limiting effect is a result of the coupling between the isolator geometry and the mechanics of the fuel injector, which will be discussed further in Section 3.3 under the context of a behavior map coupling between isolator and fuel injector.

This limiting behavior also is observed in Figure 3.2(a) where the stagnation pressure increase between Cases D_1 & J_1 drives an increase in the maximum recovered pressure, while the same increase in stagnation pressure between Cases I_1 & M_1 does not. This occurs even though in absolute terms an increase in stagnation pressure with a set equivalence ratio means a higher rate of fuel consumption and blockage.
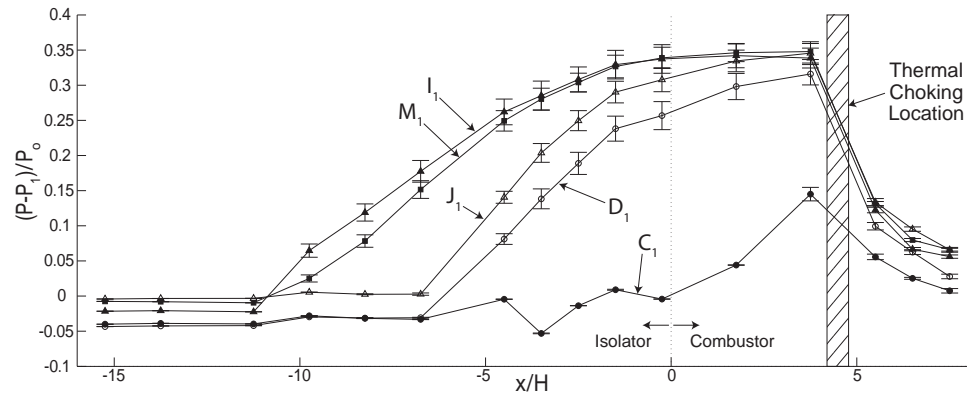
(a) Stagnation pressure, P_o, dependence
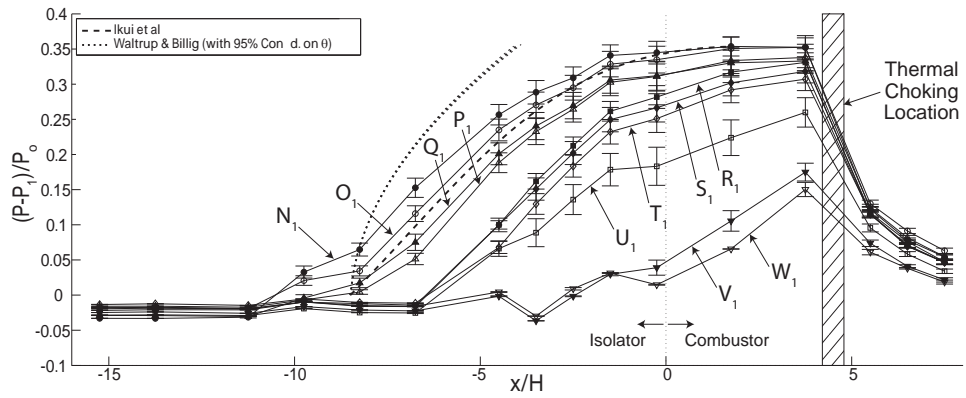
(b) Equivalence ratio, ϕ, dependence

Figure 3.2: Pressure distribution across pseudo-shock showing (a) stagnation pressure, P_o, dependence and (b) equivalence ratio, ϕ, dependence, $x = 0$ is the location of the fuel injector. See Table 2.4 for test case conditions.

3.3 Isolator Behavior and Isolator/Combustor Coupling

The observations that have been made to this point show a great deal of interaction between the pseudo-shock present in the isolator and the manner in which the fuel is injected into the combustor. The isolator geometry plays a key role in prescribing the pressure recovered by the isolator pseudo-shock when subjected to a fuel injection induced blockage. This blockage, as previously discussed, can be attributed to one of two causes, either a chemical blockage due to the combustion of fuel or a mechanical blockage due to the fluid-mechanical obstruction created by the fuel-jet. These have been quantified here in terms of the fuel equivalence ratio and the fuel-jet momentum ratio, respectively.

The relationship between these three parameters, for the MDMC test-section geometry, is given in Figure 3.3, which includes data from all the experimental runs undertaken in this study. The isolator pressure recovery is seen to behave as a function of equivalence ratio and fuel-jet momentum ratio, with the isolator geometry acting as the transfer function dictating the relationship between the parameters. For Example, if the equivalence ratio is 0.3 and the fuel-jet momentum ratio is 1.5, Figure 3.3 shows that the pressure recovered, $(P_2 - P_1)/P_o$, is 0.36.

In dissecting this behavior, it is instructive to examine the operation of the fuel-jet in isolation of the pseudo-shock. Considering a set of isolator stagnation conditions, P_o, T_o and M_1, and an applied fuel injector pressure, P_F, will result in the injector developing one particular blockage condition, or a pairing of a fuel equivalence ratio and a fuel-jet momentum ratio. This can be seen analytically by taking Equation 3.1 and substituting the relation

$$(3.4) \qquad \rho u^2 = \rho u \cdot u = \frac{\dot{m}}{A} \cdot \frac{\dot{m}}{A\rho} = \frac{\dot{m}^2}{A^2 \rho},$$
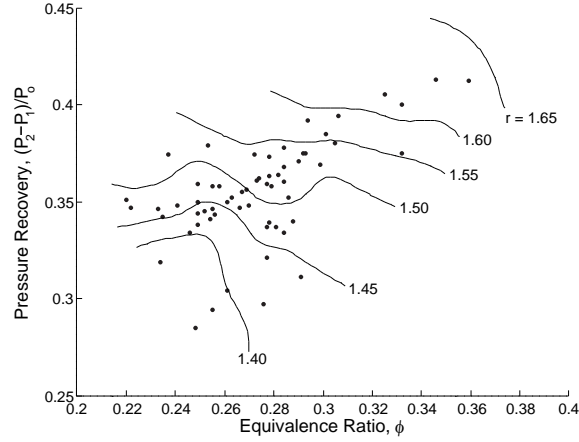
Figure 3.3: Isolator pressure recovery as a function of the chemical and mechanical blockage created by wall-normal fuel injection. The chemical blockage is quantified by the fuel equivalence ratio, ϕ, and the mechanical blockage by the fuel jet momentum ratio, r, shown as contours. Experimental operating points are marked with dots.

where $\dot{m} = \rho A u$ has been used, to provide

$$
(3.5) \qquad r = \left[\frac{\rho_I A_I^2}{\rho_F A_F^2} \frac{\dot{m}_F^2}{\dot{m}_I^2} \right]^{1/2}.
$$

Rearranging Equation 3.2 and substituting gives

$$
(3.6) \qquad r = \Lambda \cdot \phi,
$$

where the injector parameter has been defined as

$$
(3.7) \qquad \Lambda = \left[\left(\frac{\rho_F}{\rho_I} \right)^{-1/2} f_s Y_{O_2} \left(\frac{A_F}{A_I} \right)^{-1} \right].
$$

This relation, having been developed with the assumption of a choked fuel injector orifice, must be modified to account for the non-linear behavior of the injector for lower, unchoked, values of ϕ. The injector was only run under choked injector conditions. To first order, Equation 3.6 takes the form

$$
(3.8) \qquad r = \Lambda \cdot \phi + f^n (P_2, P_F).
$$

This relation can be seen experimentally as well, and is shown in Figure 3.4 for two different stagnation pressures, where the stagnation temperature has been changed to alter the value of Λ in each case.
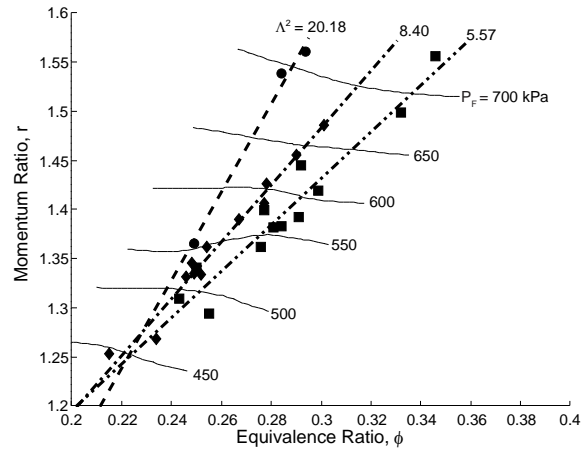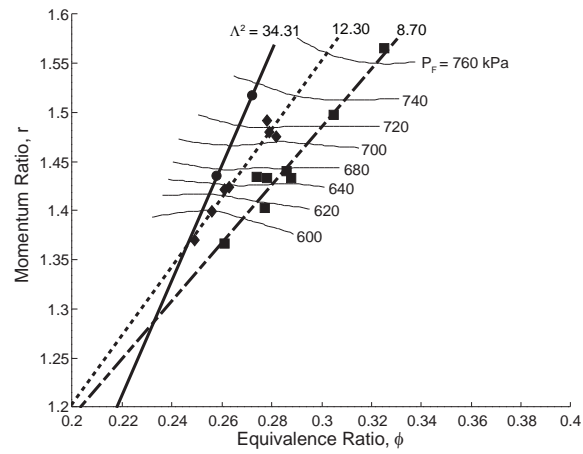
Figure 3.4: Fuel injector map relating fuel equivalence ratio, ϕ and fuel jet momentum ratio, r for a particular fuel injector geometry at an isolator flow stagnation pressure, P_o, of (a) 376.2 and (b) 448.2 kPa, with contours of fuel injector pressure, P_F, overlaid in kPa. The injector parameter Λ is given in Equation 3.7, with values shown for stagnation temperatures, T_o, of 1000 K, 1200 K and 1400 K moving from high to low values of Λ respectively.

This fuel injector behavior can now be overlaid onto the isolator pressure recovery map to more readily see the coupling of the pseudo-shock condition to the blockage provided by the fuel injector. The blockage itself is dependent on the isolator stagnation conditions and the applied fuel injector pressure. This is shown in Figure 3.5(a) where each of the fuel injector operating lines, from Figure 3.4, have been mapped onto the contours of fuel-jet momentum ratio from Figure 3.3.

Billig [3] proposes a pressure-area method for estimating the pressure recovery, as a function of stagnation temperature addition to the flow through the combustor, in terms of an entropy-limit solution to a set of simplified compressible flow equations. The results of using this method are shown in Figure 3.5(b) for three different values of stagnation temperature. Billig's method provides the same qualitative trend between increasing equivalence ratio and increasing pressure recovery seen in Figure 3.5(a), but not numerical agreement. This is expected as the operating conditions used in the experiment could not be matched to those provided by Billig.

Using this isolator/combustor coupling map, Figure 3.5(a), and a known set of isolator operating conditions and fuel injector pressure, the pressure recovered in the isolator section can be determined. Note that both the blockage behavior of the fuel injector and the pressure recovery in the isolator are highly dependent on their respective geometries.

An increase in fuel injector pressure can now be considered in terms of its impact on the pressure recovery demanded from the isolator. Beginning at the operating Point "A" in Figure 3.6, a throttle-up in fuel injector pressure will move the operating point along the fuel injector operating line to Point "B". The motion along a static operating line is reasonable so long as the throttle-up occurs "fast" compared to the acceleration response time of the notional vehicle to which the engine is attached. The assumption that the density of the fuel-jet remains constant during the throttle-up operation is also required for

47
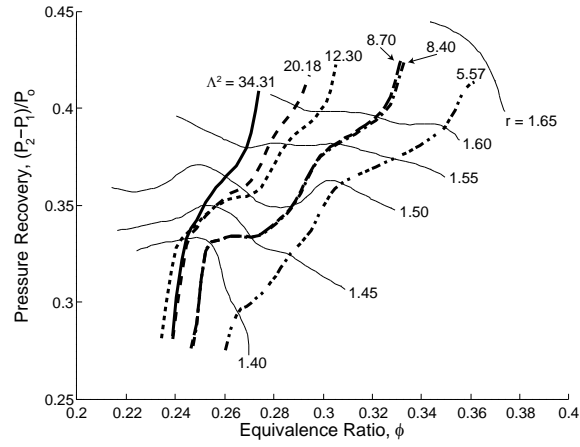
(a) Isolator/Combustor coupling map
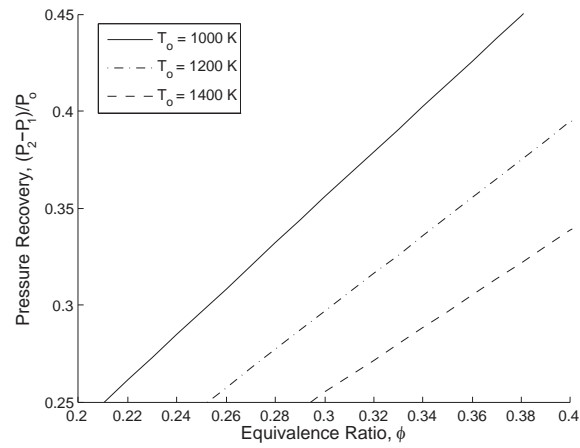
(b) Billig's pressure-area method

Figure 3.5: Isolator/Combustor coupling map showing the isolator pressure recovery (a) for a particular operating condition and fuel injector geometry, as a function of fuel equivalence ratio, ϕ, and fuel-jet momentum ratio, r, shown as contours, and (b) as estimated using the pressure-area method of Billig [3].
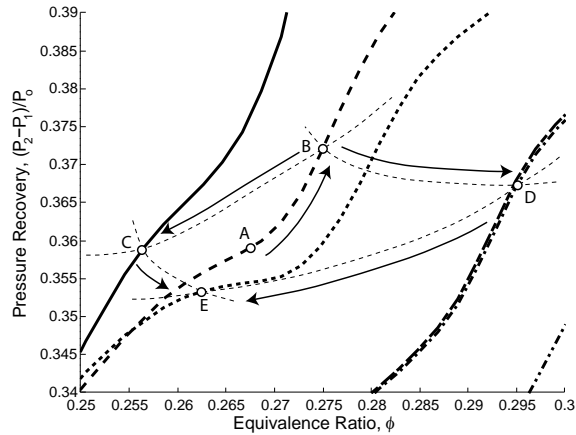
Figure 3.6: Isolator/Combustor coupling map showing the operating point of the isolator adjusting to an increase in fuel injector pressure. The isolator pressure recovery, for a particular operating condition and fuel injector geometry, is given as a function of fuel equivalence ratio, ϕ and fuel jet momentum ratio, r.

the operating point to move along a line of constant Λ, where in actuality the density of the fuel-jet is related to the pressure applied to the injector and the operating point would move along a line of constant isolator cross-flow density, $\rho_I = $ Constant.

Once the vehicle begins to respond to the new engine output, there exist two paths that will bound the pressure recovery in the isolator and are dependent on the ordering of the change in isolator inlet conditions. If the stagnation pressure were to increase first and then the stagnation temperature, the isolator operating point will move from Point "B" to Point "E" through Point "C". If the opposite happens, with the temperature increase preceding the pressure increase, the operating point will move instead through Point "D" on its way to Point "E".

These two extreme cases form the bounds for the movement of the operating point from Point "B" to Point "E". The operating point always moves on a surface of constant fuel injector pressure at its intersection with the current isolator operating conditions.

3.4 Boundary-layer Analysis

In an effort to better understand the flow state present in the isolator upstream of the pseudo-shock, an analysis of the boundary-layer that develops along the isolator wall was undertaken. Two methods were used to obtain this information. The first was a traversing stagnation Pitot pressure probe and the second was Schlieren imagery of the density variations through the boundary-layer in the isolator. The second method had to be used due to the thermally induced material failure of the Pitot tube above stagnation temperatures of T_o = 1000 K.

The Pitot tube arrangement consisted of a 1.19 mm (3/64 inch) diameter, 316 stainless steel tube, which was bent to allow the tip to be brought into near contact with the isolator wall. A computer controlled traverse was used to vary the position of the Pitot tube. The Mach number profiles shown in Figure 3.7(a) were obtained from 6 separate test runs for each of the inlet stagnation pressure cases that will be presented. Much of the method used to obtain the velocity and mass-flux profiles, which are required to calculate the integral boundary-layer thicknesses, follows that outlined by Bement et al. [1].

The inner wall temperature of the isolator is a required quantity in this equation but it is not easily measured, particularly without introducing an excess of disturbances into the flow. To address this, an unsteady finite-difference model was constructed to model the evolution of the temperature over the length of a test-section run.

The boundary-layer profiles for the inlet stagnation pressures of 310.3, 448.2 & 586.1 kPa and a stagnation temperature of 1000 K are compiled in Figure 3.7. For the lowest stagnation temperature the Pitot probe was used. The Schlieren method was then used to estimate boundary-layer thicknesses at all stagnation conditions.

Schlieren images of the flow were taken for all 9 test conditions, which were combina-
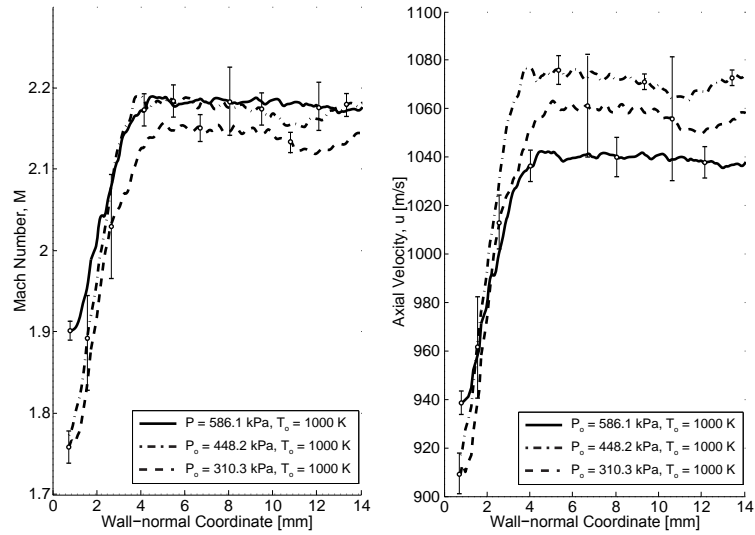
(a) Mach Number Profile

(b) Axial Velocity Profile
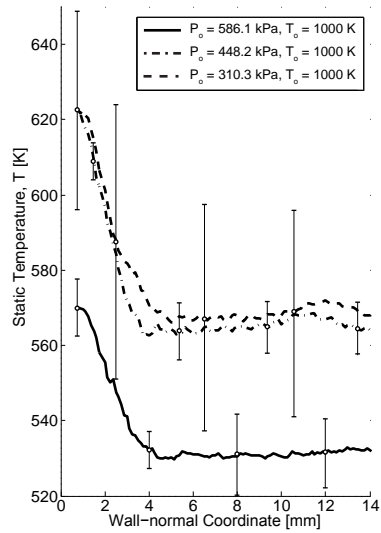
(c) Static Temperature Profile

Figure 3.7: Boundary-layer profiles of (a) Mach number, (b) axial velocity and (c) static temperature as measured using a Pitot stagnation pressure probe. Measurement error bounds are given for selected positions.

tions of the stagnation pressures of 310.3, 448.2 & 586.1 kPa and stagnation temperatures of 1000, 1200 & 1400 K. As Figure 3.8 shows, the Schlieren results for boundary-layer velocity and momentum thicknesses agree well with those obtained from the Pitot tube, while those for displacement thickness do not. This is due to the inability of the Schlieren method to adequately recreate the boundary-layer velocity profile in the wall-normal direction. The velocity thickness estimation does not rely on this profile but is directly read from the impact of the thermal boundary-layer on the density gradients in the flow. The momentum thickness, while it is dependent on the velocity profile, is less sensitive to inaccuracies than the displacement thickness due to the fact that this is a supersonic flow and the majority of the momentum carried within the boundary-layer will be in the portion furthest from the wall, which has been shown to be estimated reliably.

3.5 Pseudo-shock Pressure Rise & Length

For each of the experimental cases, pressure measurements have been made along the length of the isolator section. This allows a comparison to be made with existing models of the pressure rise that occurs across a pseudo-shock. Models have been proposed beginning with Crocco's [10] shockless model which assumes that the presence of the shocks can be disregarded entirely with the dissipation in the flow assumed to be due to the turbulence in the near wall regions. A uniform and isentropic central core flow also is assumed.

The diffusion model of Ikui et al. [22] improves on Crocco's work by considering that the central core region in the duct is not isentropic, which allows for the pressure rise across a pseudo-shock to take the form

$$(3.9) \qquad \frac{P - P_1}{P_2 - P_1} = \frac{\left\{ w_1^2 \left(w_1^2 - 2w^{*2} \right) + w_1^2 w^{*2} e^{-c(x/D)} \right\} \left(1 - e^{-c(x/D)} \right)}{\left(w_1^2 - w^{*2} \right)^2 - w_1^2 \left(w_1^2 - w^{*2} \right) e^{-c(x/D)} \left(1 - e^{-c(x/D)} \right)},$$

where w is the Crocco number, $c = 0.114$ is determined from experiment and D is the hydraulic diameter of the duct. Quantities with a subscript 1 refer to the pre-pseudo-shock
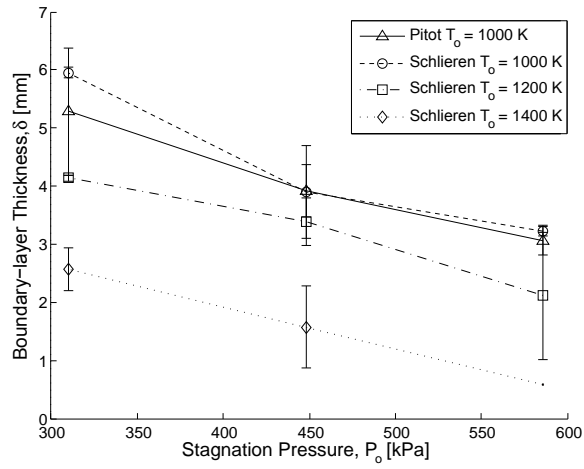
(a) Boundary-layer thickness, $\delta_{99\%}$.
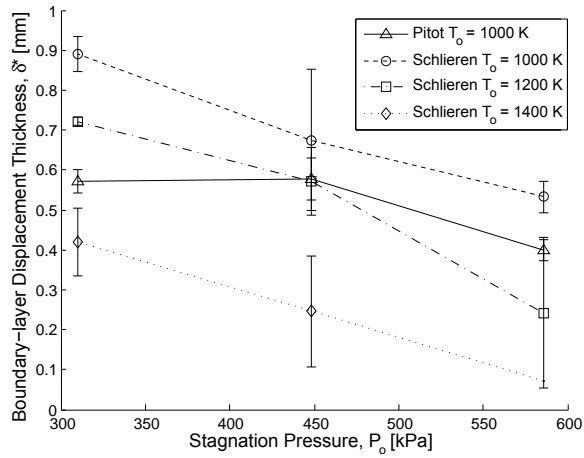
(b) Boundary-layer displacement thickness, δ^*.
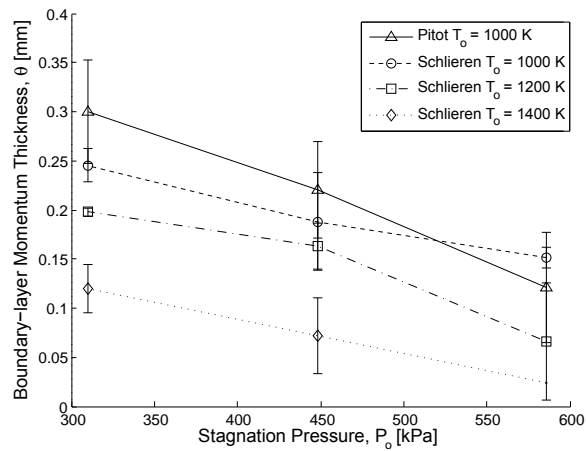
(c) Boundary-layer momentum thickness, θ.

Figure 3.8: Boundary-layer thickness measurements based on boundary-layer profiles obtained through Pitot tube and Schlieren techniques.

flow state and those with a 2 to the post-pseudo-shock state. A separate relation for the length of the pseudo-shock, L_p, is provided using the same assumptions,

$$(3.10) \qquad \frac{L_p}{D} = \frac{2}{c} sinh^{-1} \left(\frac{w_1 - w_2}{2w^*} \right).$$

It should be noted that this equation is not predictive of the maximum pressure recovered, but describes the profile of the pressure rise once both the pre- and post-pseudo-shock states are known.

The modified diffusion model of Ikui et al. [23] takes into account the friction losses to the walls of the duct, as well as the effect of the upstream boundary layer. Zimont and Ostras [53] also proposed a model which assumes that the dissipation inside the pseudo-shock takes on a jet-like structure and that it behaves in the manner of a submerged supersonic jet.

Waltrup and Billig [50, 49] offer the following correlation to experimental data obtained for a cylindrical duct:

$$(3.11) \qquad \frac{x \left(M_1^2 - 1 \right) Re_\theta^{1/4}}{D^{1/2} \theta^{1/2}} = 50 \left(\frac{P}{P_1} - 1 \right) + 170 \left(\frac{P}{P_1} - 1 \right)^2,$$

where θ is the momentum thickness of the undisturbed, pre-shock train, boundary-layer and Re_θ is the Reynolds number of the flow based on this length scale. The preceding analysis of the boundary-layers that are present under each of the experimental conditions can now be used with these models to assess their accuracy, and applicability, in estimating the key parameters of pseudo-shock length and pressure recovery.

Waltrup and Billig's correlation and Ikui et al.'s diffusion model are compared to experimental results to assess their ability to predict the longitudinal pressure rise profile along the isolator for instances where the stagnation temperature, Figure 3.9(a), and stagnation pressure, Figure 3.9(b), have been varied, with the particular model parameters adjusted

accordingly. The behavior of the correlation was found to be more sensitive to the estimated Reynolds number than the momentum thickness of the boundary-layer itself.

Ikui et al.'s diffusion model is found to provide fair agreement with the experimental profiles, showing some underestimation at the beginning of the pseudo-shock. As Bement et al. found for their results, Waltrup and Billig's correlation was also found to agree well with the experimental data, however its agreement seems to be highly dependent on the Reynolds number of the flow being considered. Case M_1 in Figure 3.9(b) shows this well, as the rate of pressure rise is over-predicted. Case M_1 has a $Re_\theta = 0.96 \cdot 10^3$ which places it just outside the lower limits of the data considered by Waltrup and Billig [50]. Case G_1, shown in Figure 3.9(a), also shows this behavior, but the slightly lower Mach number of the flow as compared to Case M_1 compensates for some of the over-prediction.

This tendency to over-predict the pressure rise for lower momentum thickness Reynolds number flows must be highlighted, as this quantity is very sensitive to the isolator cross-sectional geometry. This can be seen from the values reported by Waltrup and Billig [50] and Bement et al. [1]. The latter for instance took data using the Generic High Speed Engine experiment at NASA/Langley. While they operated at pressures, temperatures and Mach numbers comparable to the present work, they had a physically larger isolator cross-section of 101.6 mm x 104.6 mm (compared to the MDMC isolator at 25.4 mm x 38.1 mm), and thus they had thicker boundary-layers.

This has implications on the size of the system, wave-rider as compared to missile-scale, that this correlation is being used to describe. Care should be taken to confirm that the momentum-thickness Reynolds number of the flow falls within values considered by Waltrup and Billig in creating their fit, to ensure proper, applicable, predictions of the pseudo-shock behavior.

These limits on applicability in mind, a comparison of the overall pseudo-shock length
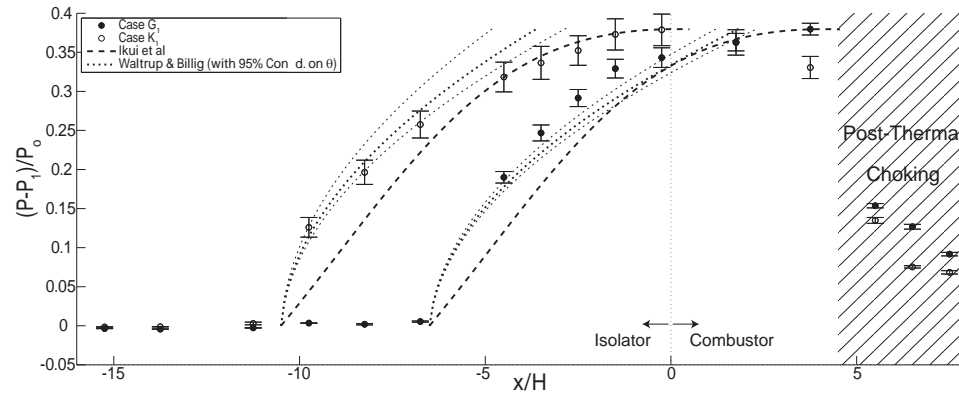
(a) Pseudo-shock approximation with stagnation temperature, T_o, dependence.
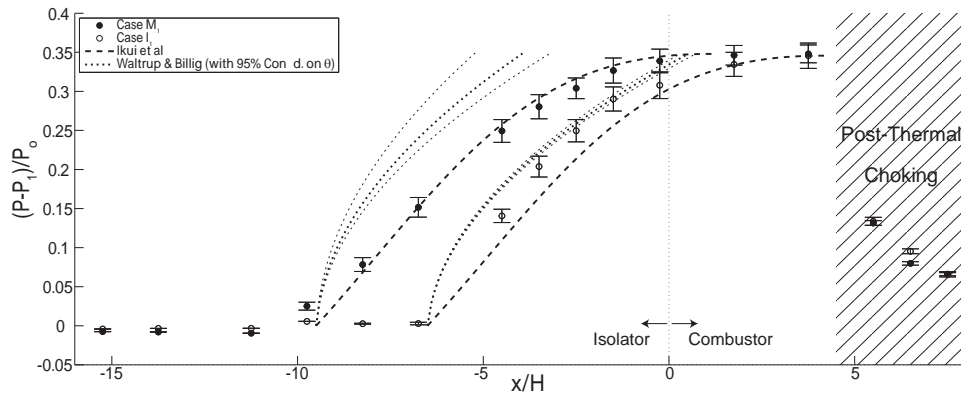
(b) Pseudo-shock approximation with stagnation pressure, P_o, dependence.

Figure 3.9: Pressure distribution across pseudo-shock showing (a) stagnation temperature, T_o, dependence and (b) stagnation pressure, P_o, dependence in comparison to the diffusion model of Ikui et al. [22] and the experimental correlation of Waltrup and Billig [50], $x = 0$ is the location of the fuel injector. See Table 2.4 for test case conditions.
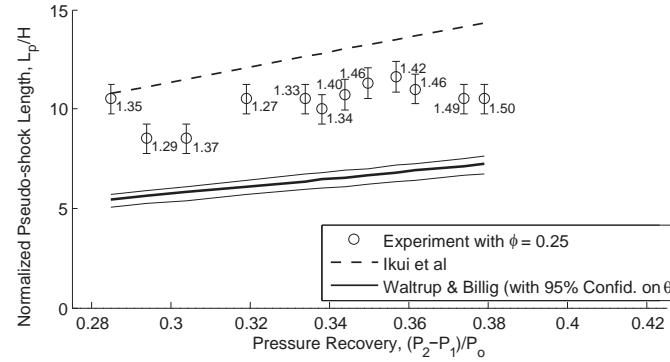
(a) $\phi = 0.25$
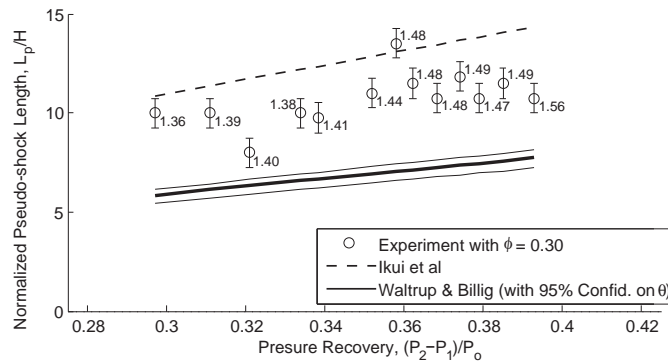
(b) $\phi = 0.30$

Figure 3.10: Comparison of pseudo-shock length from experiment for equivalence ratio, ϕ, of (a) 0.25 and (b) 0.30 with the diffusion model of Ikui et al. [22] and the experimental correlation of Waltrup and Billig [50] as a function of Maximum Pressure Recovery, $(P_2 - P_1)/P_o$. Labeled values are the momentum ratio, r, for each given condition.

can be made between these models and the present measurements, in order to better understand the influences of momentum and equivalence ratio on the blockage encountered by the isolator flow, as described earlier. Figure 3.10 provides a comparison between Ikui et al.'s diffusion model, Waltrup and Billig's experimental correlation and the present experimental data for two equivalence ratios, and a range of momentum ratios. In both cases, Ikui et al.'s pseudo-shock length prediction is found to be an overestimation, while Waltrup and Billig's length is an underestimation.

Values of momentum ratio, r, are indicated next to each data point in Figure 3.10, and it can be seen in both instances that the momentum ratio plays an important role in driving both an increase in the length of the pseudo-shock and the maximum pressure it will re-

cover over that length. This reinforces the point that the mechanical blockage created by the fuel-jet must be examined in the implementation of any injector design, in particular when considering the use of supersonic injectors or angled injectors that will increase or decrease, respectively, the wall-normal momentum ratio provided by a particular design.

3.6 Shock-train Structure & Operating Regimes

To aide in the interpretation of the pressure field measurements, Schlieren images were obtained of the shock train present in the isolator duct. These images allowed for the structure of the pseudo-shock to be examined and the regime under which the isolator shock-train was operating to be identified. These operating regimes include the existence of a simple normal shock, a curved shock, a branched normal shock or a series of shocks. A good discussion of these structures is presented by Matsuo et al. [29], in which the occurrence of a particular operating regime is linked to the flow confinement, or the ratio of the undisturbed boundary-layer thickness to the channel half-height, δ/h, and the isolator inlet Mach number, M_1.

Carrol and Dutton [6] note that for small values of δ/h a normal shock occurs, a series of nearly normal shocks occur for moderate values of δ/h and a series of oblique shocks occur for large δ/h. The discrimination between small and large flow confinement (δ/h) values appears in the literature to be fairly qualitative, with the inlet Mach number influencing this definition. An increase in inlet Mach number effectively decreases the flow confinement, hastens the onset of the full shock-train structure, while it increases the spacing between shocks already in series. This shock-train regime description, while subjective, has been found to generally describe the observed trends in the present work.

Some Schlieren images taken at 100 Hz of these regimes are shown in Figure 3.11. The other regimes are notionally depicted where unobservable due to the physical arrange-

ment of the test-section. The images display deviations from the established shock-train regime description that need to be addressed. According to the conventional description the oblique shocks observed in Figure 3.11(d) should be in the regime in which a series of normal shocks [6] occurs.

In the experimental cases examined here, the isolator inlet Mach number is nominally set at 2.2, under which conditions the pseudo-shock should have marginally entered into the full oblique shock-train regime, see Figure 3.11(e), that has been previous observed to occur for Mach numbers larger than 1.8-2.2 [29].

These two conflicting observations highlight a need to better understand the physical interplay between the normal shock and oblique shock-train regimes at lower values of flow confinement. During efforts to better understand this inconsistency, a mechanism for the breakdown of the normal shock-train and transition to an oblique shock-train has been observed, and is shown in Figure 3.12 in consecutive Schlieren images taken at 100 Hz. The steps in the breakdown mechanism are outlined in Figure 3.13, where frame references to Figure 3.12 are given.

As the isolator back pressure is raised, the mechanism begins as shown in Figure 3.12i and Figure 3.13i. Oblique shocks of a sufficient strength are created by the impingement of the pre-shock-train boundary-layer into the flow. The height of the leading normal shock is reduced by its intersection with these confinement induced oblique shocks, as seen in Figure 3.12ii and Figure 3.13ii.

A point will be reached when the oblique shocks have strengthened to the extent that the flow now entering the leading normal shock is insufficient to allow the normal shocks to continue to be stable. The leading normal shock is then found to collapse upon itself, forming a cluster of intersecting oblique shocks that are seen Figure 3.12iv, v and Figure 3.13iv, v. This cluster has a lifetime that is dependent on the flow confinement present in
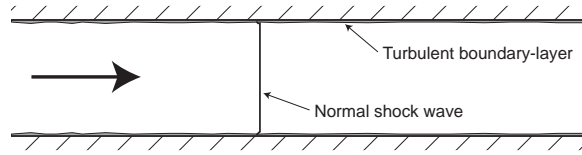
(a) Single normal shock at small δ/h.
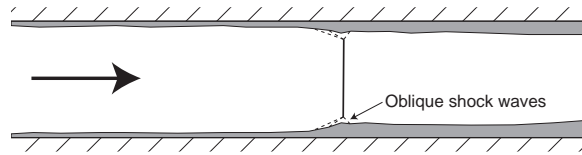
(b) Single branched-normal shock moderate δ/h.
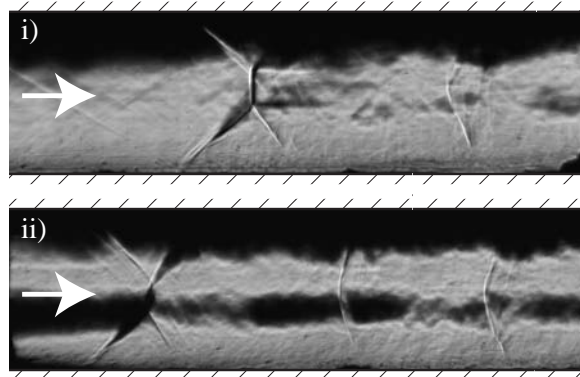
(c) Branched shock followed by bowed normal shocks L_p = 279.4-305 mm and δ/h = 0.224-0.302.
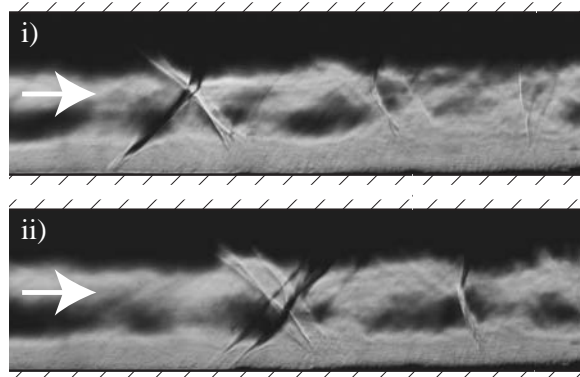
(d) Oblique shocks followed by bowed normal shocks L_p = 280 mm and δ/h = 0.121-0.122.
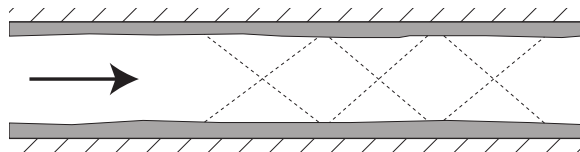
(e) Oblique shocks for large δ/h.

Figure 3.11: Shock-train stucture regimes possible in the constant area isolator section, for various run conditions.
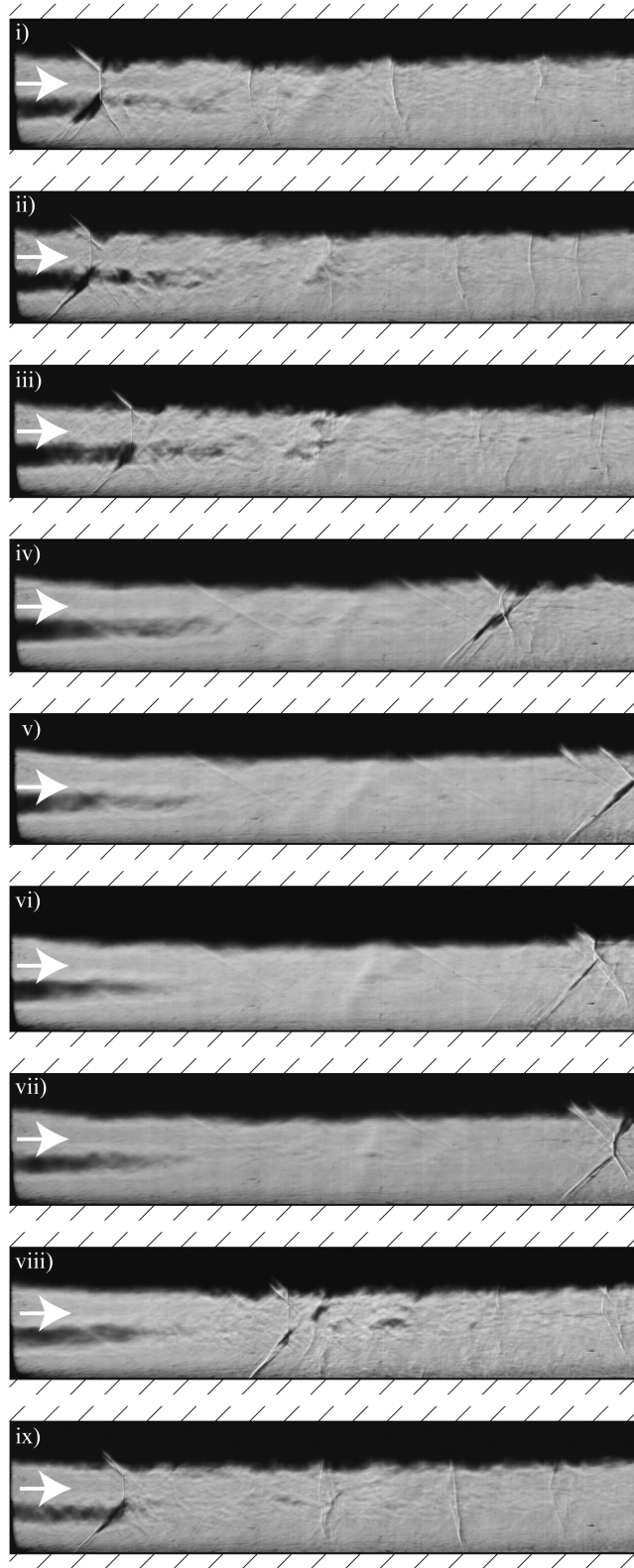
Figure 3.12: Proposed normal shock-train breakdown mechanism, shown in Schlieren imagery taken at 100 Hz, with knife-edge parallel to the flow, for a stagnation pressure of 448.2 kPa and temperature of 1200 K.

Frame(s)	
i	Oblique shocks of sufficient strength intersect leading normal shock.
ii, iii	Height of normal shock is reduced by interference of oblique shocks, with branches protruding further into the channel.
iv, v	Leading shock-structure becomes a cluster of oblique shocks as normal shock is destroyed.
vi, vii	Branched-normal shock is re-established usually with oblique shocks crossing up-stream of the normal shock.
viii, ix	Leading shock surges forward in the isolator, before returning to initial location.

— Normal Shock Wave
···· Oblique Shock Wave

Figure 3.13: Proposed normal shock-train breakdown mechanism, shown in illustration, with references to Schlieren image frames in Figure 3.12.

the isolator. If the confinement is insufficient to perpetuate the oblique shock structure, a leading normal shock will reform, followed by a surge forward in the position of the entire shock-train in the isolator, seen in Figure 3.12viii and Figure 3.13viii. After the re-establishment of the leading normal shock a pair of oblique shocks are found to cross just upstream of this location. The significance of this formation is under examination.

The frequency of this cycle, and the oblique shock lifetime, was found to increase not only for instances of increased flow confinement, but also for cases demanding higher back pressures, or pressure recovery, from the shock-train. An increased pressure rise across the leading normal shock will create an thicker post-shock boundary-layer thickness [46]. This in-turn will weaken the normal shock at its upper and lower edges, allowing a weaker oblique shock to initiate the normal-to-oblique shock-train transition.

A single mechanism now can be used to describe the inconsistencies in previous shock-

train regime observations. Figure 3.14 is a shock-train regime diagram incorporating these new effects. On the right of the diagram is the Oblique Shock Confinement Limit which occurs for large flow confinement. On the left side is the Normal Shock Compression Limit at low flow confinement.
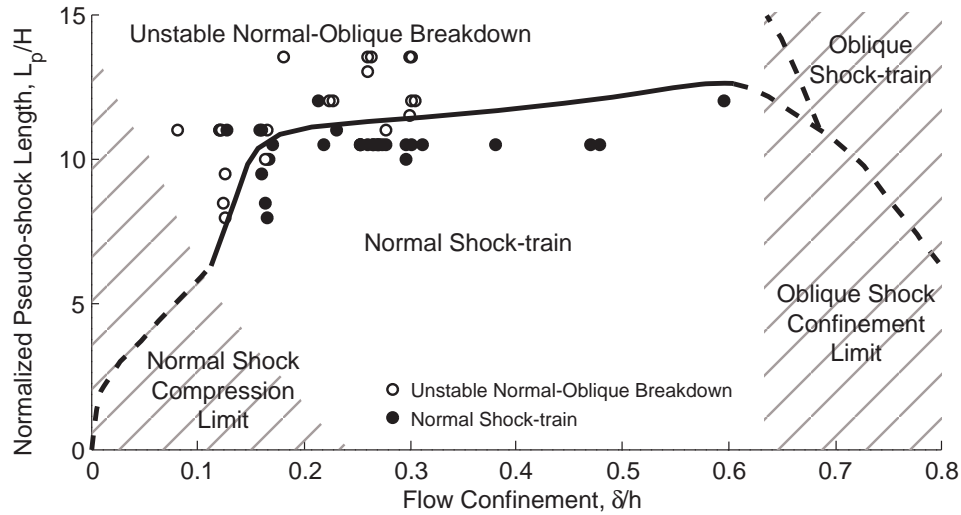
Figure 3.14: Pseudo-shock regime as a function of the flow confinement, δ/h, and the normalized pseudo-shock length, L_p/H. Observed stable normal shock-train behavior is shown as closed dots, and unstable behavior as open dots.

For intermediate values of flow confinement, the shock-train regime will be dictated by isolator inlet Mach number, the inlet stagnation conditions, and the pressure recovery demanded by the downstream blockage. All of these parameters influence the length of the pseudo-shock present in the isolator.

There is a change in slope at $\delta/h = 0.2$ of the steady normal shock-train boundary (solid line) with the region denoting the presence of the transition mechanism. This is due to the balance between a compressive efficiency dictated regime and the shock-train length dictated regime, for intermediate values of flow confinement. The longer a pseudo-shock becomes, it is more likely that oblique shocks are formed to provide the required compression.

At very low values of flow confinement and very short pseudo-shock lengths, the only

shock structure that can occur is a single normal shock. The only way to compress the flow in a short length is to have normal shock.

3.7 Conclusions for Isolator/Combustor Interaction Study

The behavior of the pseudo-shock created in a supersonic isolator by a hydrogen-air combustor has been studied for heated inlet flows up to 1400 K. It has been concluded that the flow blockage in the combustor is caused by both the combustion of the fuel and by the fuel-jet penetration into the isolator cross-flow itself. Both of these sources must be considered to adequately describe the combustor's influence on the downstream pseudo-shock anchor point and the maximum pressure recovery across the isolator. Fuel equivalence ratio and fuel-jet momentum ratio have been used to quantify these two coupled blockage sources, respectively.

The fuel injector developed blockage, and its influence on the maximum pressure recovery, plays a role in dictating the operating regime of the shock-train. This required the development of a new, more appropriate delineation of the operating regime of pre-combustion shock-trains. A plot of the flow confinement, δ/h, versus the normalized pseudo-shock length, L_p/H, describes this new operating space. In addition, a normal shock-train breakdown and transition to oblique shock-train mechanism has been experimentally observed using high-speed Schlieren imagery. This describes the transition between the discrete structural regions in the new operating regime space.

Based on the conclusion that the injector blockage has two contributing components, from combustion and from the jet itself, mappings were developed which show the relation between the fuel equivalence ratio, fuel-jet momentum ratio and the pressure recovered in the isolator. A methodology is designed to represent the intricate effects of isolator geometry, injector design and operating condition on the development of blockage in the

combustor and its coupling to the pre-combustion pseudo-shock. This isolator/injector mapping predicts the operation of the system for a set of given operating conditions.

CHAPTER IV

Investigation of Combustion Mode Transition and Flame/Shock-train Interactions

4.1 Case A$_2$: Ram-scram Transition Caused by Decreased Equivalence Ratio for Steady Conditions

As shown in Table 2.5, for Case A$_2$ the equivalence ratio was decreased from 0.337 to 0.187. The stagnation temperature was held fixed at 1400 K and the Mach number at the entrance of the isolator, M_1, was held at 2.17. The inlet stagnation pressure, P_o, was held at 448.2 kPa gauge. Values of momentum ratio, r, are listed in the table. As noted in Chapter III, increasing the equivalence ratio has two effects: it increases the flow blockage due to gas expansion as well as due to fluid-dynamic obstruction. The wall-normal fuel injection creates a region of momentum deficiency which will drive the flow to a choked condition. In its simplest form that is, even if the fuel did not burn, the added mass of a sufficient amount of fuel would eventually cause a scram-to-ram transition. Thus both heat and mass/momentum addition are coupled, as are the parameters ϕ and r.

The resulting pressure profiles are seen in Figure 4.1. The highest pressures occur for Case A$_2^1$, $\phi = 0.337$, and are due to a strong shock-train in the isolator. The curve A$_2^1$ shows that pressure increases in the isolator, but it decreases in the combustor in the x-direction, which indicates that the combustion is subsonic. Subsonic combustion drives the Mach number upward toward unity, while driving the static pressure downward in the

x-direction. As expected, decreasing the equivalence ratio causes the pressure profiles for cases A_2^2, A_2^3 and A_2^4 to decrease. Reduced heat-release rate in the combustor causes the combustor entrance Mach number, M_2, to increase and P_2 to decrease, according to Equations 1.1 and 1.5. That is, a reduction in equivalence ratio reduces the increase in Mach number between the entrance to the combustor and the thermal choking location. Due to the sonic conditions at the choking location, this means that the Mach number at the entrance to the combustor, M_2, must increase and P_2 must decrease as ϕ is decreased. This trend is observed in Figure 4.1. Also note that as the peak pressure is reduced, the length of the shock-train is similarly reduced from Case A_2^1 to Case A_2^4.

Ram-scram transition occurs in Figure 4.1 when the pressure profile abruptly decreases between Case A_2^4 (ram) and A_2^5 (scram). Note that Case A_2^5 displays almost no pressure rise in the isolator, because a pseudo-shock is not required in the scram-mode; a pseudo-shock is created because of the thermally choked downstream boundary conditions that exists in ram-mode only. Also note that for Case A_2^5 the pressure rises in the combustor, which is characteristic of supersonic combustion. In the scram-mode heat-addition drives the Mach number downward, toward unity, and the pressure upward. In all cases the pressure curves have a negative slope at far downstream locations in the diverging section, which acts like a supersonic nozzle.

It is clear that there is an abrupt change in the pressure profiles in Figure 4.1 during the ram-scram transition between Cases A_2^4 and A_2^5. The change is not gradual because the thermal choking boundary condition abruptly disappears as soon as the scram-mode is achieved.

Figure 4.1 shows that a decrease in the peak pressure recovery is accompanied by a decrease in pseudo-shock length. The location of this peak pressure recovery is in each case at the position of flame stabilization, as confirmed by the images in Figure 4.4 which will
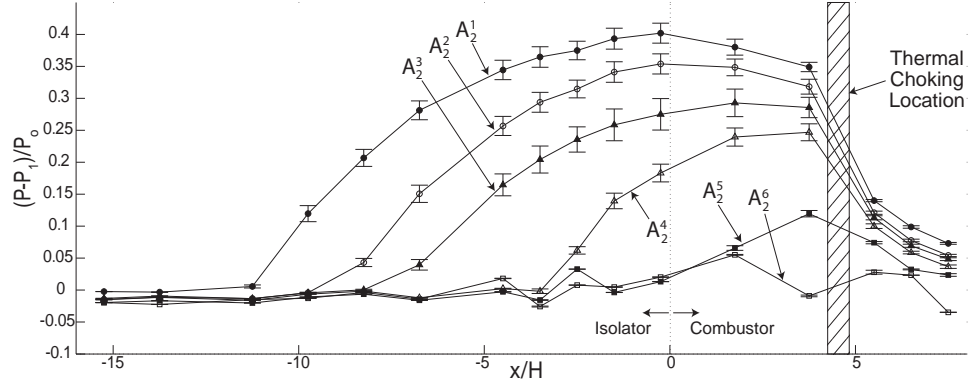
Figure 4.1: Static pressure traces showing operation of the test-section during: Case A_2^1, jet-wake flame stabilized Ramjet; Case A_2^2, lifted-jet flame Ramjet; Case A_2^3, mid-combustor flame Ramjet; Case A_2^4, cavity flame stabilized Ramjet; Case A_2^5, Scramjet and Case A_2^6, non-reacting operation. Duct height, H, is 25.4 mm. See Table 2.5 for test case conditions.

be discussed later. For Cases A_2^2 and A_2^3 the flame is less stable and sometimes oscillates; the pressures shown are time-averaged and the error bounds for Cases A_2^2 and A_2^3 are larger than for the others.

In the case of scramjet mode operation, Case A_2^5, the blockage is so small that the system is able to allow supersonic flow through the entire length of the combustor. Strong shock formations are not needed to allow the flow to adjust to the higher combustor pressures, and densities, that are created under other conditions.

The measured boundary where ram-scram transition occurs in the present experiment is shown in Figure 4.2.

Each point plotted in Figure 4.2 represent a single steady condition, i.e. a different run. The points were collected by varying the fuel equivalence ratio for three stagnation temperatures of approximately 1000 K, 1200 K and 1400 K.

A simple Rayleigh line analysis has been used to provide a one-dimensional theoretical estimate of the choking conditions in the ϕ-T_o space shown in Figure 4.2. This analysis assumes a frictionless constant-area flow with an addition of stagnation temperature. For the present case, this stagnation temperature change is due to the combustion of the fuel.

68
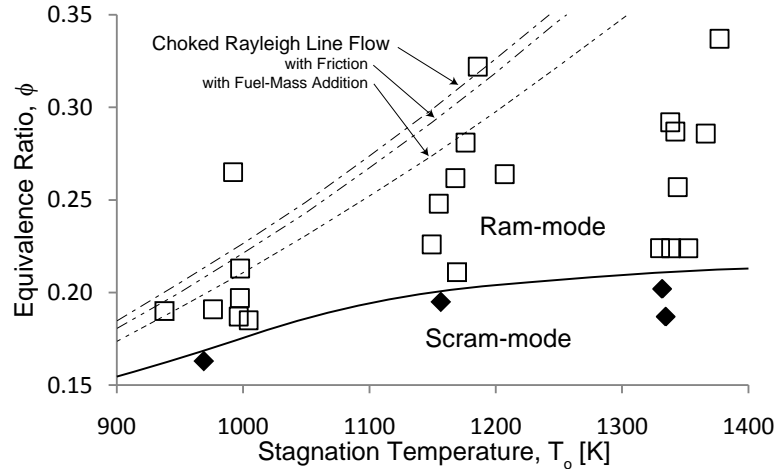
Figure 4.2: Combustion regime as a function of stagnation temperature, T_o, and fuel equivalence ratio, ϕ, at a stagnation pressure, P_o, of 448.2 kPa.

As compared to the experimentally observed ram-scram transition boundary, the Rayleigh line curve is seen to over-predict the amount of fuel required to drive the flow through the test-section to choked conditions. The deviation between these two curves grows as the stagnation temperature of the inlet cross-flow is increased. Curves representing the added effects of wall friction and fuel mass addition have also been computed and plotted. The friction coefficient used in the computation was based on that for a turbulent flat plate which ranged between $4.6 \cdot 10^{-4}$ and $5.9 \cdot 10^{-4}$, and was dependent on the gas composition for a particular stagnation temperature [51]. The fuel-mass addition was proportional to the equivalence ratio. While the addition of these effects does drive the one-dimensional prediction closer to the observed transition boundary, there still exists a substantial difference that can only be attributed to the impact of the boundary-layers present and dynamics of the flame, neither of which has been taken into account by the simple one-dimensional Rayleigh line analysis.

The operating regime of the combustor was classified as either ram-mode or scram-mode using two approaches. The first was the direct observation of the isolator pressure rise profile in which a large rise is indicative of ram-mode operation and a small, al-

ways positively sloped, increase indicates scram-mode operation. These classifications were confirmed through laser interferograms of the combustor in which weak, oblique shocks can be seen to be shed from the fuel injection location due to the disruption of the boundary-layer by the impinging fuel-jet.

The decrease in fueling conditions from Case A_2^1 through to Case A_2^6 creates a change in the flame anchoring location. This change also decreases the blockage to the inlet cross-flow created within the combustor. The system must compensate for the blockage in the combustor by creating a pseudo-shock structure upstream of the fuel injection location. The peak pressure recovered, $(P_2 - P_1)/P_o$, in each case is a direct function of the total amount of fuel injecting into the system, and can be seen from a simple Rayleigh line heat-addition analysis. For a frictionless gas in a constant-area duct this can be expressed via

(4.1)
$$\frac{dP}{P} = -\frac{\gamma M^2 \left(1 + \frac{\gamma - 1}{2} M^2\right)}{1 - M^2} \frac{dT_o}{T_o},$$

where the static pressure rise at any point is related to the local Mach number and the rate of stagnation temperature change, or the heat release distribution, in the duct [46].

Kilo-Hertz interferometry was applied to collect images of the flame boundary and the shock locations. The intense, disruptive luminosity of the flame made this method preferable to standard Schlieren or shadowgraph methods. Sample interferograms are shown in Figure 4.3. The dashed lines mark the shock locations while the solid lines identify the flame boundary. Interferograms normally are much more sensitive to the gas density field than a shadowgraph image, however they typically display a non-uniform background that must be carefully interpreted.

First, note that the shock wave on the left side of Figure 4.3(a) does not appear as a single line, but appears as a series of parallel lines which is typical of an interferogram. The shock is the downstream boundary of these lines. Shocks can be identified in the

interferograms by the presence of interference/diffraction fringe patterns in the images. These patterns are caused by the interaction of the coherent, monochromatic laser light with the step-increase in density associated with a shock wave. If the density were to take an infinitely large step-increase across that shock this pattern can be seen to be the exact same phenomenon that creates the diffraction of laser light around a knife edge, or through a slit aperture. The light, that in reality, traverses this denser downstream fluid will take a longer optical path through the test-section, and as such obtain a shift in phase compared to the light that traverses the test-section upstream of the shock. This phase difference between adjacent rays of light will add a layer of interference to the recorded image as well.

The flame boundary is identified as the edge of the fine-grained wrinkled region of density gradient. Contained within the region of highly convoluted density gradient is the hot downstream products of combustion. The images do not allow for the disposition of the flame to be determined, whether it is shredded due to high fluid-shear or perhaps more of a diffusion type structure. Unfortunately, a number of other background irregularities that are due to light wave interferences are seen in any interferogram; however, they can easily be separated from the useful data.

In Figure 4.3(b) the nearly-normal shock waves on the left represent the downstream end of the shock-train that exists in the isolator. A shock train can consist of a series of nearly-normal shocks; the flow decelerates across each shock but then it accelerates back to supersonic speeds because the thickening of the boundary layer causes the core flow area to decrease in the x-direction. The boundary-layer is not well-visualized in Figure 4.3 because the interferometry system was optimized to display density changes in the flow direction only.

In ramjet operation, the flame was found to anchor stably in either the jet-wake of the

(a) Interferogram of combustor under scramjet operation

(b) Interferogram of combustor under ramjet operation
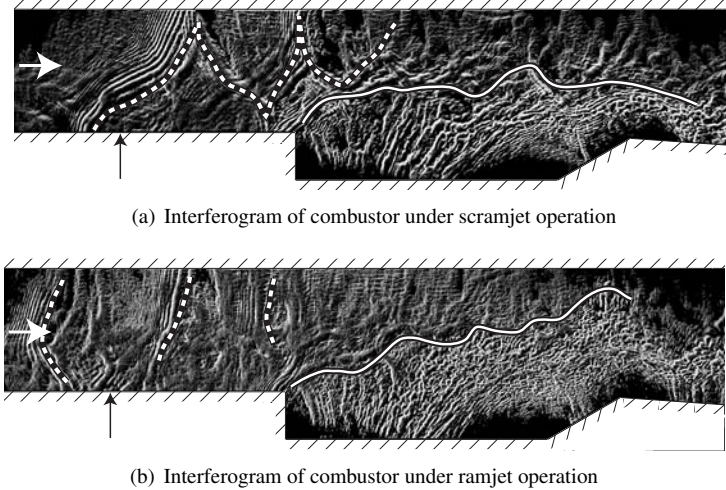
Figure 4.3: Sample interferograms taken at 1000 frames/sec, with shock boundaries (dashed lines) and flame boundaries (solid lines) highlighted. Scram mode image (a) displays a single weak oblique shock that is caused by the fuel jet; this shock reflects off the upper wall. Ram mode image (b) displays three nearly normal shocks. Flame is identified by fine-grained density gradients.

fuel plume or on top of the shear-layer that exists across the mouth of the cavity. Interferograms showing these two anchoring mechanisms are given in Figure 4.4(a) and 4.4(d), for Cases A_2^1 and A_2^4 respectively, with schematics of the various flow structures in Figure 4.5(a) and 4.5(d). These two mechanisms represent the forward and rear bounds of flame stabilization within the combustor and are obtained by lowering the fueling conditions for the same cross-flow conditions, Cases A_2^1 and A_2^4 respectively. The dark circular feature located at the angled rear cavity wall, and found in all the images that will be presented here, represents the region of low density gradient created by the partial stagnation of the flow at this location, and the subsequent high heating loads it produces.

In Figure 4.4(a) the flame can be seen to stabilize directly downstream of the fluid-mechanical obstruction created by the wake of the fuel-jet. An image showing the test-section for Case A_2^6, a non-reacting condition, is given in Figure 4.4(f) for reference. The cavity stabilized case (Figure 4.4(d)) shows that the flame is located much further downstream and that normal shocks from the tail-end of the isolator pseudo-shock are present in the flow above the fuel injector.
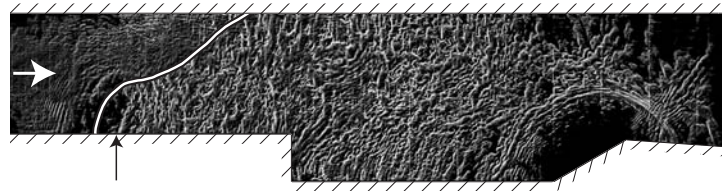
(a) Case A_2^1: Jet-wake flame stabilized operation, $\phi = 0.337$
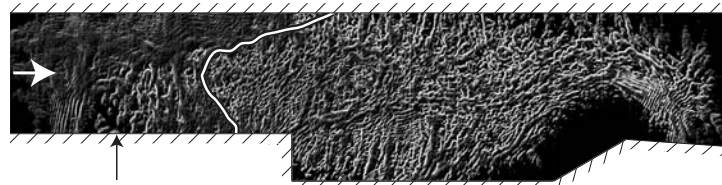
(b) Case A_2^2: Lifted-jet flame operation, $\phi = 0.286$.
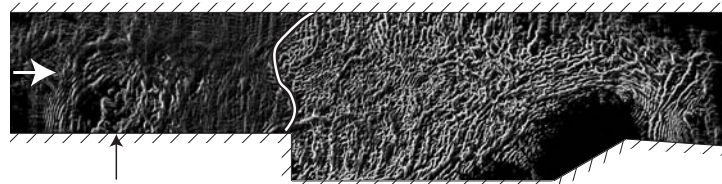
(c) Case A_2^3: Mid-combustor flame operation, $\phi = 0.257$.
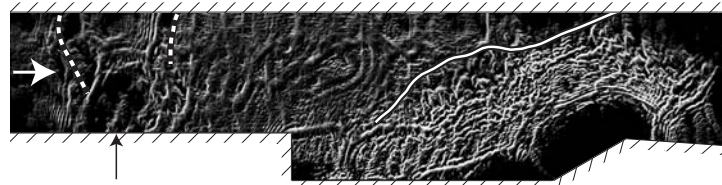
(d) Case A_2^4: Cavity flame stabilized operation, $\phi = 0.224$.
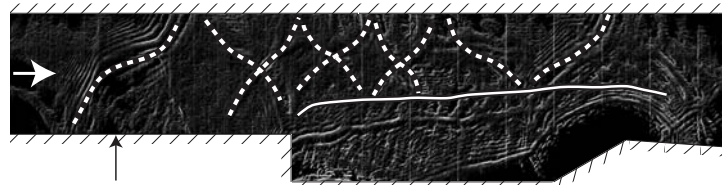
(e) Case A_2^5: Scramjet operation, $\phi = 0.187$.
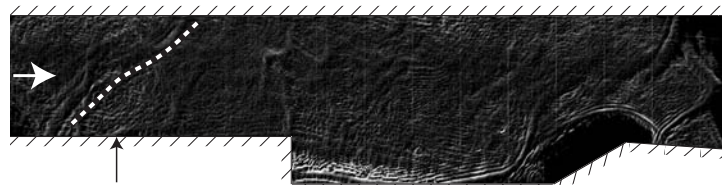
(f) Case A_2^6: Non-reacting operation, $\phi = 0.0$.

Figure 4.4: Shearing interferogram of the combustor in: (a) Case A_2^1, jet-wake flame stabilized Ramjet; (b) Case A_2^2, lifted-jet flame Ramjet; (c) Case A_2^3, mid-combustor flame Ramjet; (d) Case A_2^4, cavity flame stabilized Ramjet; (e) Case A_2^5, Scramjet and (f) Case A_2^6, non-reacting operation.

(a) Case A_2^1: Jet-wake flame stabilized Operation, $\phi = 0.337$.

(b) Case A_2^2: Lifted-jet flame operation, $\phi = 0.286$.

(c) Case A_2^3: Mid-combustor flame operation, $\phi = 0.257$.

(d) Case A_2^4: Cavity flame stabilized operation, $\phi = 0.224$

(e) Case A_2^5: Scramjet operation, $\phi = 0.187$.

(f) Case A_2^6: Non-reacting operation, $\phi = 0.0$.
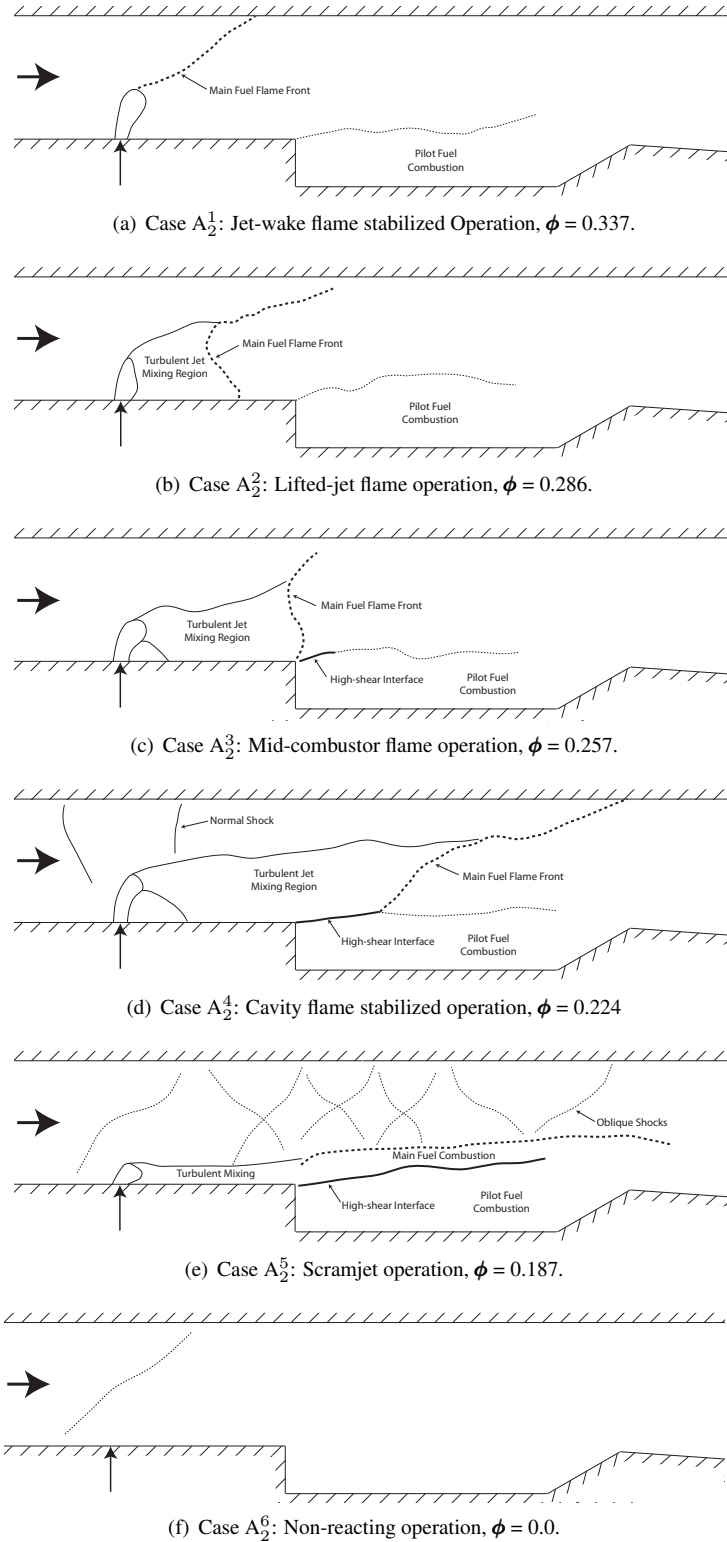
Figure 4.5: Schematics of the combustor in: (a) Case A_2^1, jet-wake flame stabilized Ramjet; (b) Case A_2^2, lifted-jet flame Ramjet; (c) Case A_2^3, mid-combustor flame Ramjet; (d) Case A_2^4, cavity flame stabilized Ramjet; (e) Case A_2^5, Scramjet and (f) Case A_2^6, non-reacting operation.

The presence of these shocks within the combustor section is important, highlighting the need to approach the ramjet/scramjet system as a single continuous device and not simply two separate components with coupled features. The two flame stabilization modes, jet-wake and cavity modes, are examined in detail by Micka and Driscoll [35] who applied OH planar laser induced fluorescence diagnostics.

Figures 4.4(b) and 4.4(c), with schematics provided in Figure 4.5(b) and 4.5(c), are images for Cases A_2^2 and A_2^3, and show two intermediate flame positions between the jet-wake and cavity stabilization modes. These are not stable locations at which the flame naturally stabilizes. The images given for Case A_2^2 and A_2^3 represent two snapshots of a flame that will move unsteadily between the jet-wake and cavity stabilization mode positions. The higher fueling condition of Case A_2^2 provided a more forward bias to the mean flame position as compared to Case A_2^3, which will be discussed further in Section 4.4 along with the dynamic behavior of the flame front under such conditions.

Case A_2^5 is a scramjet condition for which the flame is stabilized in the cavity shear-layer. This is shown in Figures 4.4(e) and 4.5(e). There are oblique shocks present in the combustor under these conditions. These are created by the interaction of the cross-flow with the disturbed boundary-layer upstream of the impinging fuel-jet. The operation of the test-section in either ramjet or scramjet modes is determined by the amount of mechanical and combustion flow blockage developed by the fuel injector. The mechanical blockage is the contribution of the momentum-flux and turbulent mixing associated with the fuel plume, while the combustion blockage is created by the consumption of fuel and oxidizer, and the subsequent expansion of the hot products.

The series of images in Figure 4.4 are taken along a line of constant stagnation temperature in Figure 4.2. As the fuel equivalence ratio and inlet stagnation temperature are increased the local flame speed of the flame front is increased as well. This allows for the

main fuel flame to begin to propagate further upstream for a given inlet condition.

An increase in fuel equivalence ratio is accompanied by an increase in the fuel-jet momentum ratio. This creates a larger fluid-mechanical obstruction at the location of the fuel injector. As the size of this obstruction, or jet-wake, grows it provides a more suitable location at which flame stabilization may occur. This mechanism allows for the flame anchoring location to move from the cavity to the jet-wake.

The discrete nature of the ram-scram transition should be noted at this point. In Figure 4.1, the pseudo-shock pressure rise profile is seen to vary in a smooth manner between the states described by Cases A_2^1 through A_2^4 as the equivalence ratio is reduced. This behavior is consistent with a Rayleigh line description of the heat-addition process to a subsonic flow. Case A_2^4 represents a fueling condition just above the point at which the flow transitions from ramjet mode to scramjet mode operation. Once below this threshold condition, the thermal throat at the combustor exit becomes unchoked and a discrete drop in peak pressure recovery is observed, as seen in Case A_2^5. As the equivalence ratio is reduced further, a smooth reduction in the pressure profile occurs again, in a Rayleigh line consistent fashion, until the non-fueled condition of Case A_2^6 is reached. The pressure profiles associated with the fueling conditions just above and below the ram-scram threshold form bounds for a set of pressure profiles that are not allowed under the current set of inlet stagnation conditions and device geometry. Such profiles would be consistent with flow states that violate the thermal choking boundary condition at the combustor exit.

4.2 Case B_2: Ram-scram Transition Caused by Rapid Decrease in Equivalence Ratio

Another set of pressure profiles were recorded for Case B_2; the equivalence ratio was rapidly decreased during a 90 msec time period. Figure 4.6 shows the equivalence ratio and Figure 4.7 shows the static pressure profile as a function of time. The ram-to-scram

transition was observed for the conditions listed in Table 2.6.
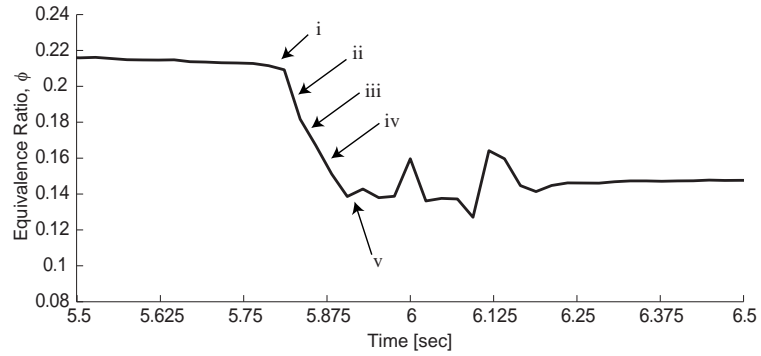
Figure 4.6: Main fuel equivalence ratio as as a function of time during mode transition from ramjet to scramjet operation for Case B_2, with frame locations indicated for Figure 4.8.

Figure 4.7: Static Pressure traces of mode transition from ramjet to scramjet operation for Case B_2, with frame locations indicated for Figure 4.8.

In the five consecutive schematic images of recorded interferograms, given in Figure 4.8 with an effective frame rate of 50 Hz, the different stages of the transition are shown. Under a high fueling condition the combustor can be seen in Figure 4.8i (Case B_2^1) to operate in ramjet mode with the main fuel flame stabilized by the cavity. For reference, the timing of the images in Figure 4.8 with respect to fueling condition is shown in Figure 4.6.
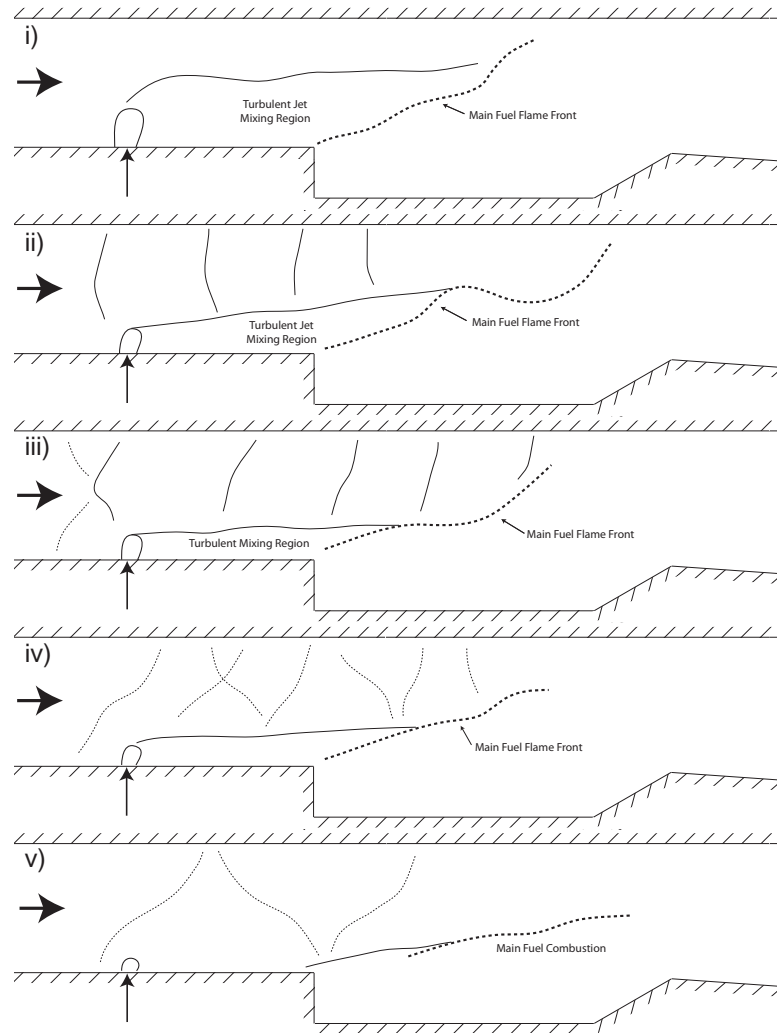
Figure 4.8: Schematics of combustion mode transition from ramjet to scramjet operation for Case B_2. The effective frame rate of the images is 50 Hz.

As the fueling is initially decreased, the tail-end of the pseudo-shock begins to drop further back into the combustor. In Figure 4.8ii (Case B_2^2) successive normal shocks are seen to span the flow region directly above the fuel injector. The combustor is still operating under ramjet mode with a cavity stabilized flame. Further reduction in fuel brings the collapse of the entire shock-train structure into the combustor. At the left of Figure 4.8iii (Case B_2^3) a large "K" shock formation is visible, indicating that the entrance of the pseudo-shock has reached the fuel injector with the entire shock-train visible within the combustor. The combustor is still operating strictly under ramjet mode, by the size of the

cavity stabilized flame is substantially reduced compared to the two earlier frames.

The instant that portions of the flow through the combustor becomes supersonic occurs between image iii and iv in Figure 4.8 (Cases B_2^4 and B_2^5 respectively). The leading shock is now a curved oblique shock anchored to the boundary-layer obstruction upstream of the fuel injector. On close examination, a number of oblique shocks are seen to exist while the flame continues to be cavity stabilized. The combustor is now operating in an early scramjet mode of operation.

The transition event is concluded by the establishment of a steady scramjet flow pattern as in Figure 4.8v (Case B_2^5). The only shocks that are visible are the oblique shocks shed by the impingement of the fuel-jet into the test-section. Given the lack of penetration of the flame vertically into the combustor, and no evidence of flow structures locally around the fuel injector, the fuel is believed to be streaming down the lower wall of the test-section and then into the shear-layer present over the cavity. The main fuel combusts above the cavity in a similar location as under cavity stabilized ramjet mode operation, but with the expected decrease in intensity due to the lower fueling levels.

The fuel flow rate decreases during a 90 msec interval as seen in Figure 4.6. Sequential imaging showed that the flow structures and combustion present within the test-section adjusted quickly compared to this 90 msec timescale. The transition between combustion modes is quasi-steady; it was completed as soon as the final fuel state was reached. In effect this creates a situation similar to that described in Section 4.1 for Case A_2, where the steady-state influence of a decreased fuel equivalence ratio was examined.

4.3 Case C_2: Scram-ram Transition Caused by Increasing Wall Temperature

A somewhat surprising observation was made when the combustor was first operated in the scram-mode and the combustor wall temperature was allowed to increase in time.

A previous section describes steady-state (Case A_2) operation for which the flow was run for 11 seconds to achieve steady conditions. For Case C_2 the measurements were taken after only 6.6 seconds during which unsteady wall heating still occurs. A scram-to-ram transition was observed for the conditions that are listed in Table 2.7.

As the wall temperature rises in time, the measured pressure profiles are plotted in Figure 4.9. Note that there is a sudden increase in the pressures from a scram to a ram profile, as a shock-train is formed in the isolator due to the abrupt imposition of a down-stream choked flow boundary condition. During this transition the equivalence ratio is held constant at 0.185.
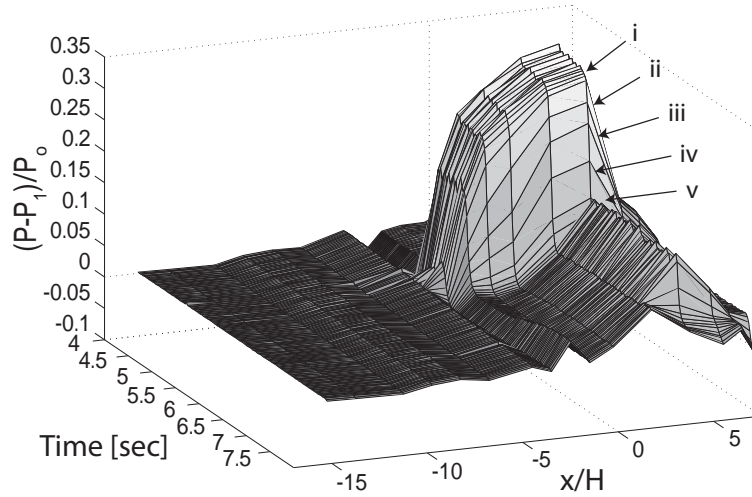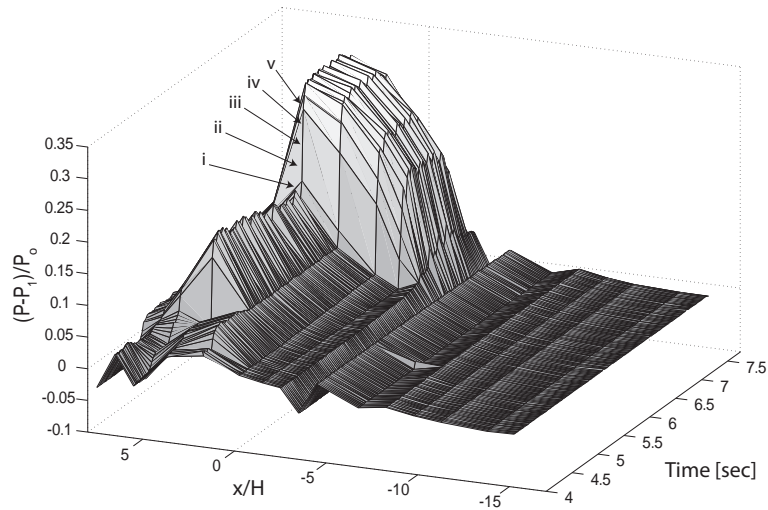

Figure 4.9: Static Pressure traces of mode transition from scramjet to ramjet operation for Case C_2, with frame locations indicated for Figure 4.10.

The physical explanation for this phenomena is believed to be the following. As the wall temperature is allowed to increase, there will be less heat transfer to the wall since heat transfer is proportional to the difference between the free-stream stagnation temperature and the wall temperature. This means that for higher wall temperatures, more of the combustion heat-release will go into heating the air flow, and less will be lost to the walls. So an increase in wall temperature is equivalent to an effectively larger heat-release from

the combustion process, and this would tend to cause the scram-to-ram transition that is observed.

A series of schematic images from recorded interferograms are provided in Figure 4.10 that show the mode transition from scramjet-to-ramjet operation for the conditions given in Table 2.7. Prior to the onset of transition in Figure 4.10i (Case C_2^1) a steady scramjet mode flow structure is present. A series of oblique shocks are created by the impingement of the fuel injection, and the main fuel combusts across the cavity shear-layer. The static pressure profile in the test-section, from inlet-to-exhaust, shows that the combustor is operating under an early scramjet mode. The timing of each image in Figure 4.10 with respect to the static pressures recovered in the test-section is given in Figure 4.9 by the symbols i-v.

As the transition progresses, Figure 4.10ii shows that for Case C_2^2 the oblique shocks in the combustor begin to compress forward. The leading oblique shock is still anchored at the location of the fuel injector. The flame at the trailing-end of the cavity has strengthened, penetrating further into the core of the flow.

In Figure 4.9iii normal shocks are seen to form in the combustor, above the fuel-jet. The presence of normal shocks indicates that thermal choking has occurred. Figure 4.10iii (Case C_2^3) shows that the fuel-jet is still anchoring a shock, but that the compressed series of oblique shocks has become a set of normal shocks. The combustor is now operating under ramjet mode operation.

The peak pressure recovery within the combustor continues to rise as the transition progresses. The normal shock formations continue to strengthen in Figure 4.10iv, eventually leading to the establishment of a steady ramjet shock structure in Figure 4.10v (Cases C_2^4 and C_2^5 respectively). The tail-end of the pseudo-shock sits above the fuel-jet in this steady state. The flame is stabilized by the cavity.

It should be reiterated that the only aspect of the flow that has been altered between
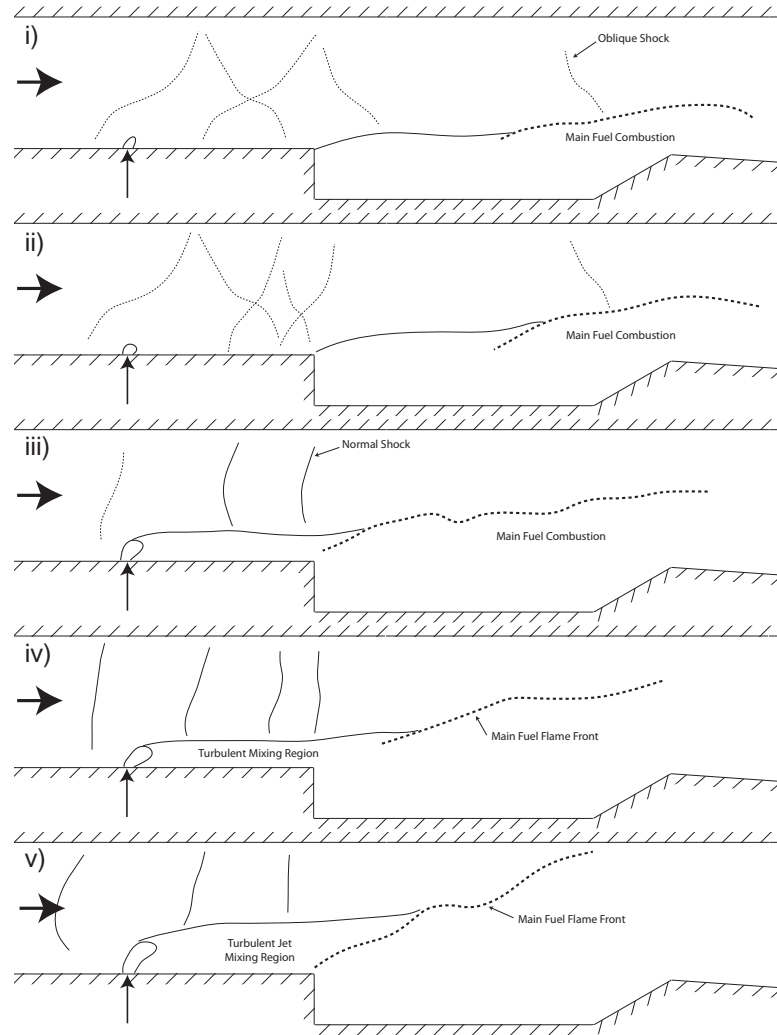
Figure 4.10: Schematics of combustion mode transition from scramjet to ramjet operation for Case C_2. The effective frame rate of the images is 100 Hz.

Figure 4.10i and 4.10v is that the thermal boundary-layers have been allowed to evolve over time. This naturally occurs under all test conditions, but here it is seen to trigger a wholesale, discrete change in the operation of the test-section. The quantity of fuel being injected has not changed, only the manner in which the fuel is consumed and its energy deposited.

The timescale for this passively actuated transition to be completed was 0.018 ± 0.002 seconds, as observed from the 1 kHz imaging. This transition provides a minimum scram-to-ram transition time as the actuation time of the trigger is dependent on the structure of

the flow itself, initiating the transition once the boundary-layer has sufficiently evolved. This is different from the instance of ram-to-scram transition discussed earlier, as the pressure controller used to actuate the main fuel pressure has a physically limited, finite response time.

4.4 Case D_2: Dynamics of Ram-mode Flame Oscillations

Under certain conditions that are listed in Table 2.8, the flame was observed to undergo periodic low frequency oscillations; the mechanism was identified as being associated with a shear-layer instability across the flame holder wall cavity. It is not argued that these flame oscillations are of a general nature; instead they are believed to be geometry-specific. However they do offer an interesting way to observe how the upstream shock-train responds to downstream periodic flame oscillations, and to measure the relevant time scales of the flame-shock interaction.

Once above a particular threshold fueling condition, which is a function of stagnation temperature, there exists a region where the two stabilization modes, the jet-wake and cavity modes, are in competition given the instantaneous state of the flow within the combustor. This is the unsteady behavior described earlier as observed for Cases A_2^2 and A_2^3.

Micka and Driscoll originally reported this transition between mean flame stabilization locations as a function of stagnation temperature, where an increase drove the flame anchoring position upstream toward the fuel injector. This, in effect, alters both the flame speed and mechanical blockage components of the flame stabilization mechanism. A higher stagnation temperature leads to a higher static temperature at the fuel injector which is both easier to be obstructed by the fuel-jet and promotes more rapid combustion. They also directly studied the impact of decreasing the flame speed on the system through the use of a mixture of hydrogen and ethylene as a fuel. This was found to retard the transition

to the jet-wake stabilization regime by preventing the flame from being able to physically propagate forward in the combustor until much higher fueling conditions were reached.

4.4.1 Flame/Shock-train Interaction

The implications of the location of flame stabilization within the combustor on the system as a whole can be examined by considering a single ramjet case (Case D_2^1) which displays unsteady flame stabilization. During this single case, as Figure 4.11 shows, the flame can be present in the forward jet-wake stabilized location, the rearward cavity stabilized location and an intermediate lifted jet location. The static pressure traces corresponding to each of the three images in Figure 4.11 is provided in Figure 4.12.

(a) Jet-wake stabilization

(b) Lifted jet stabilization

(c) Cavity stabilization
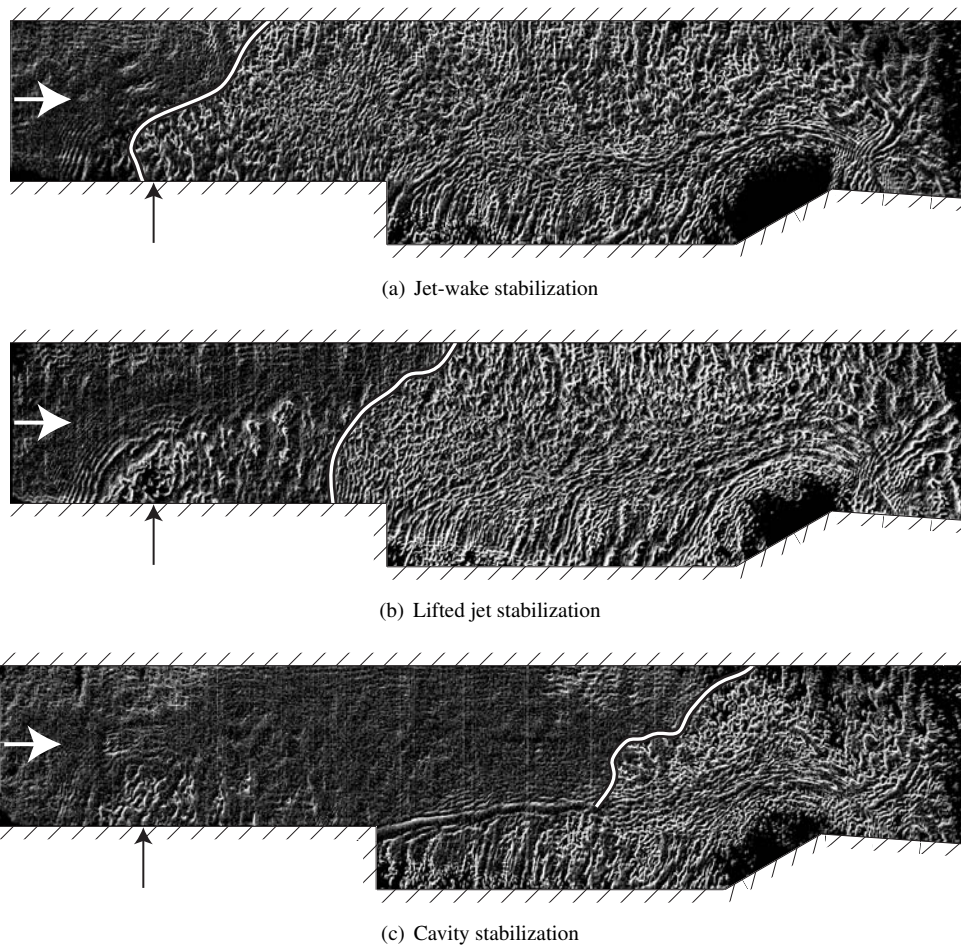
Figure 4.11: Shearing interferograms of the (a) jet-wake, (b) lifted jet and (c) cavity flame stabilization modes for Case D_2^1.
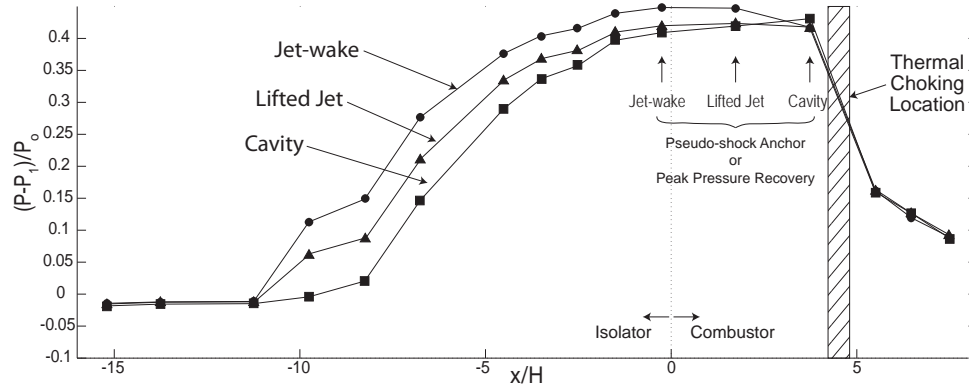
Figure 4.12: Static pressure traces showing the effect of flame stabilization position on the pseudo-shock downstream anchor location for Case D_2^1. See Table 2.8 for test case conditions.

The peak pressure recovered in each instance is comparable, as would be expected because the same amount of fuel is being burned. However, the location of the peak pressure recovery, or pseudo-shock downstream anchor point, does vary with the location of the main flame within the combustor. As the flame moves from the cavity stabilized location, the pseudo-shock anchor point moves forward from the thermal choking location, to a mid-combustor location and then to the fuel injector location itself. The anchor location change, while not impacting the pressure recovery required of the up-stream pseudo-shock, shifts the entire pseudo-shock structure forward in the isolator portion of the test-section. The axial location of the initial static pressure rise shows this by shifting forward proportional to the forward shift in the flame location. The pseudo-shock does not get longer or stronger, but rather adjusts to allow for a change in the application point of the maximum blockage in the combustor. This point of maximum blockage is the main flame front as confirmed by the images in Figure 4.11.

The leveling-off of the profiles in Figure 4.12 at $x = $ -10 is not due to the fluctuation in flame location. Instead, it is caused as the leading-edge of the shock-train changes from a normal to an oblique shock structure. This behavior, as well as the mechanism causing it, is described by Fotia and Driscoll [13].

Figure 4.13 shows a revised version of Figure 4.2 that now includes the various combustion stabilization modes that have been observed. Under ram-mode operation and for low stagnation temperature the flame stabilizes in the shear-layer of the cavity. As the stagnation temperature or equivalence ratio is increased the flame enters into an oscillatory regime in which there appears to be a competition between the jet-wake and cavity stabilization modes. Both these parameters influence the combustion flame speed and as such must be coupled to the mechanism driving the oscillations in this way. For high stagnation temperature and fueling conditions, a pure jet-wake stabilization is attainable. The increased stagnation temperature reduces the required fuel residence time for combustion stablization, while the increased equivalence ratio is linked to an increased momentum ratio which allows the creation of a larger fluid-mechanical obstruction that more easily provides this, now reduced, residence time to anchor the flame.
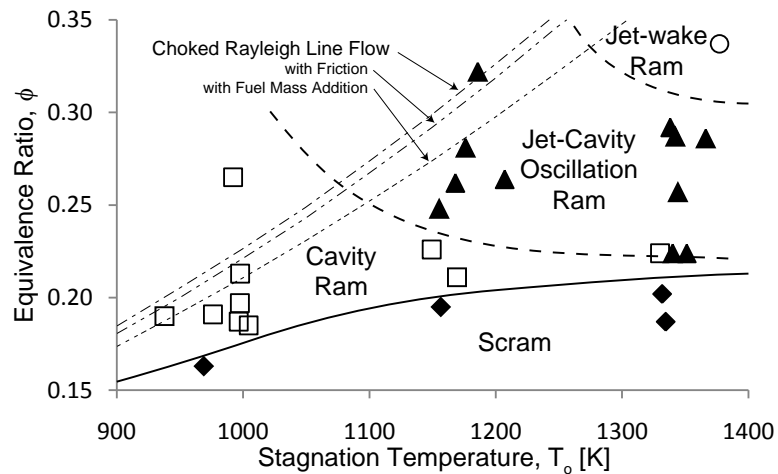
Figure 4.13: Flame stabilization modes (cavity ram, jet-wake ram and jet-cavity oscillation) added to regime diagram as a function of stagnation temperature, T_o, and fuel equivalence ratio, ϕ, at a stagnation pressure, P_o, of 448.2 kPa.

Figure 4.13 shows that the deviation between the Rayleigh line heat-addition curve and the experimental ram-scram transition boundary grows with the inlet stagnation temperature of the flow. This also occurs as the level of observed flame dynamics increases,

indicating that there is a relationship that is not yet understood between the behavior of the flame and manner in which the released heat chokes the combustor flow.

4.4.1.1 Transient Flame Behavior

The location of the flame within the combustor is a function of the fueling conditions, ϕ and r, and the stagnation temperature, T_o, of the inlet flow to the combustor. The axial position of the flame inside the combustor can be identified by averaging the recorded image intensity across each vertical slice of an image to create a one-dimensional axial image intensity profile. From the interferograms, the flame front is identified as being the location of the inflection point in this one-dimensional profile.

Figure 4.14 is a histogram showing that the flame position oscillates over a fairly large distance; this distance is the width of the histogram and it is approximately x/H = 3-4 (H = 25.4 mm) for all cases. However, the center of the histogram is seen to move upstream or downstream as the equivalence ratio and stagnation temperature are varied. This movement is due to the fact that at high stagnation temperatures the flame is stabilized in the wake of the fuel-jet, while at lower T_o it stabilizes in the cavity shear-layer [35].

Figure 4.14(a) shows that as the fuel equivalence ratio and jet-momentum ratio are increased from a cavity stabilized condition (Case A_2^4) to a jet-wake stabilized condition (Case A_2^1 through Case A_2^3 and A_2^2) the probability of finding the flame in a more forward position dramatically increases. The same is true if the inlet stagnation temperature is increased, from Case D_2^1 to Case A_2^1, as shown in Figure 4.14(b).

Figure 4.15 is a plot of the spectrum of the flame position and spectra of the pressure transducers positioned at locations 3 through 6, shown in Figure 2.1. These four locations span the approximate leading edge location of the pseudo-shock for Case D_2^2, which is located primarily between locations 4 and 5, and were sampled at 10 kHz by a LeCroy Waverunner 6100A oscilloscope. For this condition, Figure 4.15 shows that a sharp peak

in the flame position spectrum occurs at 4.88±0.48 Hz. The leading edge of the pseudo-shock is found to have the same periodicity, through the pressure spectra. Again it is noted that much higher frequency oscillations may occur in real engines, so it is not argued that this oscillation is representative of scramjet dynamics, but it offers a way to investigate low frequency flame-shock interactions.
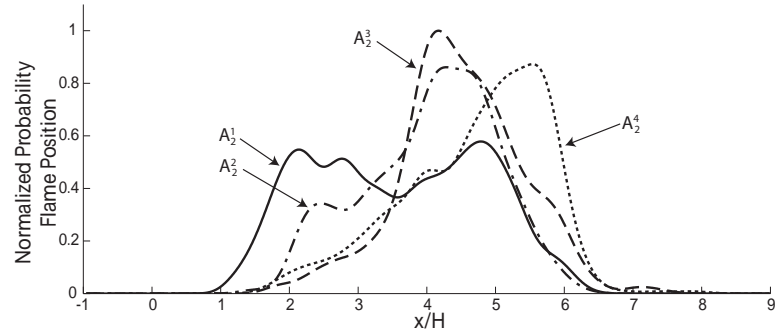
(a) Flame position dependence on fueling condition.
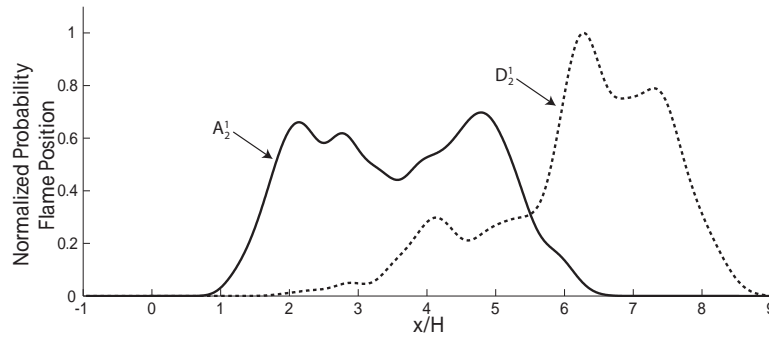
(b) Flame position dependence on stagnation Temperature.

Figure 4.14: Flame position as function of (a) fueling conditions, ϕ and r, and (b) isolator inlet stagnation temperature, T_o. See Tables 2.5 and 2.8 for test case conditions.

Figure 4.16 shows a time history of the periodic oscillations of the flame position and the pressures at locations 3 through 6 on the isolator wall. The pressure oscillations are due to the periodic motions of the shock-train in this ram-mode. First note that all four curves are very periodic, so these are not random motions. The peak value of the flame leading-edge curve represents the farthest upstream location of the flame front; the minimum value of this curve represents the farthest downstream value. The peak value of each pressure curve indicates that a shock wave in the shock-train has moved upstream of the
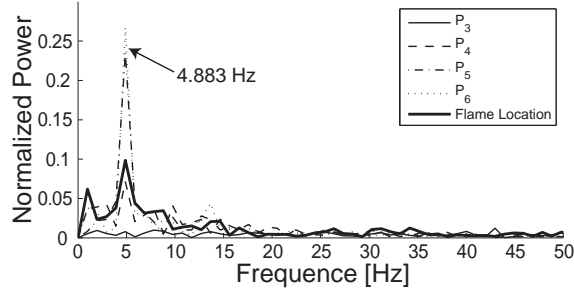
Figure 4.15: Spectra showing the dominant frequencies of the flame position and the pressure transducers in the isolator for Case D_2^2.
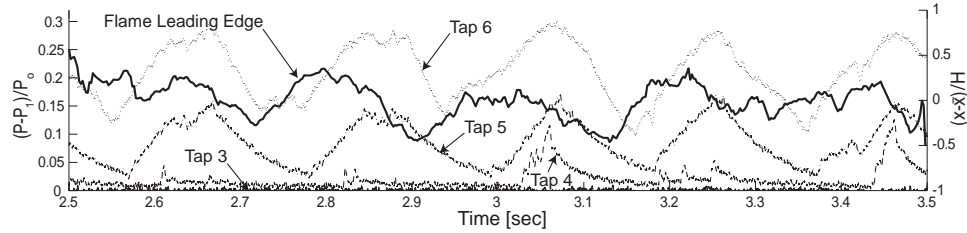
Figure 4.16: Isolator shock-train static pressure traces for tap locations 3 through 6 overlaid with flame position as a function of time for Case D_2^2. x/H locations of tap 3 (-6.420), tap 4 (-5.564), tap 5 (-4.7079) and tap 6 (-6.8517). Flame position is plotted relative to the mean, $\bar{x}$.

transducer, causing a pressure rise at the transducer. From these plots it can be seen that all of the pressure transducers are in phase; they all have peak values at approximately the same times. The shock-train is moving as a single entity in the upstream and downstream directions. Figure 4.16 also shows that there is a clear phase difference between the flame and isolator pressure signals; this phase difference was measured to be 88 degrees by analyzing the signals with a standard Fourier analysis.

The phase offset represents the time delay for the information that the flame has moved to propagate forward to the entrance of the pseudo-shock through the subsonic boundary-layers present around the supersonic core flow in the isolator section. The forward propagation speed of information can be calculated from the known geometry of the test-section by

$$(4.2) \qquad \frac{\Delta x}{\Delta t} = \frac{x_{\text{Flame}} - x_{\text{Pressure Tap}}}{T \cdot \theta / 360^o} = \frac{0.1714 \text{ m}}{0.2 \text{ sec} \cdot 87.91^o / 360^o} = 3.51 \pm 0.40 \text{ m/s},$$

using the pressure signal from location 6 and its offset from the flame of about 88°.

Wagner et al. [48] examined the propagation of unstart in an inlet/isolator model. They reported an average forward propagation speed of approximately 26 m/s, while using tank temperature air and with a boundary-layer momentum-thickness Reynolds number of Re_θ = 39,000. The difference between this propagation speed (3.51 m/s) and that observed for the present study is due to the heated flow effects. The boundary-layer momentum-thickness Reynolds number for Case D_2^2 is Re_θ = 625, and while the momentum-thickness is roughly a third of that in Wagner et al.'s work, the Reynolds number is less in the present work due to the dramatic increase in the kinematic viscosity associated with the highly-heated flows that are present. This increased damping behavior of the subsonic boundary-layer lowers the response time of the upstream pseudo-shock structure to variations in the downstream boundary conditions.

The unsteady behavior of the shock-train is actually the pseudo-shock structure adjusting to a new downstream anchor position dictated by the fluctuations in main flame front present in the combustor, and their associated impact on the position of the peak pressure recovered in the test-section.

Rowley et al. [44] describe two self-sustaining oscillations that have been observed to exist in the compressible flow over rectangular cavities. A shear-layer mode of oscillation, first seen by Rossiter [43], in which small disturbances in the free shear-layer spanning the cavity are amplified via the Kelvin-Helmholtz instability. The Strouhal number, $St = fL/U$, based on the cavity depth, associated with this instability was between 0.2 and 0.3. A second, wake-mode of oscillation was identifed by Rowley et al. [44] from the previous experiments of others and their own numerical simulations. This oscillatory mode is associated with large vortical structures forming in the shear-layer spanning the cavity, usually occurring for longer cavity lengths and at Strouhal numbers between 0.064 and

0.054 depending on flow and cavity configuration.

Calculating the frequency for these two self-sustaining oscillations for the flows present in the combustor gives frequencies on the order of hundreds of Hertz. Oscillations at such frequencies are not observed in the data collected. The physical reason for the periodic low frequencies seen in Figure 4.16 is believed to be the following. The oscillatory behavior of the flame stabilization location, for intermediate fueling conditions, begins with the local flame speed exceeding the local flow speed either due to residence time, equivalence ratio or static temperature effects. This causes the flame to move forward at a speed that forcibly excites the self-sustaining shear-layer instability of the cavity. The flame causes a peak in the pressure profile and so this pressure peak would move forward with the flame. These pressure oscillations then couple back into the flame speed and flame stabilization location, giving the flame, and the pseudo-shock forward of it, a sustained oscillatory behavior.

Therefore, if a flame propagation speed is calculated from the flame front information a mean flame velocity of 0.273±0.048 m/s is obtained. This mean flame speed is associated with the mean speed at which the pressure field above the cavity will fluctuate. If used to calculate a Strouhal number for these fluctuations,

$$(4.3) \qquad St = \frac{fL}{U} = \frac{4.88 \text{ Hz} \cdot 0.0127 \text{ m}}{0.273 \text{ m/s}} = 0.233 \pm 0.046,$$

where the frequency, f, and mean velocity, U, from the observed flame front observations has been used with cavity depth. This non-dimensional value corresponds to that of the shear-layer instability, but in this case it is being forced by the imposition of the flame front dictated pressure field velocity over the cavity.

It should be mentioned that there also exists the potential for a transition event to be triggered by the flame oscillations. As can be seen in Figure 4.13, the region in which the oscillatory instability was observed adjoins the scramjet mode operation region. If unstable ramjet mode operation were to be established just outside of the scram-mode regime

boundary, the device could transition into scramjet mode due to any small perturbations in flow blockage created as the flame position oscillates in the combustor. Operation in scramjet mode does not allow the self-sustaining oscillatory mechanism described to perpetuate. This would require the flow to transition back to ramjet mode, with the instability driving a continual cycle of combustion mode transition within the device.

4.5   Case E$_2$: Flame Penetration Angle

For cases where the flame is stabilized in the cavity shear-layer, the angle of flame penetration with respect to the cross-flow becomes a function of inlet stagnation temperature. Three different stagnation temperature conditions are provided in Table 2.9 with similar equivalence ratio. In Figure 4.17, three images are shown for the same fueling condition but different inlet cross-flow stagnation temperatures. The penetration angle of the flame is seen to increase with stagnation temperature.

Higher inlet stagnation temperatures create higher static temperatures in the combustion. An increase in static temperature in the combustor, in turn increases the flame speed. This allows a steeper penetration of the flame into the center of the combustor.

Flame penetration angle, with respect to the cross-flow direction, is shown as a function of inlet stagnation temperature in Figure 4.18. The data points in the figure were compiled by tracing contours of constant recorded image intensity along the flame front for a series of images at each stagnation temperature. The angle varies from approximately 15° at 1000 K to 21.5^o at 1400 K in a roughly linear manner.

This information is consistent with the earlier observation that the cavity stabilization mode becomes more preferred as the inlet stagnation temperature is lowered. In the instance of increased stagnation temperature, a flame is located further forward along the cavity and will have a greater potential to move from the stable cavity stabilization regime

(a) Case E_2^1, T_o = 1000 K

(b) Case E_2^2, T_o = 1200 K

(c) Case E_2^3, T_o = 1400 K
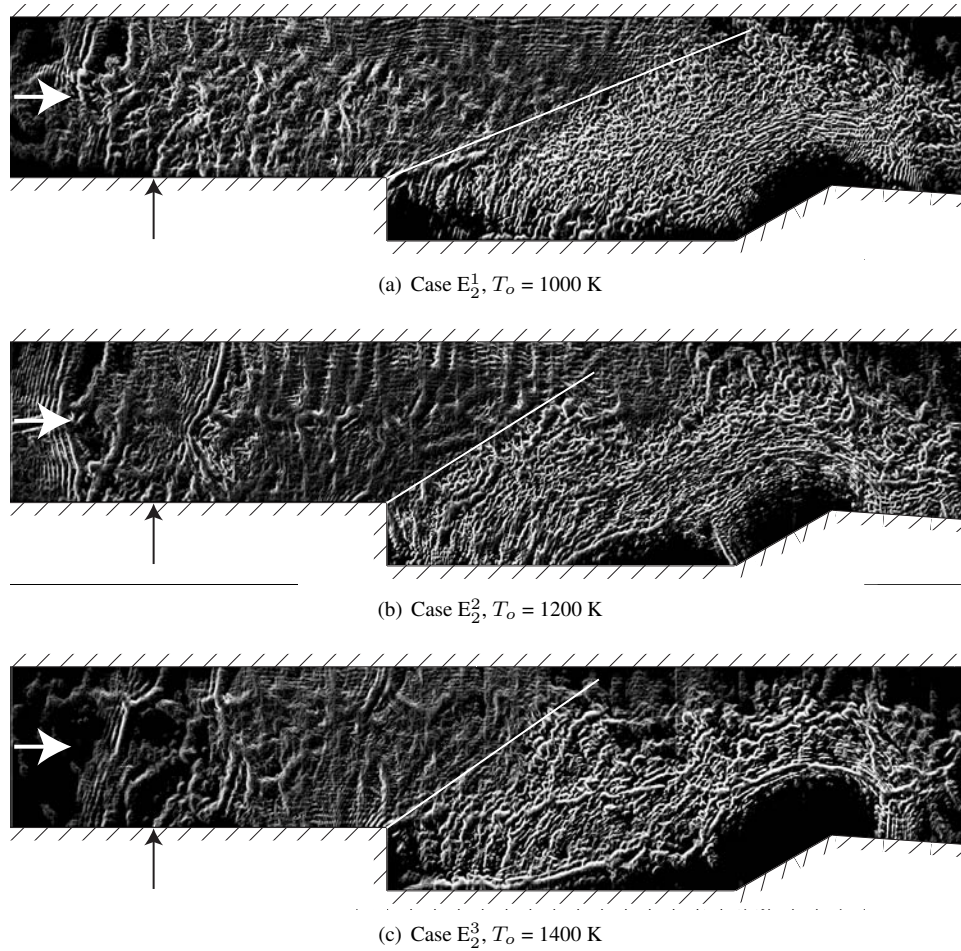
Figure 4.17: Shearing interferograms of the combustor for stagnation temperatures, T_o, of (a) 1000K, (b) 1200K and (c) 1400K.

to the unsteady, flame speed coupled oscillatory flame regime. As Heltsley et al. [19] observed, the increase in combustor static temperature due to the stagnation temperature increase assists in this progression to instability.

4.6 Conclusions for Combustion Mode Transition and Flame/Shock-train Interaction Study

The ram-scram transition boundary was measured and plotted on a regime diagram that represents the parameter space formed by the fuel equivalence ratio and inlet stagnation temperature. For the stagnation temperatures that were achieved in the range of 1000 to 1500 K, the transition equivalence ratio was found to vary from 0.17 to 0.22. These tran-
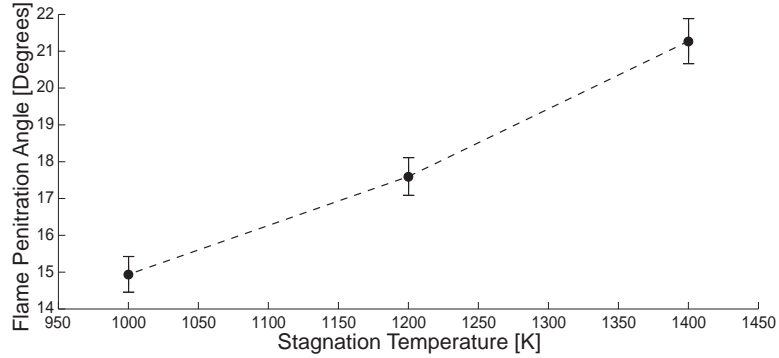
Figure 4.18: Penetration angle of main flame, measured flow parallel from the leading edge of the cavity, as a function for inlet stagnation temperature, T_o.

sition values also depend on the area ratio of the combustor geometry and the heat losses to the walls. The nature of the flame stabilization over this equivalence ratio/stagnation temperature parameter space has been studied as well. A model is required to extrapolate the present results in order to predict transition in other geometries.

For certain run conditions the flame leading edge underwent low frequency periodic oscillations. A mechanism has been identified for which flame speed excites the self-sustaining cavity shear-layer instability and drives the oscillatory behavior of the flame in the unstable regime. The front-to-rear oscillatory motion of the flame was observed to be coupled directly to the behavior of the upstream isolator pseudo-shock. The entire shock-train was measured to undergo oscillations at the same frequency as the flame, but were 88 degrees out of phase with the flame oscillations. The relevant time scales of the flame-shock interactions were discussed.

The discrete instance of combustion mode transition, from ram-to-scram and vice versa, was imaged at over 1 kHz frame rate. In both instances, shocks are seen to adjust as required by the blockage created in the combustor and the subsequent back pressure that it develops. At times the shock-trains present are seen to exist entirely within the confines of the combustor, stretching from the location of the fuel injector and across the cavity anchored position of the main flame.

A surprising result is that scram-to-ram transition was observed when the combustor sidewall temperature was allowed to rise sufficiently. The mechanism is believed to be that the reduction of heat loss to the hot walls causes more combustion heat release to be absorbed by the air flow, which increases the effective equivalence ratio and drives the flow to ram-mode.

Images of the shock structure during the ram-scram transition indicate that flow is highly two-dimensional; the isolator shock-train moves downstream and sits above the fuel-jet, leading to a mixed supersonic upper flow and a subsonic lower combustion region. Eventually the shock-train disappears, leaving only the bow shock attached to the fuel-jet when the scram-mode is achieved.

CHAPTER V

Summary & Conclusions

The University of Michigan Dual-mode Combustor experiment has been used to study the physical interplay between a combustion induced pseudo-shock created in a supersonic isolator and the dynamics present in the combustor region of such a device. Schlieren imaging has been used to assess the pseudo-shock structure, while a laser interferometry technique has been adapted to provide insight into the combustor, in particular the dynamics of the main fuel flame.

A hydrogen-air combustor has been studied for heated inlet flows up to 1400 K. It has been concluded that the flow blockage in the combustor is caused by both the combustion of the fuel and by the fuel-jet penetration into the isolator cross-flow itself. Fuel equivalence ratio and fuel-jet momentum ratio have been used to quantify these two coupled blockage sources, respectively. The fuel injector developed blockage, and its influence on the maximum pressure recovery, plays a role in dictating the operating regime of the shock-train. A new, more appropriate delineation of the operating regime of pre-combustion shock-trains was developed taking these observations into account. In support of this, a normal shock-train breakdown and transition to oblique shock-train mechanism has been experimentally observed using high-speed Schlieren imagery.

A methodology is designed to represent the intricate effects of isolator geometry, injec-

tor design and operating condition on the development of blockage in the combustor and its coupling to the pre-combustion pseudo-shock. This isolator/injector mapping predicts the operation of the system for a set of given operating conditions.

The ram-scram transition boundary was measured and plotted across the equivalence ratio/stagnation temperature parameter space of the study. The nature of the flame stabilization was observed through kilo-hertz imaging using a laser interferometry technique.

An unexpected result of this study was the observation of scram-to-ram transition caused through an increase in the wall temperature of the test-section. As the wall temperature rises, the heat transferred away from the flow in reduced thus creating an effective increase in equivalence ratio, forcing the flow to ram-mode.

A low frequency periodic oscillation of the flame leading edge was observed under particular conditions. The driving mechanism behind this behavior was identified as being a flame speed forced coupling to the self-sustaining cavity shear-layer instability. The motion of the flame was seen to be directly linked to the position of the upstream isolator pseudo-shock. The entire shock-train was measured to undergo oscillations at the same frequency, but were out of phase with the flame oscillations.

The behavior of a supersonic isolator coupled to a combustor is a complex and fully coupled system. Understanding the interactions between the flame, the geometry, and pressure field with its subsequently formed shocks is critical if high-speed air-breathing propulsion technology is to be tamed.

APPENDICES

APPENDIX A

Flow Simulation - Comparison between Two Commercial Computational Fluid Dynamics Codes

A.1 Simulation of the Dual-Mode Combustor

The ability to simulate the flows through a scramjet device is critical to reducing the time between design cycles. A decreased reliance on experimental observation, while never being wholly removed, is a key target in lowering development costs. This section presents a brief comparison between two commercially available computational fluid dynamics packages in an effort to evaluate their applicability to the scramjet problem. The goal was not to make a direct comparison to actual experimental conditions, as neither package was expected to fully simulate such a complex internal flow-path, but rather to provide a commentary on what aspects of each piece of software contributed to converging the solution to a more physically rooted solution. The general areas of the physical effects captured, the validity of the simulated flow, as well as the ease in convergence to a solution were used as guidelines for this comparison. The two software packages used were CFD++ version 8.1.1 [33] and Fluent version 12.0.16 [24].

The geometry that was simulated was that of the Michigan Dual-Mode Combustor(MDMC) experiment, shown in Figure A.1. The geometry used is that of the experiment prior to the alterations described in Section 2.1, with a right-angled rear-cavity wall.
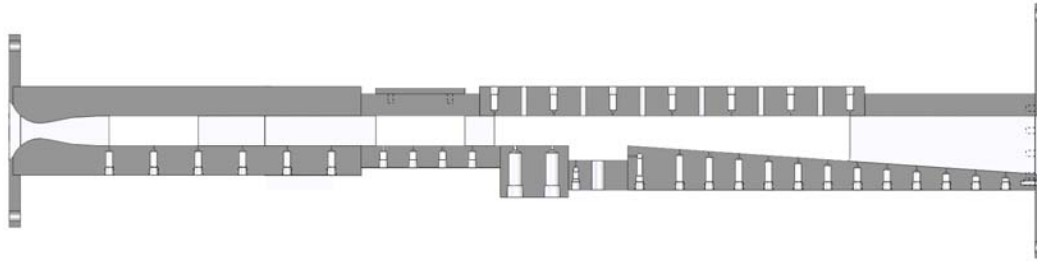
Figure A.1: Test-section Geometry

Figure A.2: Air Force Research Lab Computational Mesh

From this geometry two simulation meshes were created, one for each of the software packages as each had a slightly different set of requirements. The mesh used for the CFD++ simulation was created by Dr. C.-J. John Tam, AFRL/RZAS/Taitech Inc., and is shown in Figure A.2. The mesh consists of 384,000 hexahedral cells, following the geometry from upstream of the facility nozzle to the exit of the diverging combustor section. The mesh is fairly regular in design with appropriate groupings around the fuel injector and the cavity shear-layer locations.

The Fluent simulation was conducted on a mesh of 366,314 tetrahedral cells, with dense groupings along the lower combustor wall, and around the front and rear corners of the cavity. The mesh is shown in Figure A.3. Initial attempts were made to use the Air Force mesh with both pieces of software, however Fluent had problems with converging to a solution using this full, inlet-to-exhaust, model. To work around this mesh-density related issue, the truncated mesh containing what would be the subsonic portion of the combustor under ramjet operating conditions was created. The matching of boundary conditions between these two simulations became more complicated, and is described in Section A.2.1.
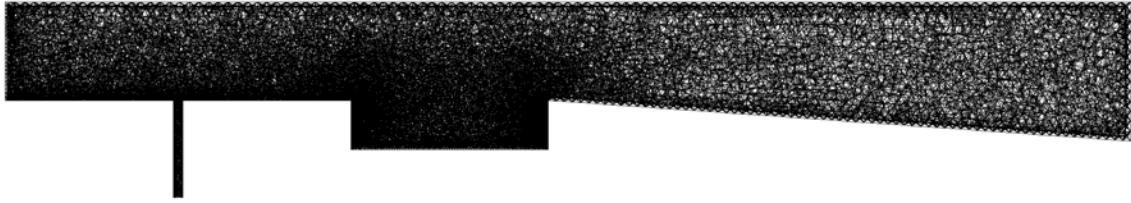
Figure A.3: Truncated Combustor Computational Mesh

A.2 Steady Simulations

Steady simulations were created with the software packages for a single set of operating conditions. For the CFD++ simulation, the Compressible Real Gas Navier-Stokes/Euler equations were solved with a cubic k-ϵ turbulence model. Thirteen chemical species were included in the simulation. See Section A.2.2 for a more detailed description of the reaction mechanisms used. The Fluent simulation solved the Compressible Navier-Stokes equations with the inclusion of nine chemical species. A realizable k-ϵ turbulence model with standard wall functions models the turbulence. Both solutions were converged to normalized residuals of 10^{-4} or better.

A.2.1 Boundary Conditions

The boundary conditions for the simulation were defined to mimic the conditions present in the MDMC experiment, including the vitiated air effects from the water vapor contamination. The inlet condition for the CFD++ simulation was set to behave as a reservoir of stagnation conditions, with a particular chemical composition and turbulence properties. These conditions are listed in Table A.1 and are consistent with conditions observed during an experiment with a stagnation pressure of 339 kPa (49 psia) and stagnation temperature of 1370 K.

To compensate for the inability of the Fluent code to use the Air Force generated mesh, the truncated combustor mesh was used. To ensure an "apples-to-apples" comparison the

101

Table A.1: Combustor inlet air boundary conditions

Quantity	Boundary Value	Units
$P_{o,3}$	$339,000$	Pa
$T_{o,3}$	1370	K
k_3	6	m^2/s^2
ϵ_3	9003.4	m^2/s^3
$Y_{H_2,3}$	$8.2 \cdot 10^{-8}$	
$Y_{H,3}$	0.0	
$Y_{O_2,3}$	0.21	
$Y_{O,3}$	$1.8 \cdot 10^{-7}$	
$Y_{H_2O,3}$	0.21	
$Y_{H_2O_2,3}$	$2.5 \cdot 10^{-8}$	
$Y_{HO_2,3}$	$2.0 \cdot 10^{-7}$	
$Y_{HNO,3}$	0.0	
$Y_{OH,3}$	$3.4 \cdot 10^{-5}$	
$Y_{N,3}$	0.0	
$Y_{NO,3}$	0.0	
$Y_{NO_2,3}$	0.0	
$Y_{N_2,3}$	0.58	

Table A.2: Additional truncated combustor inlet air boundary conditions

Quantity	Boundary Value	Units
M_3	0.63	
ρ_3	0.657	kg/m^3
U_3	456	m/s

inlet conditions for the truncated mesh were taken from the converged CFD++ solution at the appropriate combustor location. The Fluent software required the additional conditions listed in Table A.2.

The fuel injection conditions for both simulations were the same. Gaseous hydrogen fuel was injected at the choked sonic condition into the combustor. The required boundary conditions are listed in Table A.3, and represent a room temperature fuel injected under 814 kPa (118 psia) of stagnation pressure.

A.2.2 Chemistry

One of the major differences between the two simulation was the manner in which the chemical kinetics were handled by each code. At the basis of both codes was the inclusion of finite-rate chemistry, however the difference was in the particulars of the implementation.

A.2.2.1 Finite-rate Chemistry - CFD++

The CFD++ software models the chemical interaction in a strict finite-rate manner through the Arrhenius equation,

$$k = AT^n e^{(-E/RT)},$$ (A.1)

where k is the reaction rate, A is the frequency factor, T the static temperature, n the temperature exponent, E the activation energy and R the gas constant. This means that

Table A.3: Hydrogen fuel injector boundary conditions

Quantity	Boundary Value	Units
$P_o f$	$814,000$	Pa
$T_o f$	300	K
k_f	600	m^2/s^2
ϵ_f	$1.47 \cdot 10^7$	m^2/s^3
$Y_{H_2,f}$	1.0	
$Y_{H,f}$	0.0	
$Y_{O_2,f}$	0.0	
$Y_{O,f}$	0.0	
$Y_{H_2O,f}$	0.0	
$Y_{H_2O_2,f}$	0.0	
$Y_{HO_2,f}$	0.0	
$Y_{HNO,f}$	0.0	
$Y_{OH,f}$	0.0	
$Y_{N,f}$	0.0	
$Y_{NO,f}$	0.0	
$Y_{NO_2,f}$	0.0	
$Y_{N_2,f}$	0.0	
M_f	1.0	
ρ_f	0.653	kg/m^3
U_f	1207	m/s

the only mechanism impacting the progress of a reaction are the densities of the constituent chemical compounds and the physical conditions present at a particular location. For the CFD++ simulation the hydrogen-air reaction mechanism developed for scramjet applications by Jachimawski [25] was used. The various rate constants for the reaction mechanism are given in Table A.4.

This method of including chemical reactions into a computational code is fairly straightforward. The amount of modeling hidden below the surface of the code, e.g. cellular mixing efficiencies, is minimized. While the implementation is not as sophisticated as it could be, it does lend itself to providing a measure of stability to the solver as it attempts to iterate to a solution.

A.2.2.2 Flamelet Chemistry - Fluent

The Fluent software simulated the combustion process using a flamelet modeling approach. Unlike the CFD++ simulation, the reaction mechanism used as a basis for the flamelet tables is the standard 18 reaction mechanism. Table A.5 gives the Arrhenius coefficients for this set of reactions.

For an equilibrium, adiabatic, single-mixture fraction case, the mean temperature, density and species fractions are a function of the mixture fraction, $\bar{f}$, and its variance, $\bar{f'^2}$, only. These integrals are computed and stored in look-up tables for use during the simulation process.

The mixture fraction, f, takes the form

(A.2) $$f = \frac{Z_1 - Z_{i,ox}}{Z_{i,fuel} - Z_{i,ox}}$$

where Z_i is the elemental mass fraction for element, i. The subscript ox denotes the value at the oxidixer stream inlet and the subscript $fuel$ denotes the values at the fuel stream inlet. The sum of these two mixture fractions is unity, $f_{fuel} + f_{ox} = 1$.

Table A.4: Jachimawski Reaction Mechanism for Hydrogen-Air Combustion [25]

	Reaction[†]	A	n	E
1	$H_2 + O_2 \rightarrow OH + OH$	$1.7 \cdot 10^{10}$	0	$2.008 \cdot 10^{10}$
2	$H + O_2 \rightarrow OH + O$	$2.6 \cdot 10^{11}$	0	$7.029 \cdot 10^{7}$
3	$O + H_2 \rightarrow OH + H$	$1.8 \cdot 10^{7}$	1	$3.724 \cdot 10^{7}$
4	$OH + H_2 \rightarrow H_2O + H$	$2.2 \cdot 10^{10}$	0	$2.155 \cdot 10^{7}$
5	$OH + OH \rightarrow H_2O + O$	$6.3 \cdot 10^{9}$	0	$4.561 \cdot 10^{6}$
6	$H + OH + M \rightarrow H_2O + M$	$2.2 \cdot 10^{16}$	-2	0.0
7	$H + H + M \rightarrow H_2 + M$	$6.4 \cdot 10^{11}$	-1	0.0
8	$H + O + M \rightarrow OH + M$	$6.0 \cdot 10^{10}$	-0.6	0.0
9	$H + O_2 + M \rightarrow HO_2 + M$	$2.1 \cdot 10^{9}$	0	$-4.184 \cdot 10^{6}$
10	$HO_2 + H \rightarrow H_2 + O_2$	$1.3 \cdot 10^{10}$	0	0.0
11	$HO_2 + H \rightarrow OH + OH$	$1.4 \cdot 10^{11}$	0	$4.519 \cdot 10^{6}$
12	$HO_2 + H \rightarrow H_2O + O$	$1.0 \cdot 10^{10}$	0	$4.519 \cdot 10^{6}$
13	$HO_2 + O \rightarrow O_2 + OH$	$1.5 \cdot 10^{10}$	0	$3.975 \cdot 10^{6}$
14	$HO_2 + OH \rightarrow H_2O + O_2$	$8.0 \cdot 10^{9}$	0	0.0
15	$HO_2 + HO_2 \rightarrow H_2O_2 + O_2$	$2.0 \cdot 10^{9}$	0	0.0
16	$H + H_2O_2 \rightarrow H_2 + HO_2$	$1.4 \cdot 10^{9}$	0	$1.506 \cdot 10^{7}$
17	$O + H_2O_2 \rightarrow OH + HO_2$	$1.4 \cdot 10^{10}$	0	$2.678 \cdot 10^{7}$
18	$OH + H_2O_2 \rightarrow H_2O + HO_2$	$6.1 \cdot 10^{9}$	0	$5.983 \cdot 10^{6}$
19	$M + H_2O_2 \rightarrow OH + OH + M$	$1.2 \cdot 10^{14}$	0	$1.904 \cdot 10^{8}$
20	$O + O + M \rightarrow O_2 + M$	$6.0 \cdot 10^{11}$	0	$-7.531 \cdot 10^{6}$
21	$N + N + M \rightarrow N_2 + M$	$2.8 \cdot 10^{11}$	-0.75	0.0
22	$N + O_2 \rightarrow NO + O$	$6.4 \cdot 10^{6}$	1	$2.636 \cdot 10^{7}$
23	$O + NO \rightarrow N_2 + O$	$1.6 \cdot 10^{10}$	0	0.0
24	$N + OH \rightarrow NO + H$	$6.3 \cdot 10^{8}$	0.5	0.0
25	$H + NO + M \rightarrow HNO + M$	$5.4 \cdot 10^{9}$	0	$-2.510 \cdot 10^{6}$
26	$H + HNO \rightarrow NO + H_2$	$4.8 \cdot 10^{9}$	0	0.0
27	$O + HNO \rightarrow NO + OH$	$5.0 \cdot 10^{8}$	0.5	0.0
28	$OH + NO \rightarrow NO + H_2O$	$3.6 \cdot 10^{10}$	0	0.0
29	$HO_2 + HNO \rightarrow NO + H_2O_2$	$2.0 \cdot 10^{9}$	0	0.0
30	$HO_2 + NO \rightarrow NO_2 + OH$	$3.4 \cdot 10^{9}$	0	$-1.088 \cdot 10^{6}$
31	$H + NO_2 \rightarrow NO + OH$	$3.5 \cdot 10^{11}$	0	$6.276 \cdot 10^{6}$
32	$O + NO_2 \rightarrow NO + O_2$	$1.0 \cdot 10^{10}$	0	$2.510 \cdot 10^{6}$
33	$M + NO_2 \rightarrow NO + O + M$	$1.16 \cdot 10^{13}$	0	$2.761 \cdot 10^{8}$

Rate Coefficient are given in the form: $k = AT^n e^{(-E/RT)}$.

Units are in seconds, kilomoles, cubic meters, Joules, and Kelvins.

[†]The third-body efficiencies relative to $N_2 = 1.0$ are as follows: for reaction (6), $H_2O = 6.0$; for reaction (7), $H_2 = 2.0$ and $H_2O = 6.0$; for reaction (8), $H_2O = 6.0$; for reaction (9), $H_2 = 2.0$ and $H_2O = 16.0$; for reaction (19), $H_2O = 15.0$.

Table A.5: Standard 18 Reaction Mechanism for Hydrogen-Air Combustion

	Reaction	A	n	E
1	$H_2 + O_2 \leftrightarrow OH + OH$	$1.7 \cdot 10^{10}$	0	$2.016 \cdot 10^{10}$
2	$H + O_2 \leftrightarrow OH + O$	$1.42 \cdot 10^{11}$	0	$6.866 \cdot 10^{7}$
3	$O + H_2 \leftrightarrow OH + H$	$2.07 \cdot 10^{11}$	0	$5.757 \cdot 10^{7}$
4	$OH + H_2 \leftrightarrow H_2O + H$	$3.16 \cdot 10^{4}$	1.8	$1.289 \cdot 10^{7}$
5	$OH + OH \leftrightarrow H_2O + O$	$5.50 \cdot 10^{10}$	0	$2.931 \cdot 10^{7}$
6	$H + OH + M \leftrightarrow H_2O + M$	$2.2 \cdot 10^{16}$	-2	0.0
7	$H + H + M \leftrightarrow H_2 + M$	$6.53 \cdot 10^{11}$	-1	0.0
8	$H + O_2 + M \leftrightarrow HO_2 + M$	$3.20 \cdot 10^{12}$	-1	0.0
9	$HO_2 + H \leftrightarrow H_2 + O_2$	$2.53 \cdot 10^{10}$	0	$2.931 \cdot 10^{6}$
10	$HO_2 + H \leftrightarrow OH + OH$	$1.99 \cdot 10^{11}$	0	$7.536 \cdot 10^{6}$
11	$HO_2 + H_2 \leftrightarrow H_2O_2 + H$	$3.01 \cdot 10^{8}$	0	$7.829 \cdot 10^{7}$
12	$HO_2 + O \leftrightarrow O_2 + OH$	$5.0 \cdot 10^{10}$	0	$4.186 \cdot 10^{6}$
13	$HO_2 + OH \leftrightarrow H_2O + O_2$	$5.0 \cdot 10^{10}$	0	$4.186 \cdot 10^{6}$
14	$HO_2 + HO_2 \leftrightarrow H_2O_2 + O_2$	$1.99 \cdot 10^{9}$	0	0.0
15	$H + H_2O_2 \leftrightarrow H_2O + OH$	$5.0 \cdot 10^{11}$	0	$4.186 \cdot 10^{7}$
16	$O + H_2O_2 \leftrightarrow OH + HO_2$	$1.99 \cdot 10^{10}$	0	$2.47 \cdot 10^{7}$
17	$OH + H_2O_2 \leftrightarrow H_2O + HO_2$	$1.02 \cdot 10^{10}$	0	$7.954 \cdot 10^{6}$
18	$M + H_2O_2 \leftrightarrow OH + OH + M$	$1.21 \cdot 10^{14}$	0	$1.905 \cdot 10^{8}$

Rate Coefficient are given in the form: $k = AT^n e^{(-E/RT)}$.
Units are in seconds, kilomoles, cubic meters, Joules, and Kelvins.

Fluent simulates the evolution of the mixture fraction via two equations. The first is the Favre mean mixture fraction equation

$$(A.3) \qquad \frac{\partial}{\partial t}\left(\rho \bar{f}\right) + \nabla \cdot \left(\rho \vec{v} \bar{f}\right) = \nabla \cdot \left(\frac{\mu_t}{\sigma_t}\nabla \bar{f}\right) + S_m + S_{user}.$$

The source term S_m is due solely to transfer of mass into gas phase from liquid fuel droplets or reacting particles (e.g. coal). S_{user} is any user-defined source term. Fluent also solves a conservation equation for the mixture fraction variance,

$$(A.4) \qquad \frac{\partial}{\partial t}\left(\rho \bar{f'^2}\right) + \nabla \cdot \left(\rho \vec{v} \bar{f'^2}\right) = \nabla \cdot \left(\frac{\mu_t}{\sigma_t}\nabla \bar{f'^2}\right) + C_g \mu_t \left(\nabla \bar{f}\right)^2 - C_d \rho \frac{\epsilon}{k}\bar{f'^2} + S_{user}$$

where $f' = f - \bar{f}$. The default values for the constants σ_t, C_g and C_d are 0.85, 2.86 and 2.0, respectively, and S_{user} is again any user-defined source term.

The turbulence-chemistry interaction is modeled using an assumed-shape probability density function (PDF) approach. The relationship between the mixture fraction, f, and the shape of the PDF, $p(f)$, can be written as

$$(A.5) \qquad p(f)\Delta f = \lim_{T \to \infty} \frac{1}{T}\sum_i \tau_i$$

where T is the time scale and τ_i is the amount of time the mixture fraction, f, spends in the Δf band of values. The assumed-shape of the PDF was a β-Function, defined as

$$(A.6) \qquad p(f) = \frac{f^{\alpha-1}\left(1-f\right)^{\beta-1}}{\int f^{\alpha-1}\left(1-f\right)^{\beta-1} df}$$

where

$$(A.7) \qquad \alpha = \bar{f}\left[\frac{\bar{f}\left(1-\bar{f}\right)}{\bar{f'^2}} - 1\right]$$

and

$$(A.8) \qquad \beta = \left(1-\bar{f}\right)\left[\frac{\bar{f}\left(1-\bar{f}\right)}{\bar{f'^2}} - 1\right].$$

Since the shape of the PDF is a function of only two moments of f the model can be closed and the species composition, density and temperature determined from the look-up tables to be fed back into the flow simulation.

A.2.3 Plume Structure

The first comparison that can be made between the CFD++ and Fluent simulations is that of the structure of the fuel plume. The results of the CFD++ simulation is shown as contour plots in Figure A.4 through A.11, while the Fluent results are given in Figures A.12 through A.19. In some cases, care should be taken to note the contour level scalings when making comparisons of a particular quantity between the two simulations.

A qualitative examination of the axial flow velocities predicted by the two codes, provided in Figures A.4 and A.12, shows that there is consistency in the global structure of the fuel plume. The predicted jet penetration distance is similar as well as the maximum axial speeds. One difference between the simulations is that Fluent predicts a considerably stronger recirculation in the wake of the fuel-jet, an almost three times stronger reversed flow speed than that predicted by CFD++. Given that the Fluent inlet boundary conditions have been matched to the conditions provided by the CFD++ simulation, the difference must come from the modeling approach used by the respective codes. In the case of the weaker recirculation zone, the different methods used to handle flow compressibility can be seen. The CFD++ simulation shows a larger compressible interaction between the fuel-jet and the inlet flow upstream of the injector. This can be seen in both the axial velocity, Figure A.4 and A.12, and the static pressure, Figure A.6 and A.14, results where the fuel-jet has caused a larger decrease in flow velocity and a proportional increase in static pressure to compensate.

Besides this apparent difference in the modeling of compressible flow effects, both simulations predict that the flow will choke at the same axial location, just after the entrance to the diverging section, within the combustor.

The CFD++ simulation predicts higher static temperatures, by nearly 400 K, than the Fluent results in the combusting fuel plume. This difference between the simulations

can be attributed to the implementation of the chemistry in each code. Without the rate-moderating effects caused by the flamelet modeling, the apparent reaction rates in the CFD++ case are higher than those shown by Fluent. This in turn drives the heat-release rate higher and is most readily seen in the local static temperature.

Interestingly, the CFD++ simulation predicts that the fuel will persist further into the combustor than in the Fluent case. This can be seen in Figures A.10 and A.18. The Fluent simulation predicts a faster breakdown of the H_2 fuel into intermediate species, but that these intermediates persist longer. Figure A.19 shows that the profile of oxidizer mass-fraction predicted by Fluent is consistent with that predicted by CFD++ in Figure A.11.
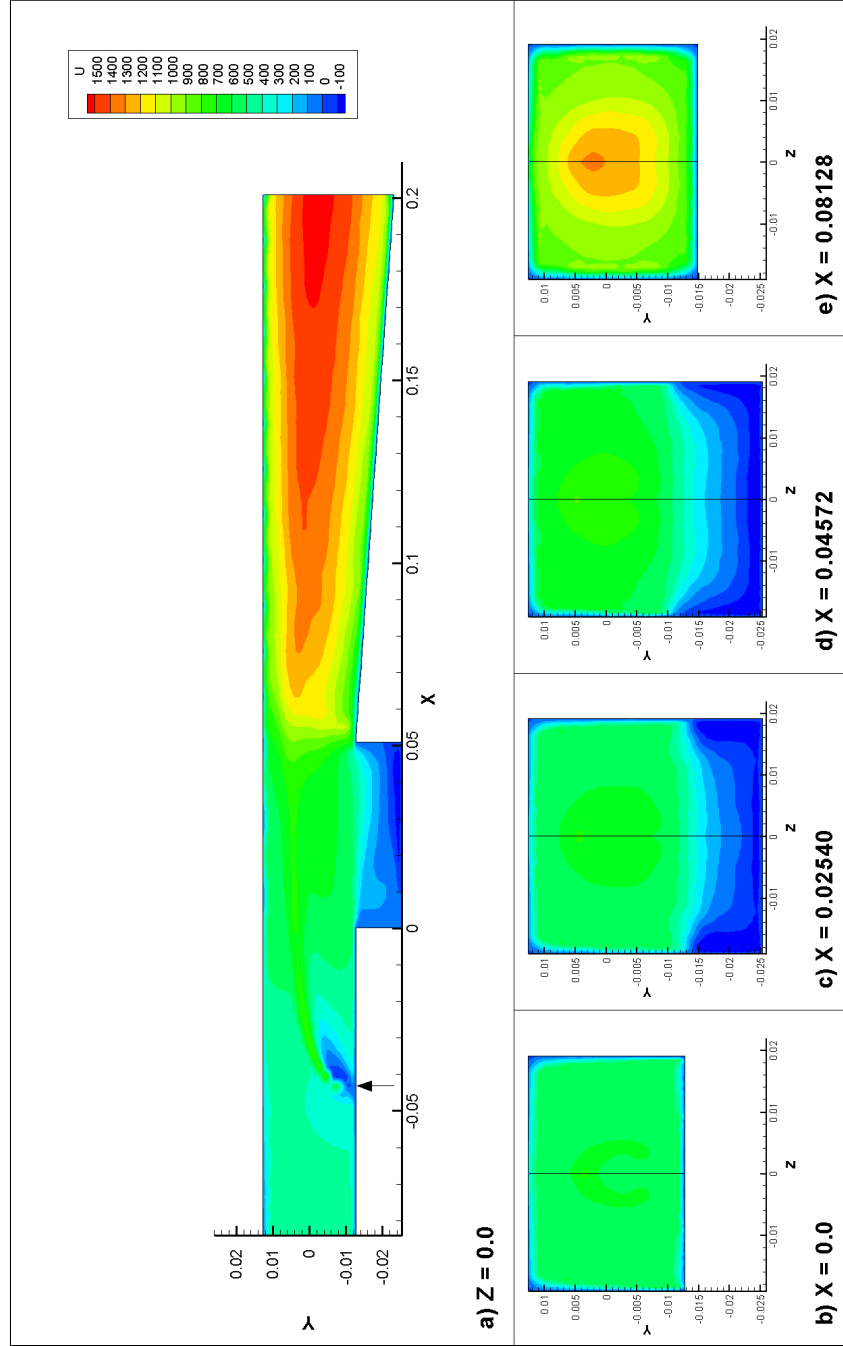
Figure A.4: Contours of axial velocity in meters per second from CFD++ on the (a) combustor symmetry plane and Z-Y planes at (b) $x = 0.0$ m, (c) $x = 0.02540$ m, (d) $x = 0.04572$ m and (e) $x = 0.08128$ m.
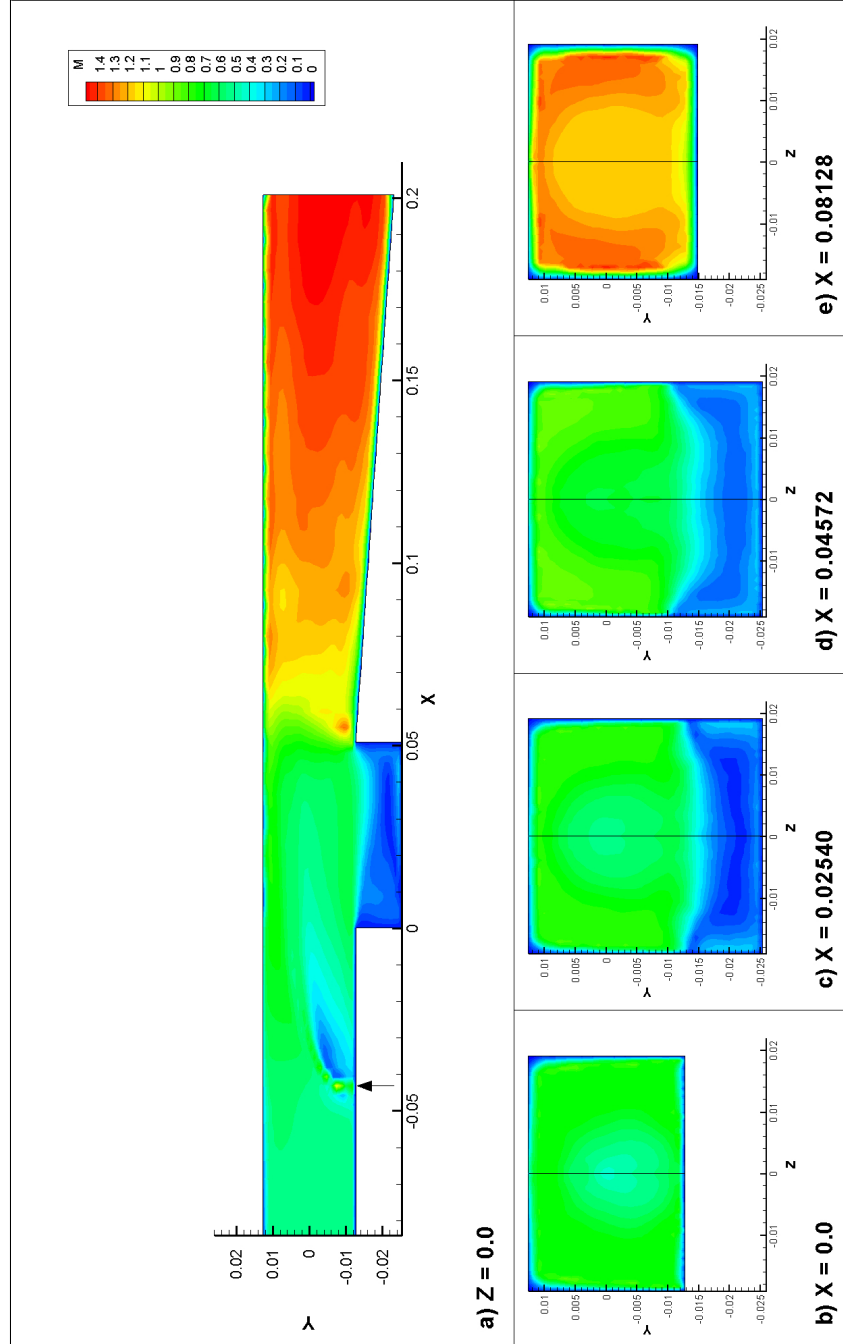
Figure A.5: Contours of Mach number from CFD++ on the (a) combustor symmetry plane and Z-Y planes at (b) $x = 0.0$ m, (c) $x = 0.02540$ m, (d) $x = 0.04572$ m and (e) $x = 0.08128$ m.
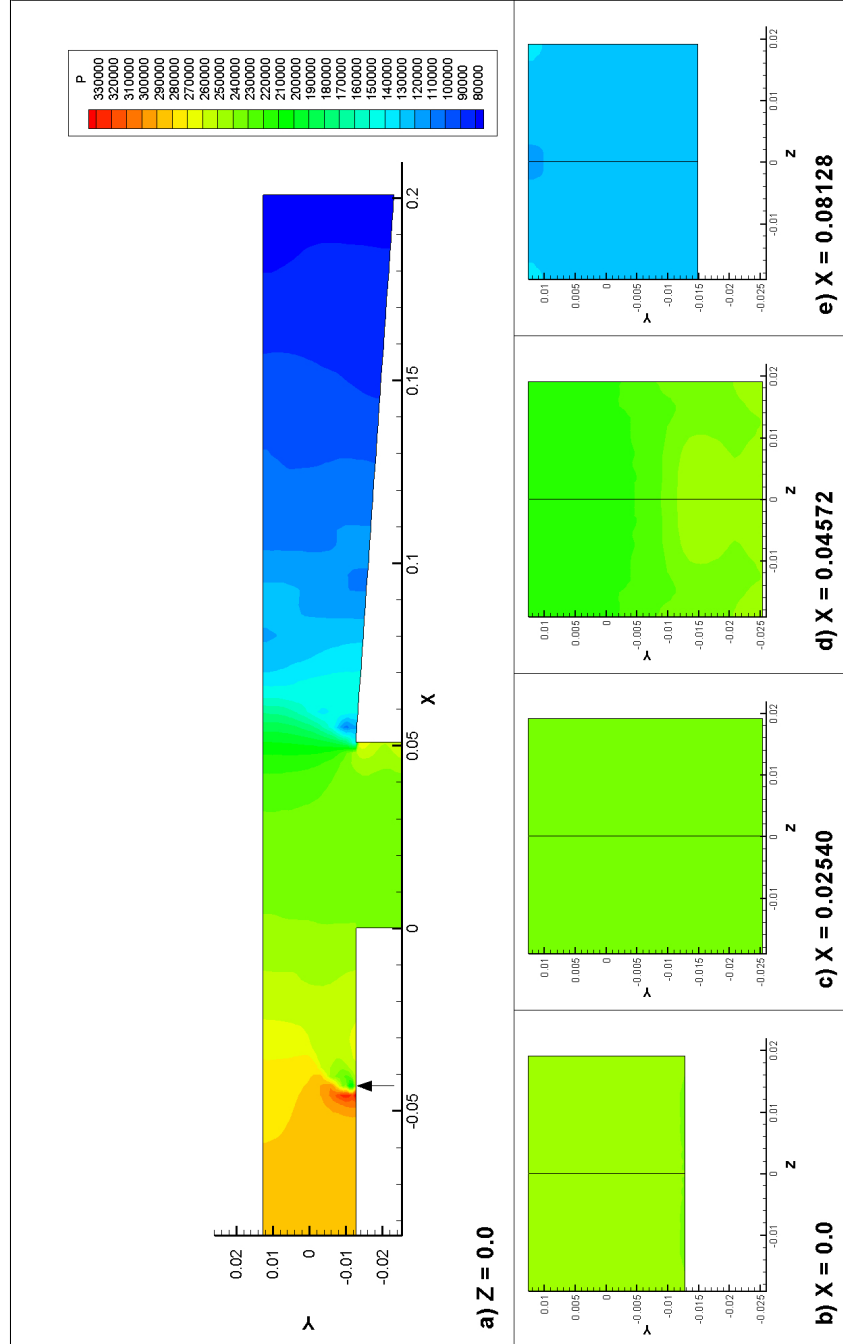
Figure A.6: Contours of static pressure in Pascals from CFD++ on the (a) combustor symmetry plane and Z-Y planes at (b) $x = 0.0$ m, (c) $x = 0.02540$ m, (d) $x = 0.04572$ m and (e) $x = 0.08128$ m.
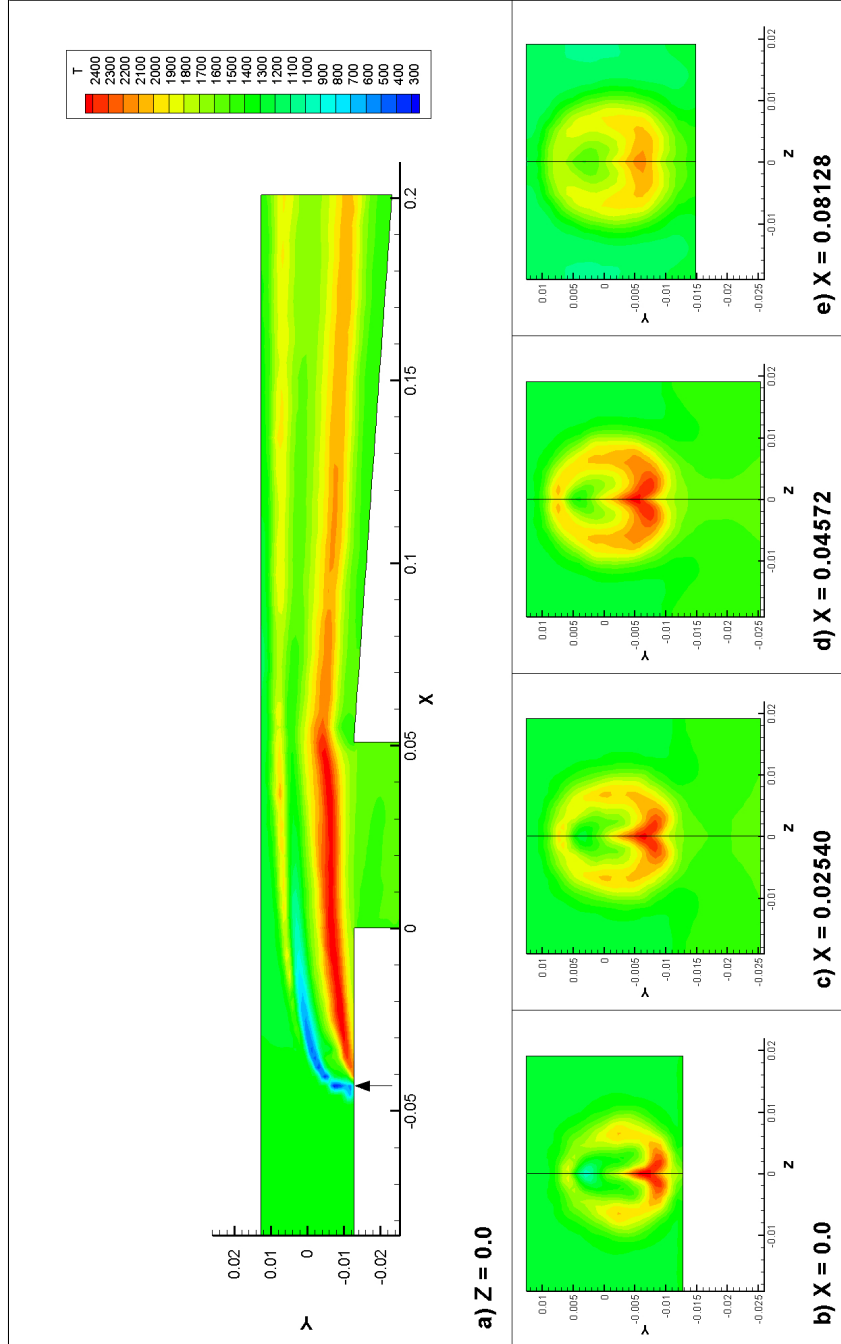
Figure A.7: Contours of static temperature in Kelvin from CFD++ on the (a) combustor symmetry plane and Z-Y planes at (b) $x = 0.0$ m, (c) $x = 0.02540$ m, (d) $x = 0.04572$ m and (e) $x = 0.08128$ m.
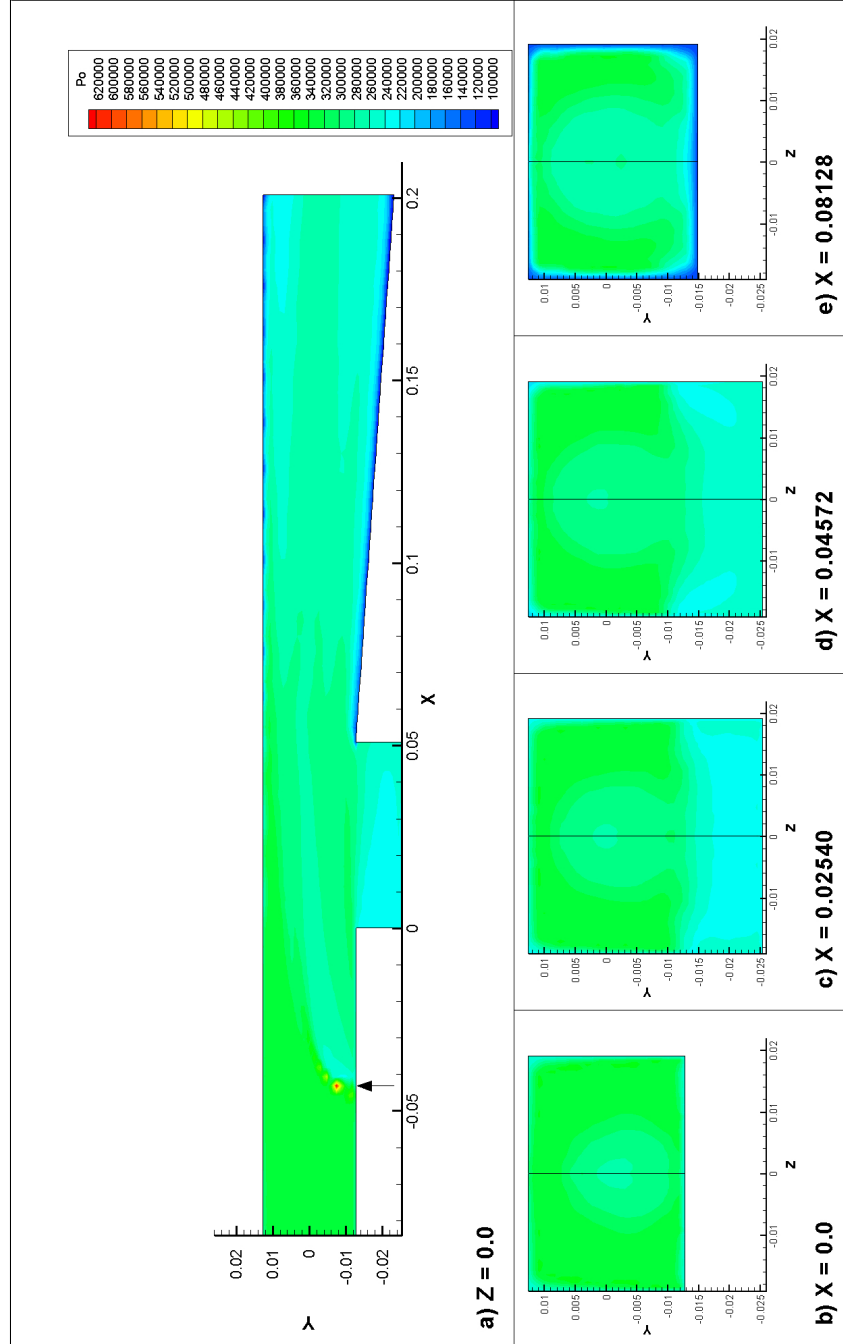
Figure A.8: Contours of stagnation pressure in Pascals from CFD++ on the (a) combustor symmetry plane and Z-Y planes at (b) $x = 0.0$ m, (c) $x = 0.02540$ m, (d) $x = 0.04572$ m and (e) $x = 0.08128$ m.
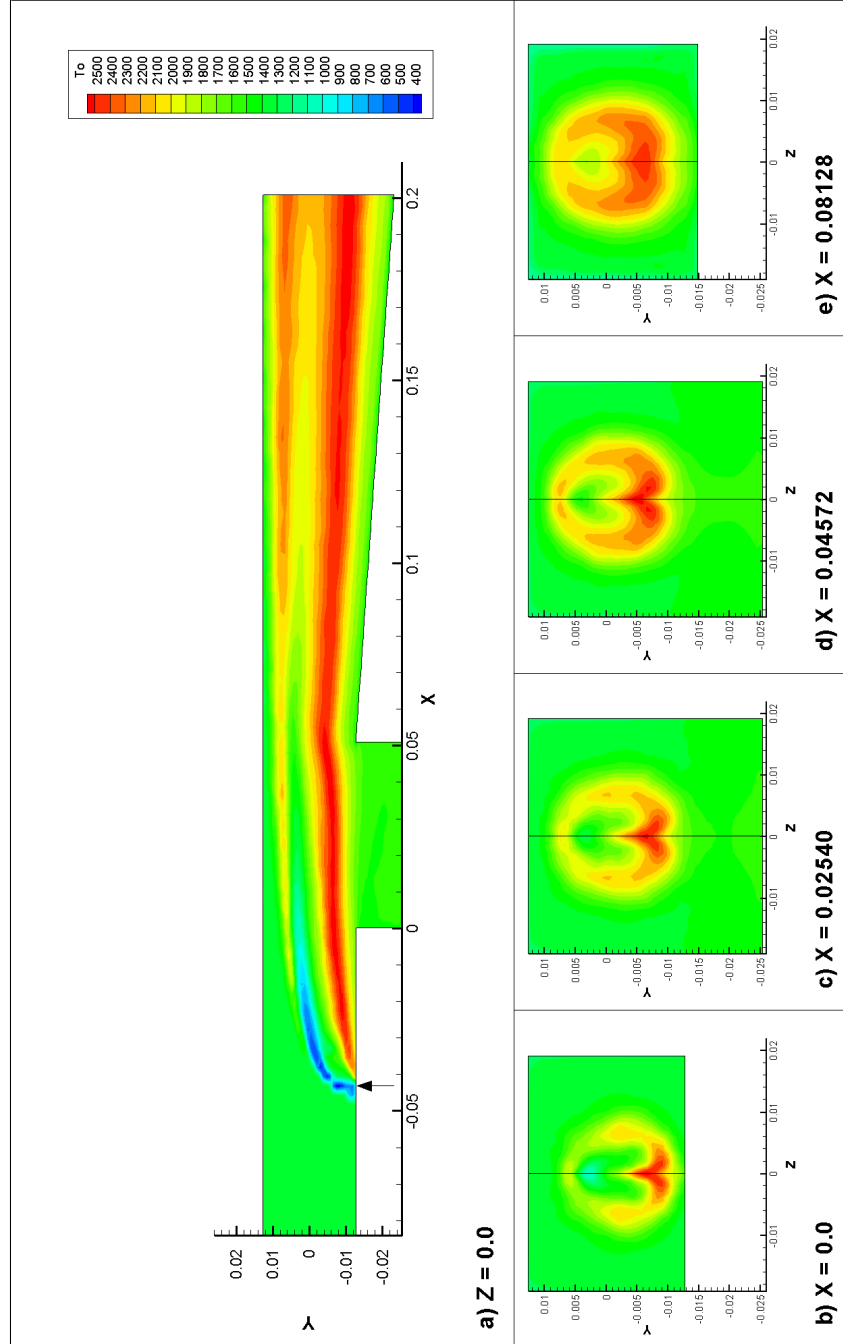
Figure A.9: Contours of stagnation temperature in Kelvin from CFD++ on the (a) combustor symmetry plane and Z-Y planes at (b) $x = 0.0$ m, (c) $x = 0.02540$ m, (d) $x = 0.04572$ m and (e) $x = 0.08128$ m.
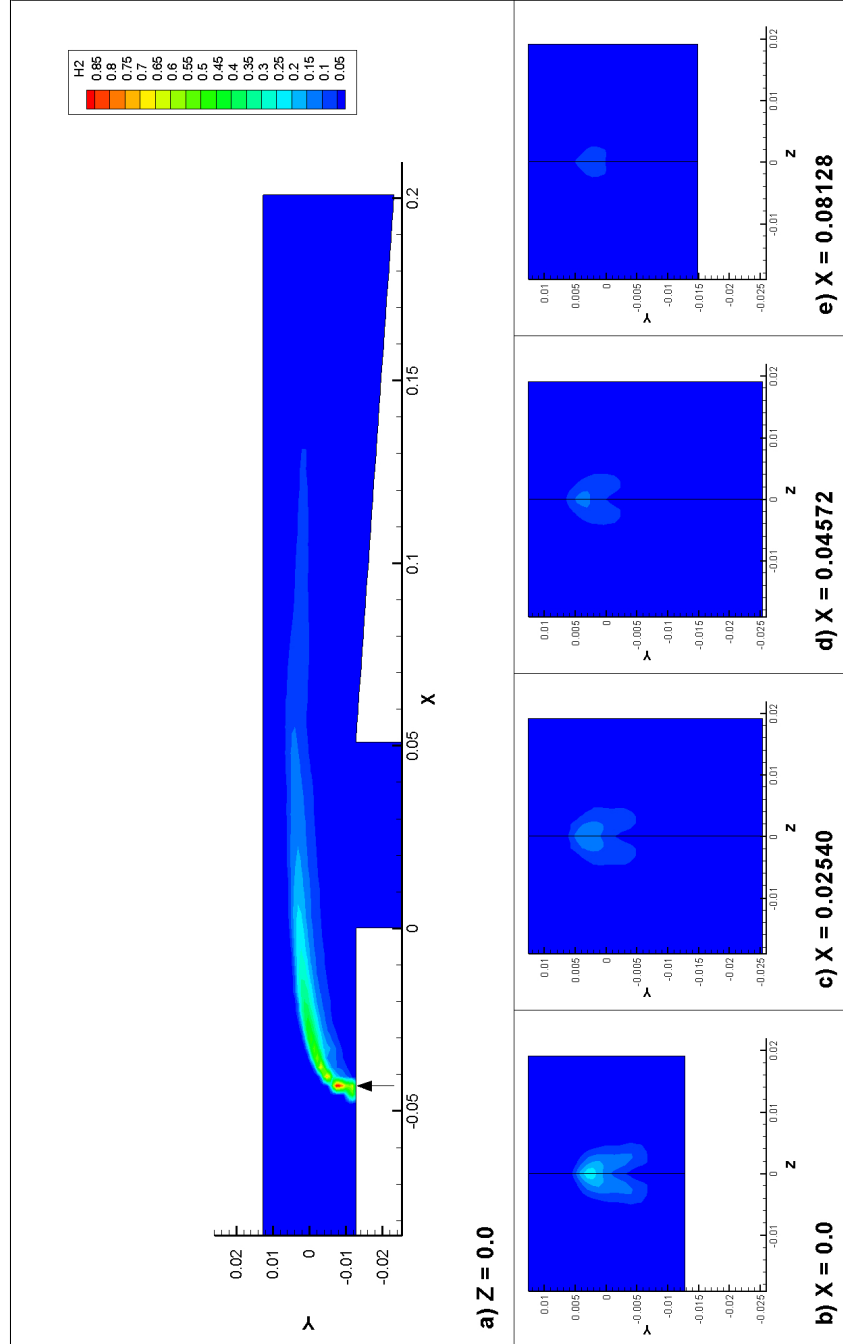
Figure A.10: Contours of fuel mass-fraction from CFD++ on the (a) combustor symmetry plane and Z-Y planes at (b) $x = 0.0$ m, (c) $x = 0.02540$ m, (d) $x = 0.04572$ m and (e) $x = 0.08128$ m.
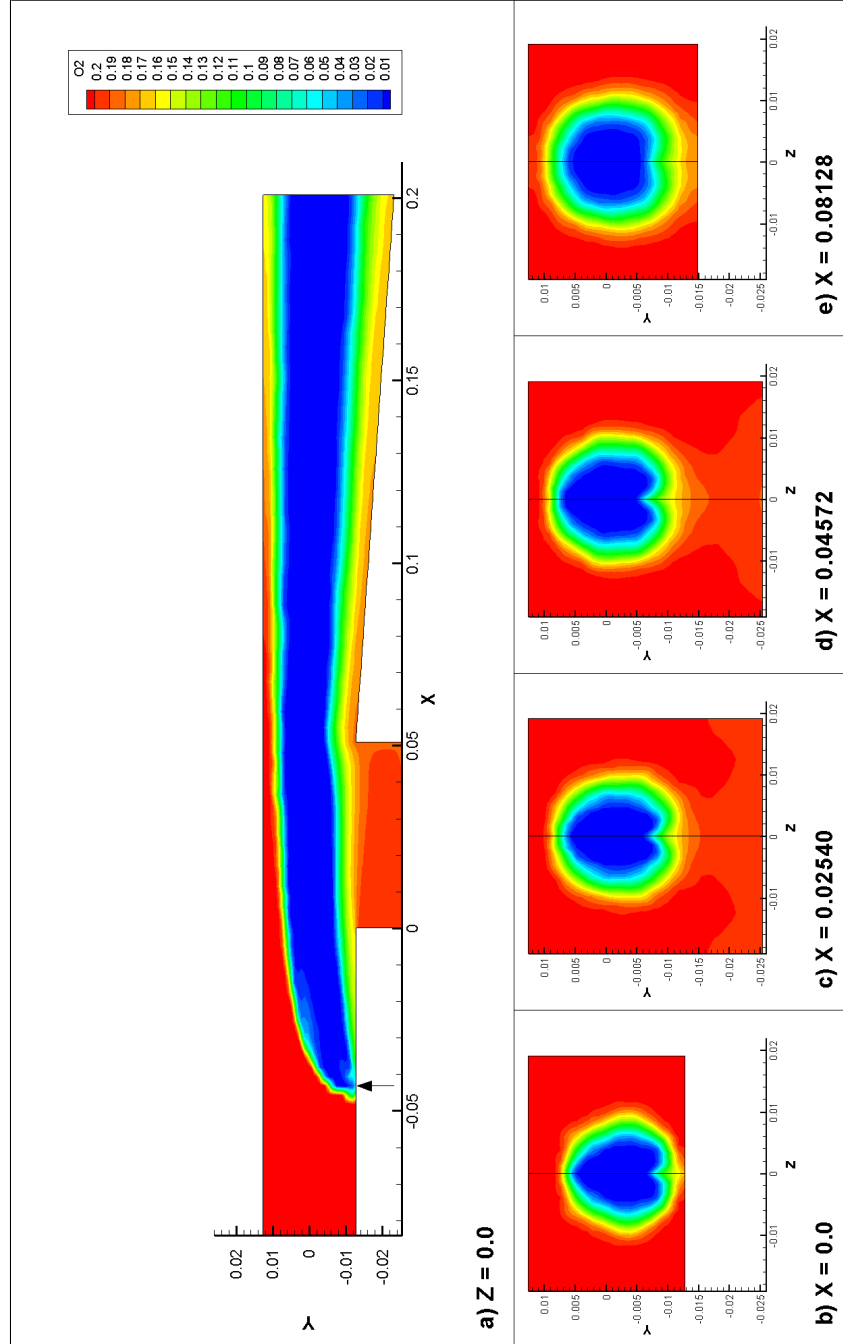
Figure A.11: Contours of oxidizer mass-fraction from CFD++ on the (a) combustor symmetry plane and Z-Y planes at (b) $x = 0.0$ m, (c) $x = 0.02540$ m, (d) $x = 0.04572$ m and (e) $x = 0.08128$ m.
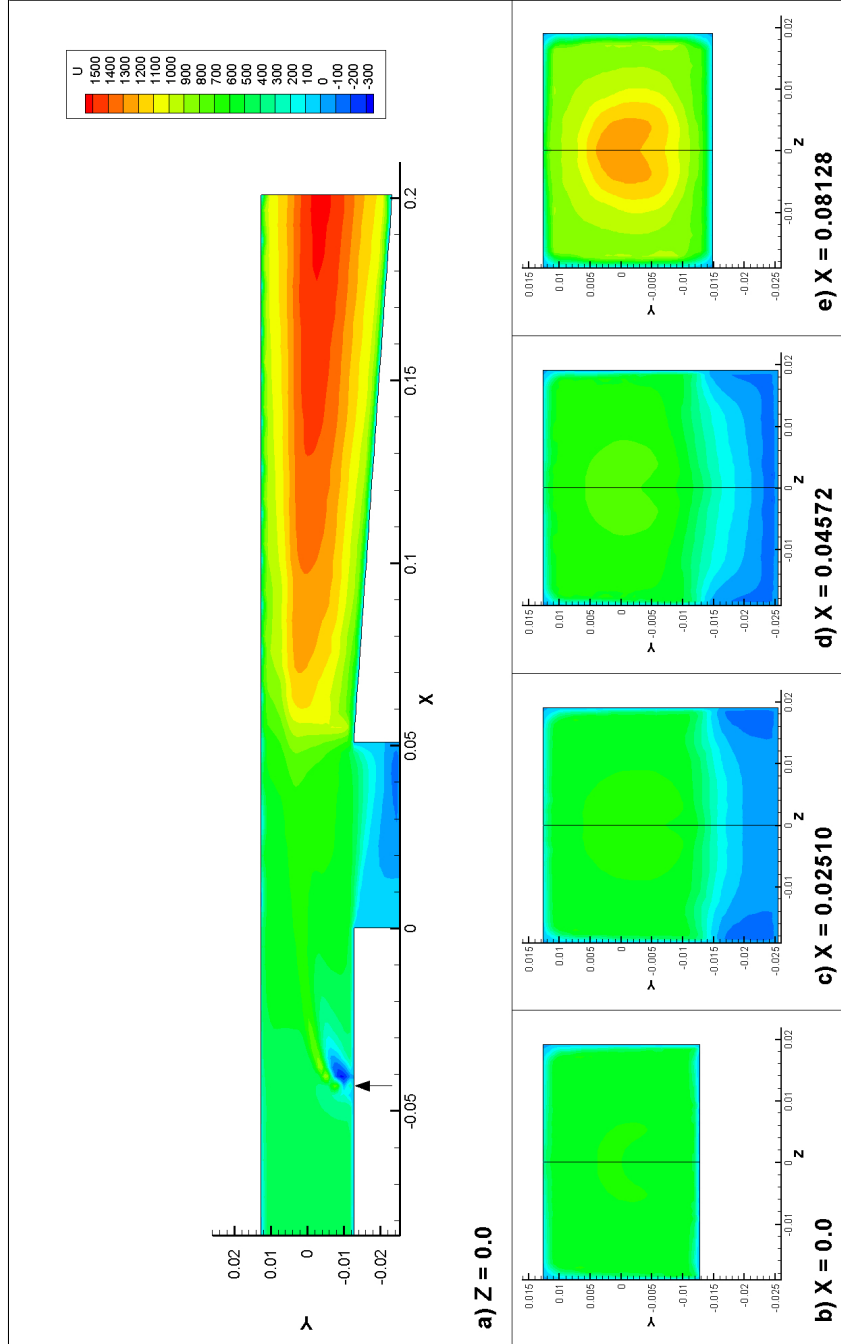
Figure A.12: Contours of axial velocity in meters per second from Fluent on the (a) combustor symmetry plane and Z-Y planes at (b) $x = 0.0$ m, (c) $x = 0.02540$ m, (d) $x = 0.04572$ m and (e) $x = 0.08128$ m.
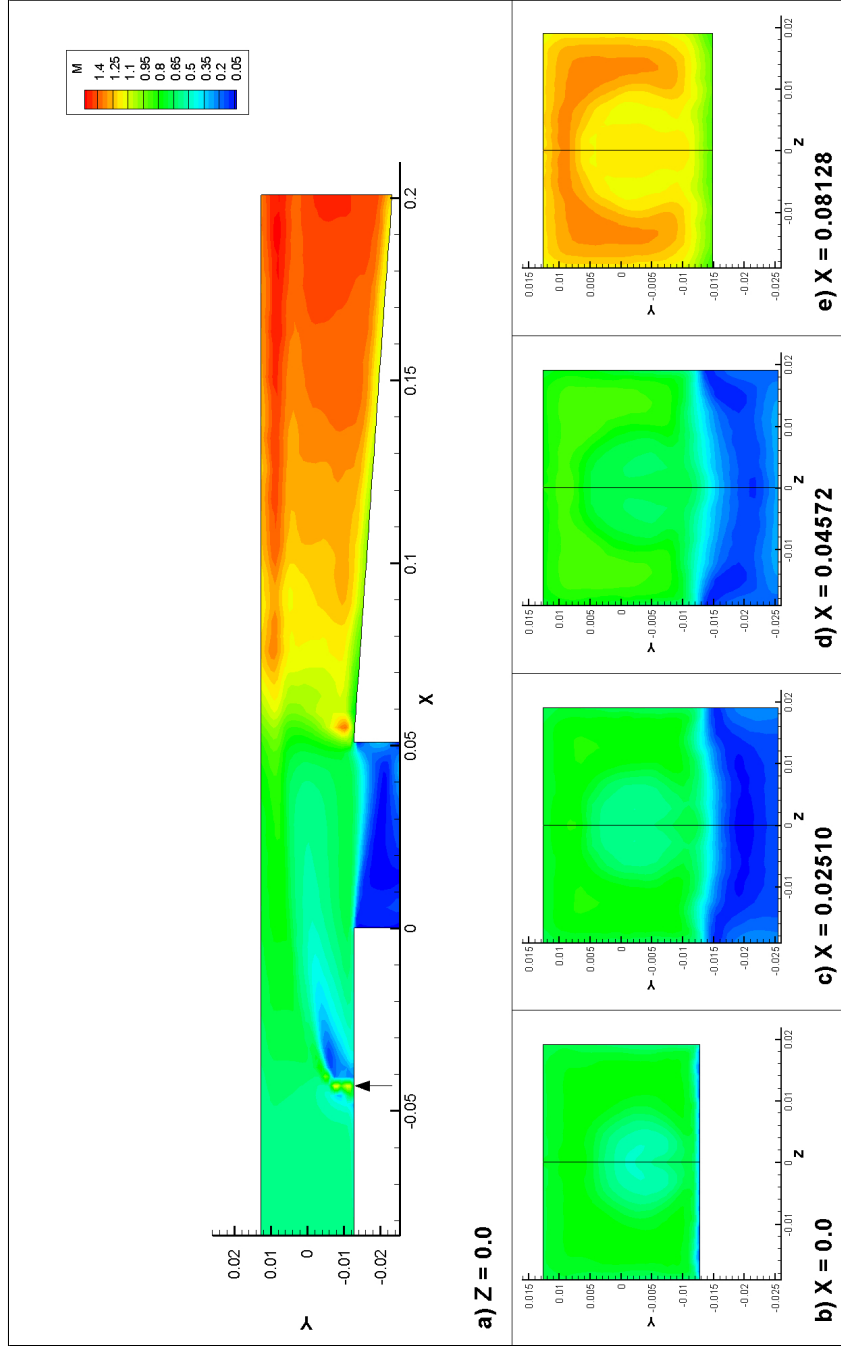
Figure A.13: Contours of Mach number from Fluent on the (a) combustor symmetry plane and Z-Y planes at (b) $x = 0.0$ m, (c) $x = 0.02540$ m, (d) $x = 0.04572$ m and (e) $x = 0.08128$ m.

Figure A.14: Contours of static pressure in Pascals from Fluent on the (a) combustor symmetry plane and Z-Y planes at (b) $x = 0.0$ m, (c) $x = 0.02540$ m, (d) $x = 0.04572$ m and (e) $x = 0.08128$ m.
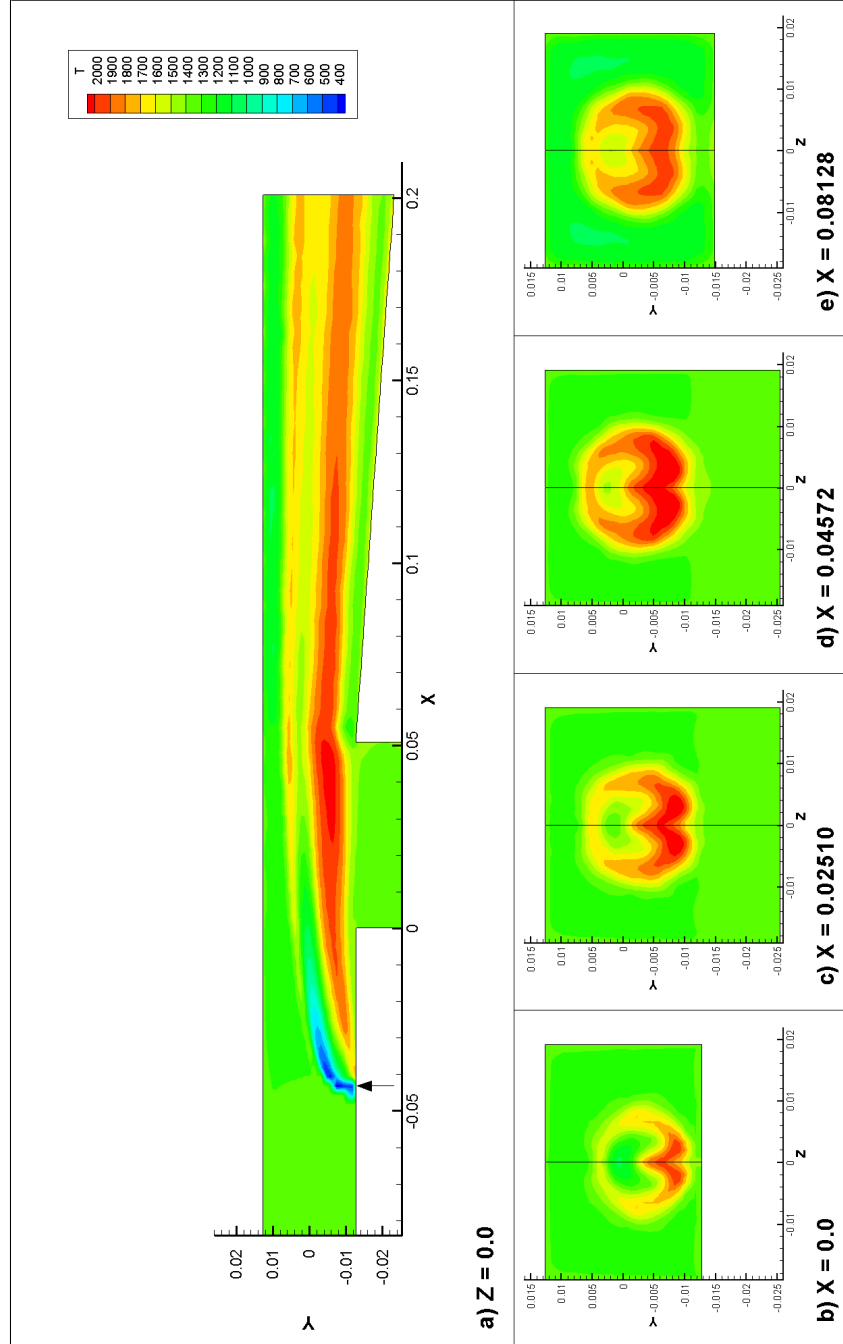
Figure A.15: Contours of static temperature in Kelvin from Fluent on the (a) combustor symmetry plane and Z-Y planes at (b) $x = 0.0$ m, (c) $x = 0.02540$ m, (d) $x = 0.04572$ m and (e) $x = 0.08128$ m.
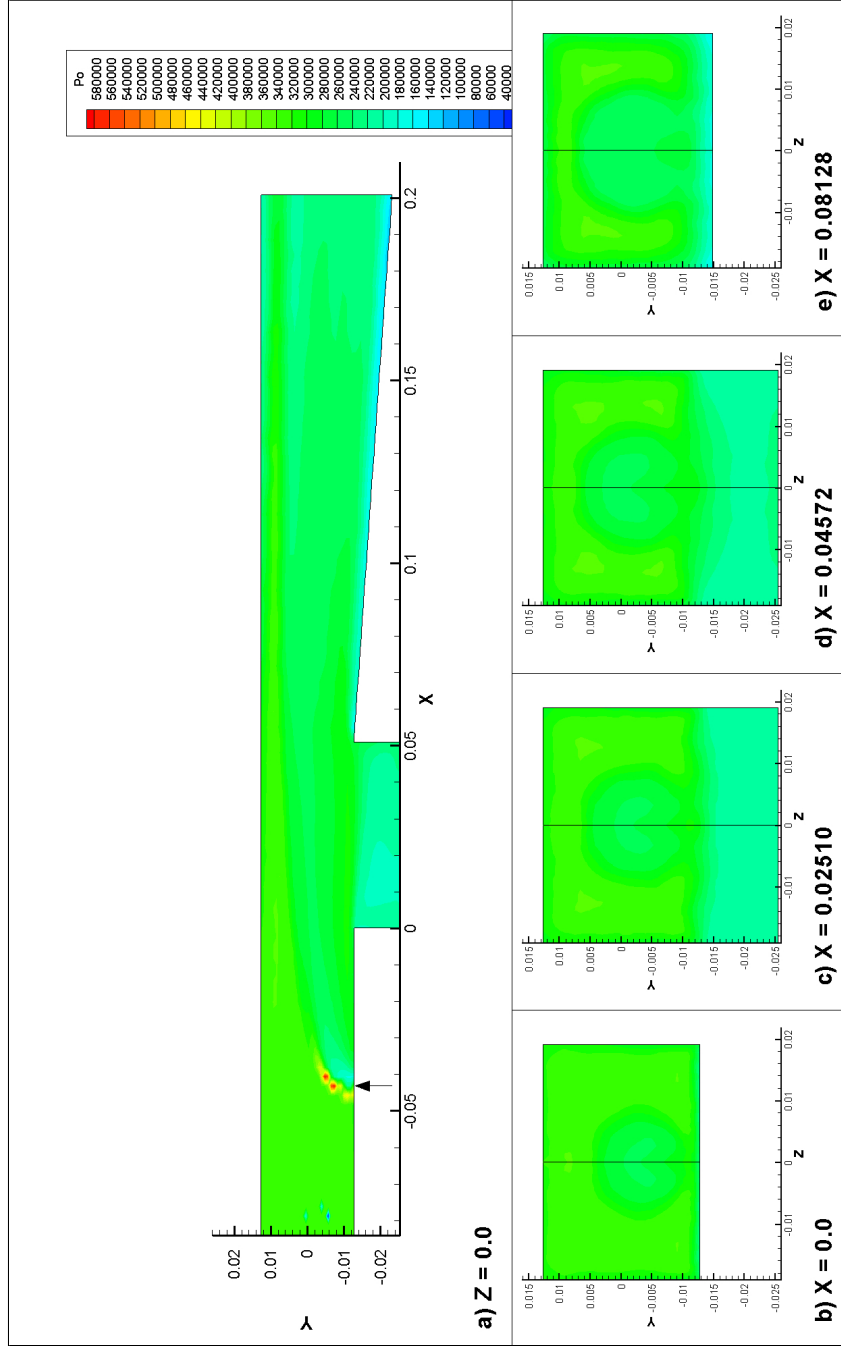
Figure A.16: Contours of stagnation pressure in Pascals from Fluent on the (a) combustor symmetry plane and Z-Y planes at (b) $x = 0.0$ m, (c) $x = 0.02540$ m, (d) $x = 0.04572$ m and (e) $x = 0.08128$ m.
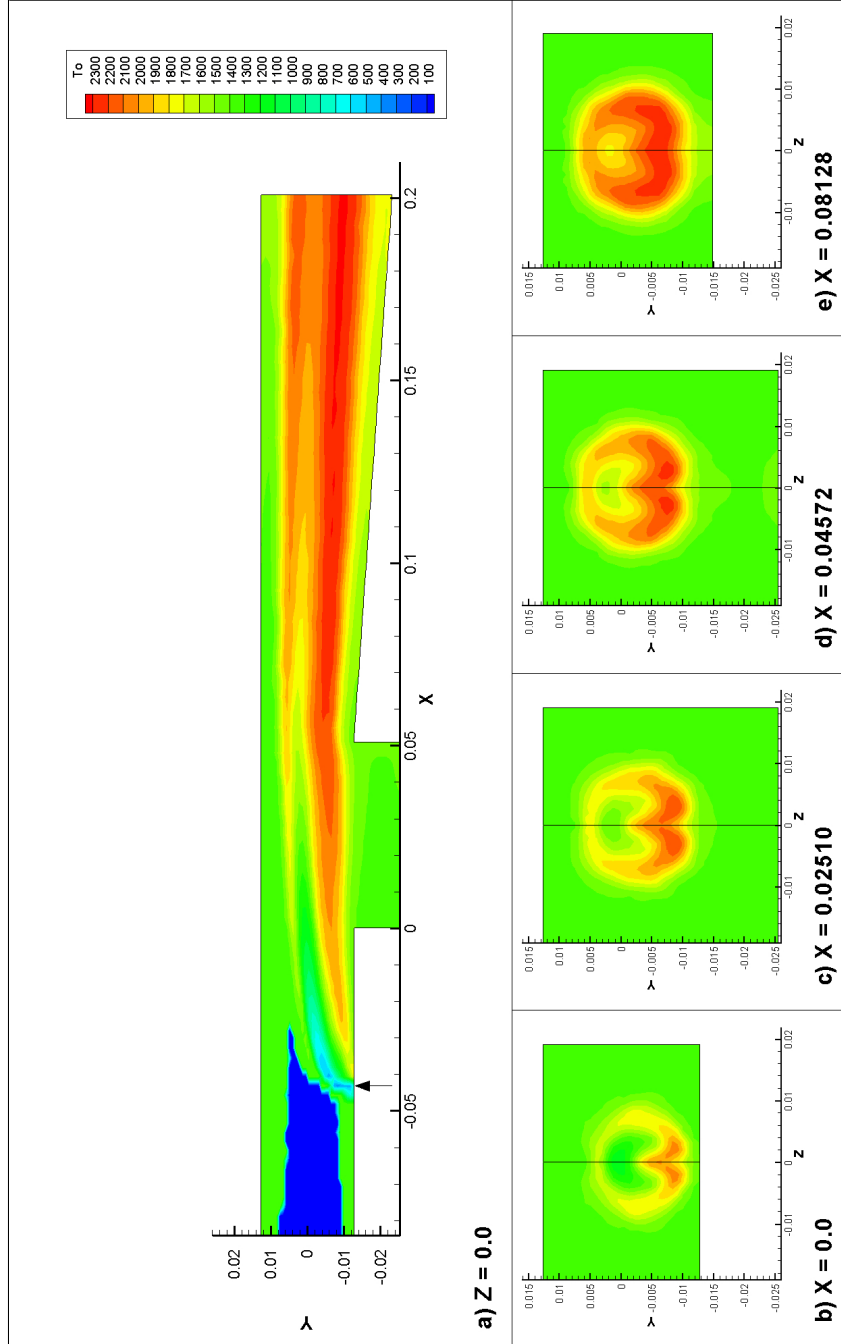
Figure A.17: Contours of stagnation temperature in Kelvin from Fluent on the (a) combustor symmetry plane and Z-Y planes at (b) $x = 0.0$ m, (c) $x = 0.02540$ m, (d) $x = 0.04572$ m and (e) $x = 0.08128$ m.
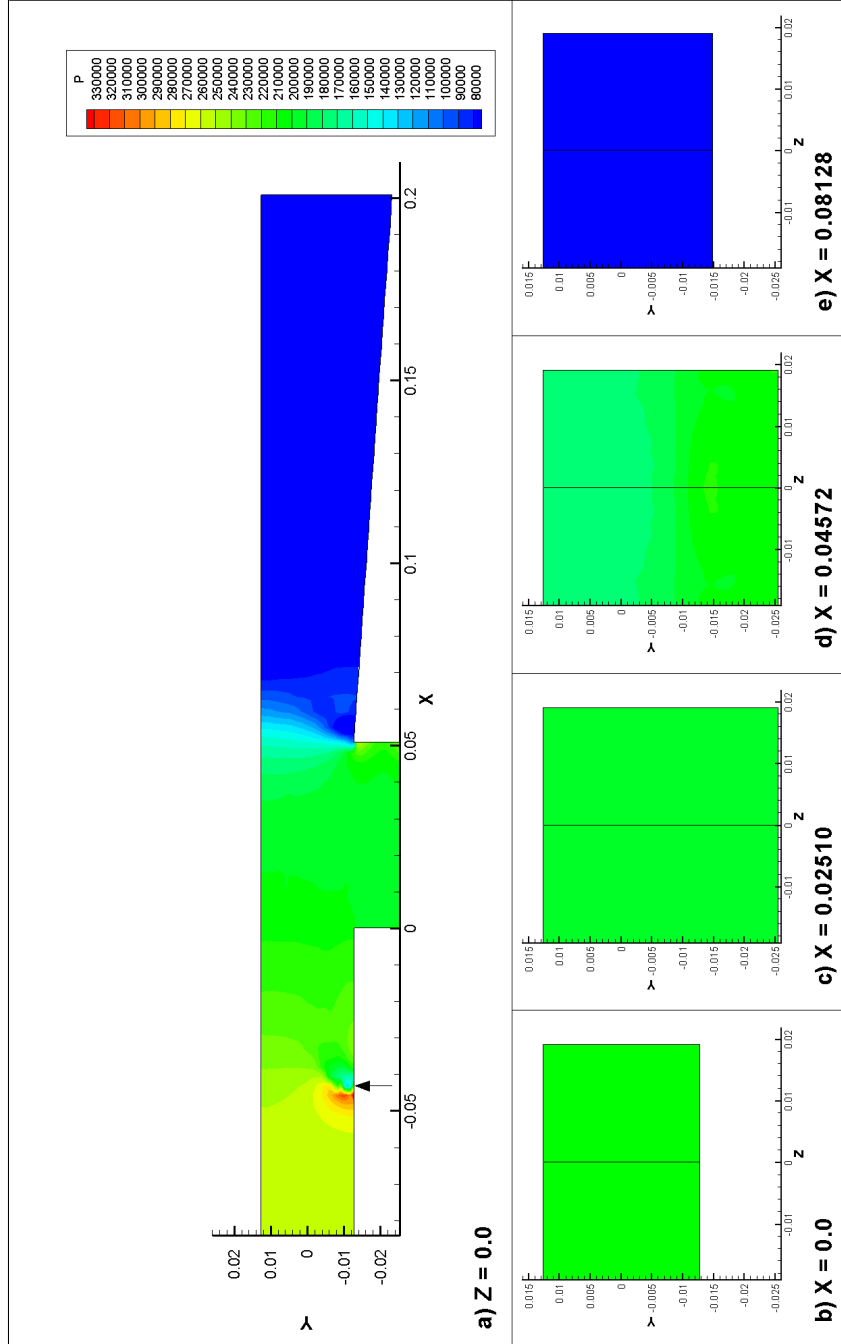
Figure A.18: Contours of fuel mass-fraction from Fluent on the (a) combustor symmetry plane and Z-Y planes at (b) $x = 0.0$ m, (c) $x = 0.02540$ m, (d) $x = 0.04572$ m and (e) $x = 0.08128$ m.

Figure A.19: Contours of oxidizer mass-fraction from Fluent on the (a) combustor symmetry plane and Z-Y planes at (b) $x = 0.0$ m, (c) $x = 0.02540$ m, (d) $x = 0.04572$ m and (e) $x = 0.08128$ m.
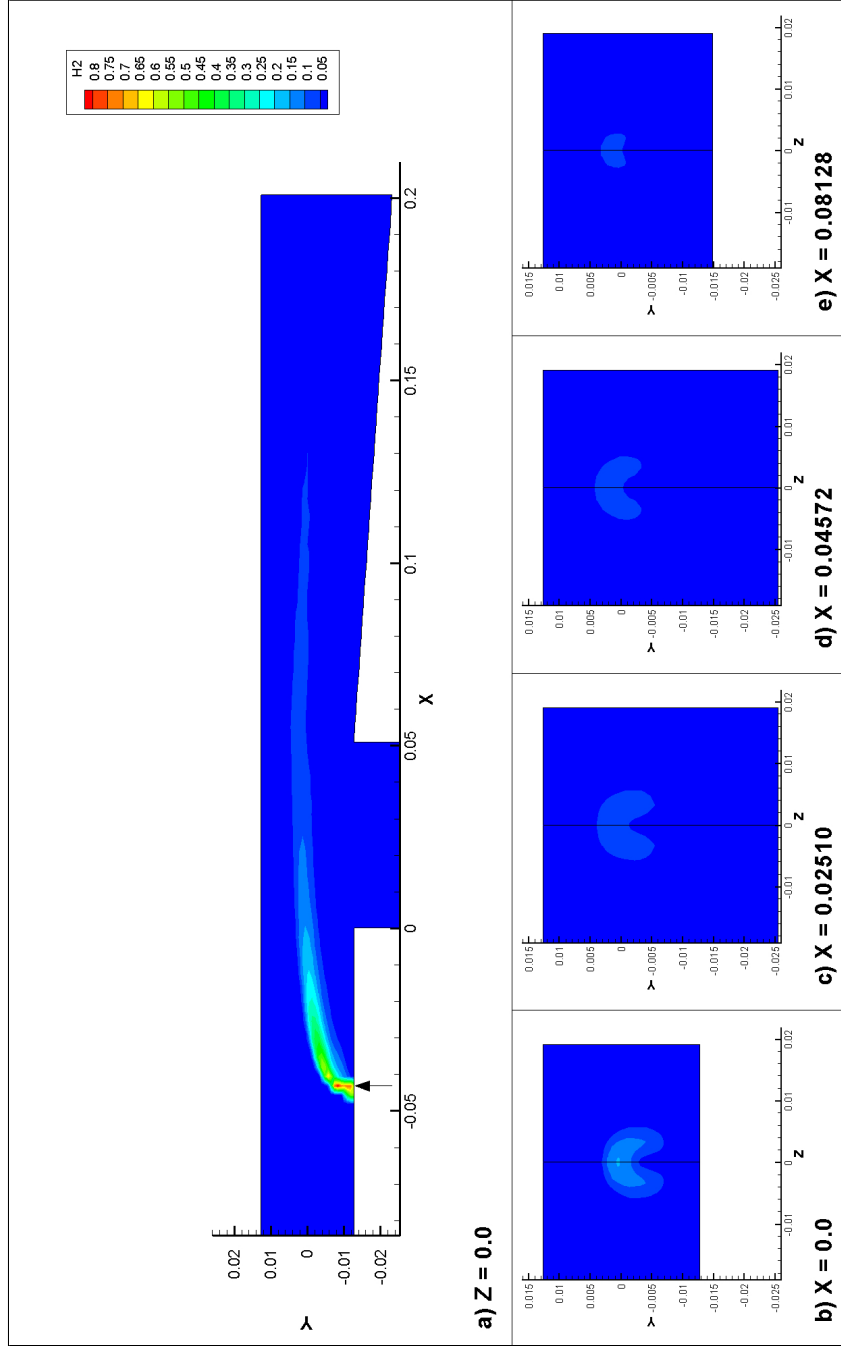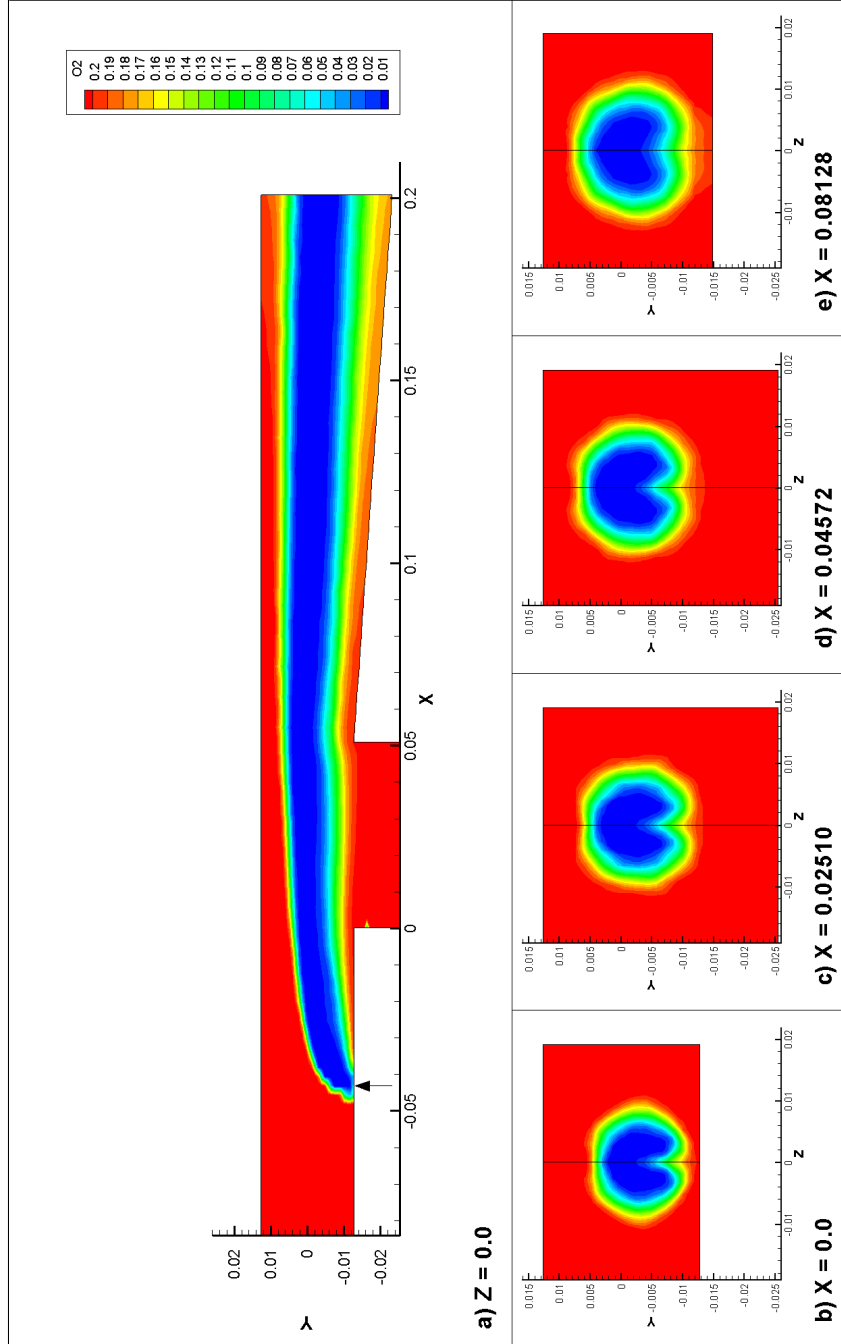
A.2.3.1   One-dimensional Combustor Quantities

The one-dimensional, planar integrated quantities for both simulations are given in Figures A.20 and A.21. These profiles have been calculated as a function of axial position using a local density weighting,

$$(A.9) \qquad \tilde{G}(x) = \frac{\int_{P(y,z)} \rho G dP}{\int_{P(y,z)} \rho dP}$$

where G is the local quantity value, ρ the local mass density and $P(y,z)$ the Z-Y integration plane.

As discussed earlier, the axial velocity profiles of the two simulations show good agreement while the static temperatures reached by the CFD++ simulation exceed those predicted by the Fluent code. The planar integrated Mach number simulated by Fluent is marginally higher due to this difference. Again, the sonic location predicted by both software packages was comparable.

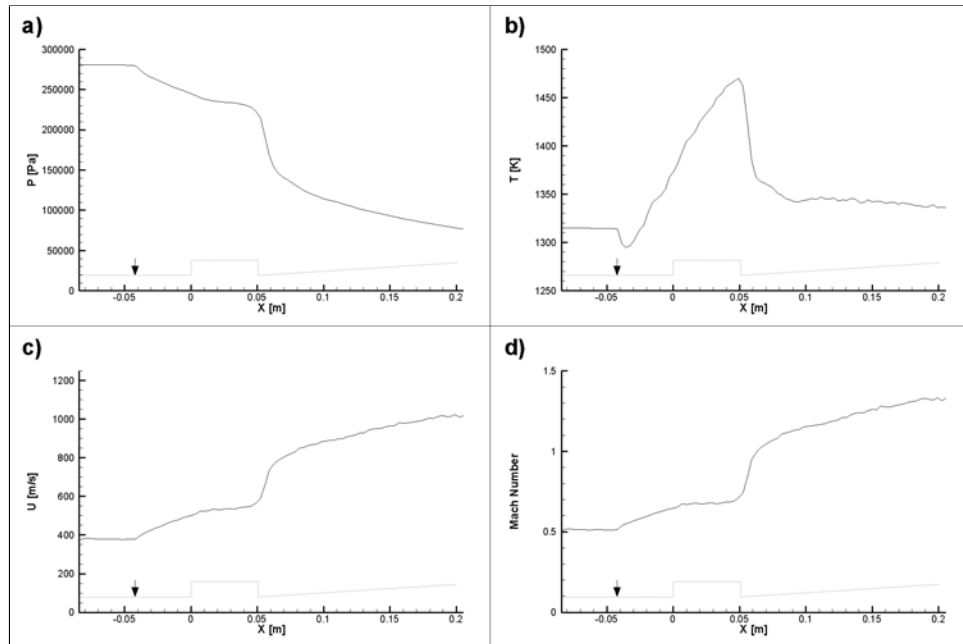Figure A.20: One-dimensional, planar integrated quantities from CFD++: (a) static pressure, (b) static temperature, (c) axial velocity and (d) Mach number in solid lines with test-section geometry in dotted lines (Arrow denotes fuel injector location).
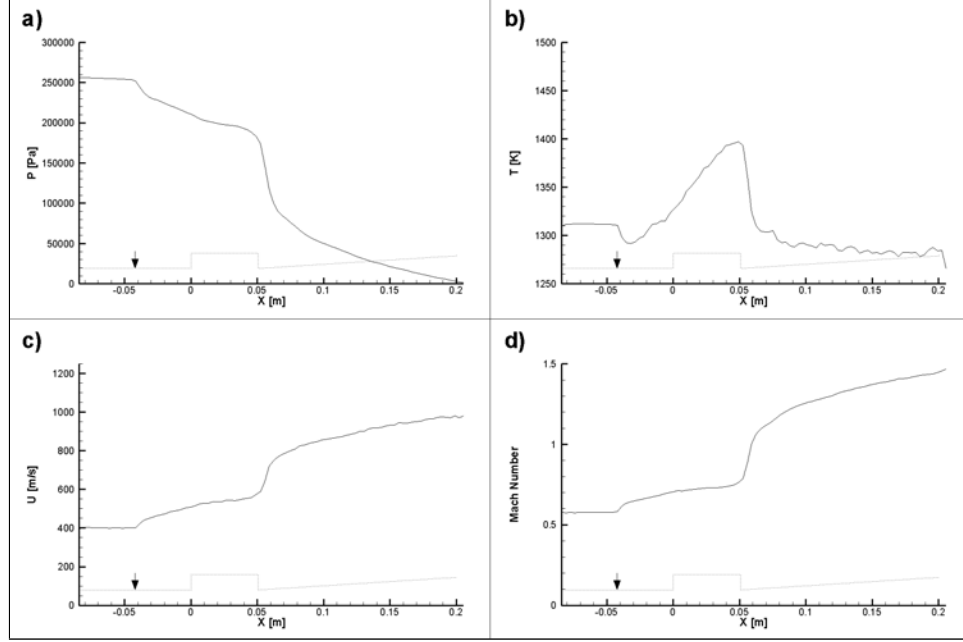
Figure A.21: One-dimensional, planar integrated quantities from Fluent: (a) static pressure, (b) static temperature, (c) axial velocity and (d) Mach number in solid lines with test-section geometry in dotted lines (Arrow denotes fuel injector location).

A.2.4 Heat-release Distribution

The most difficult quantity for any simulation to correctly predict is arguably the distribution of heat released from the fuel. This has already been mentioned as one of the factors creating differences between the two simulations that have been presented. The heat-release is not a quantity that is readily accessible from most computational packages. To aide in this analysis, the local heat release has been calculated from both sets of simulation results via

$$(A.10) \quad \frac{Dh}{Dt} = \rho V_{cell} \left[\left(u_x \frac{\partial h}{\partial x} + u_y \frac{\partial h}{\partial y} + u_z \frac{\partial h}{\partial z} \right) - \frac{\kappa}{\rho C_p} \left(\frac{\partial^2 h}{\partial x^2} + \frac{\partial^2 h}{\partial y^2} + \frac{\partial^2 h}{\partial z^2} \right) \right],$$

where h is the enthalpy, V_{cell} is the cell volume, u is the component of velocity in a particular coordinate direction, κ is the thermal conductivity and C_p the ratio of specific heats at constant pressure.

The results of this calculation are shown in Figures A.22 and A.23. The CFD++ sim-

128

ulation has a fairly localized heat-release distribution, with discrete fluid structures, e.g. shocks, being strongly coupled to the local areas of heat-release. This is what would be expected from a simulation with high rates of reaction.

The Fluent simulation shows a much more diffuse heat-release distribution. As compared to the CFD++ case, the rates at which the chemical reactions progress is moderated by the imposed flamelet model. The overall structure of the distribution shows some compressible interactions, however it mostly appears to be dictated by the reduced reaction rates.

Figure A.22: Contours of heat release in Watts per meter cubed from CFD++ on the (a) combustor symmetry plane and Z-Y planes at (b) $x = 0.0$ m, (c) $x = 0.02540$ m, (d) $x = 0.04572$ m and (e) $x = 0.08128$ m.
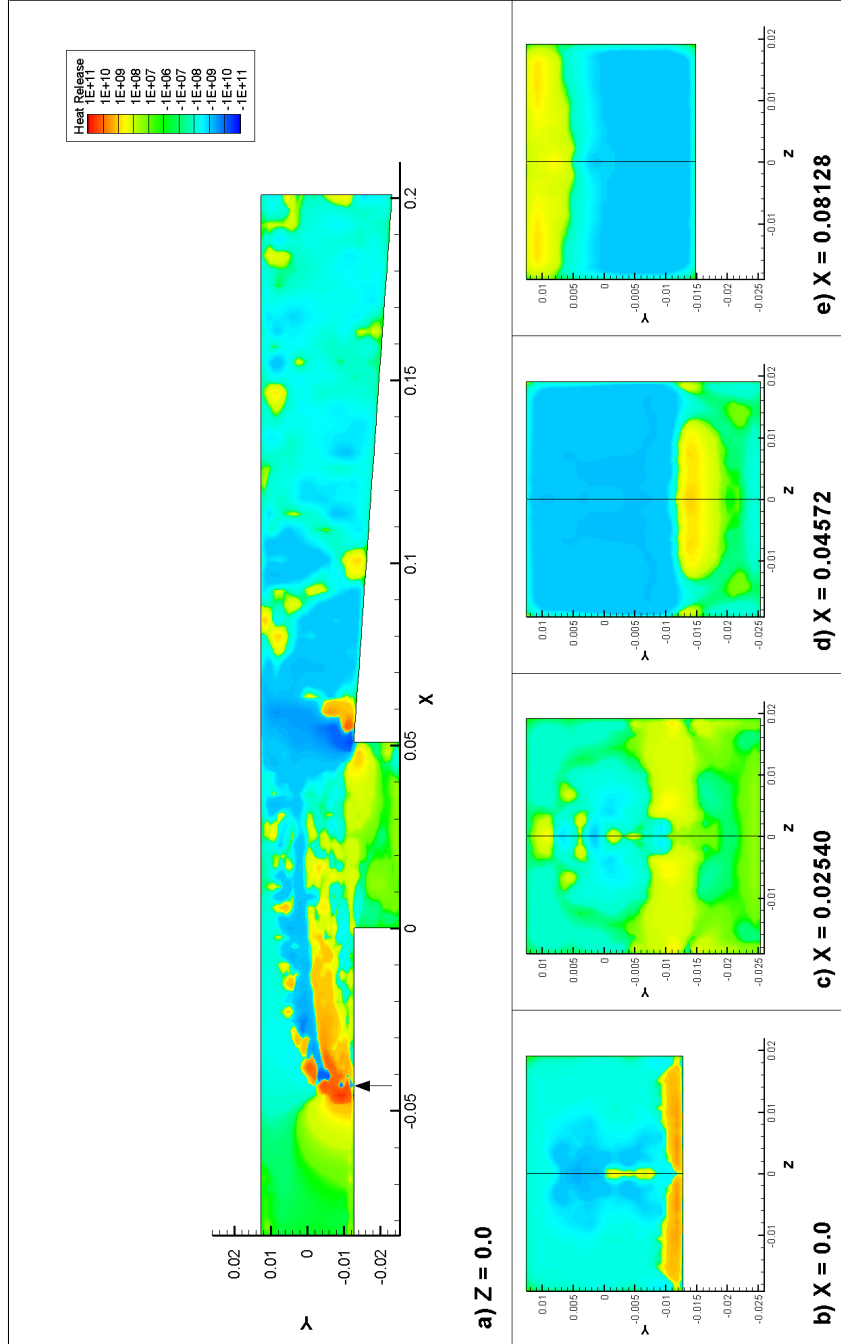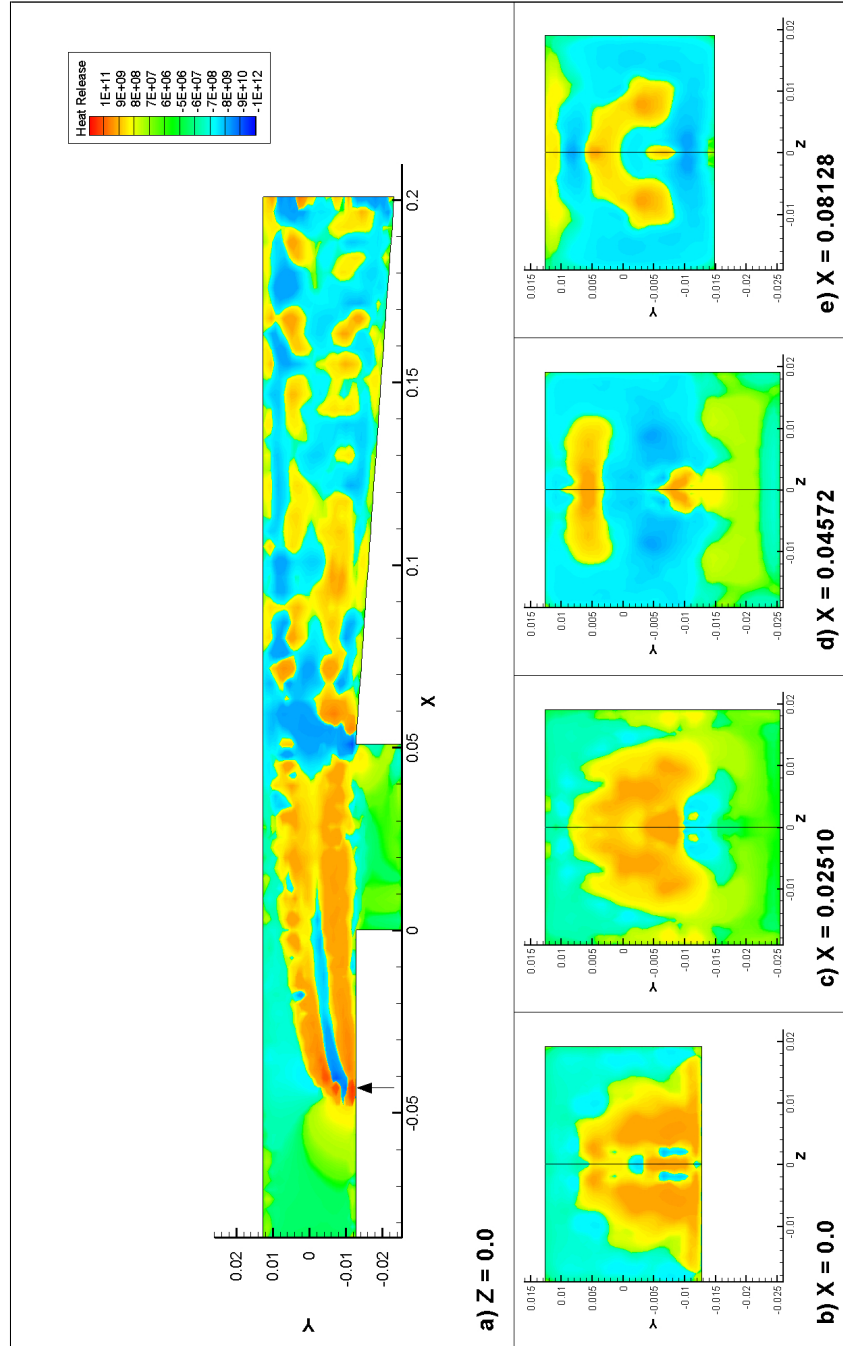
Figure A.23: Contours of heat release in Watts per meter cubed from Fluent on the (a) combustor symmetry plane and Z-Y planes at (b) $x = 0.0$ m, (c) $x = 0.02540$ m, (d) $x = 0.04572$ m and (e) $x = 0.08128$ m.

The three-dimensional heat release information has been presented as line-of-sight projections in Figures A.24(a) and A.25(a), and as a one-dimensional integrated quantity in Figures A.24(b) and A.25(b). The line-of-sight projections provide a good contrast between the two simulations. The impact of the flamelet model on the finite-rate chemistry is very evident in Figure A.25(a) where heat is being released over a large region inside the combustor. While in contrast to this the CFD++ simulation shows that the bulk of the heat is deposited into the flow just aft of the fuel injector.

Both simulations predict a region of recombination, or absorption of heat into chemical bonds, as the flow transits the thermal throat, and sonic location. Once through this choke point the forward reactions begin to progress again with heat being releasing as the flow expands and is exhausted.
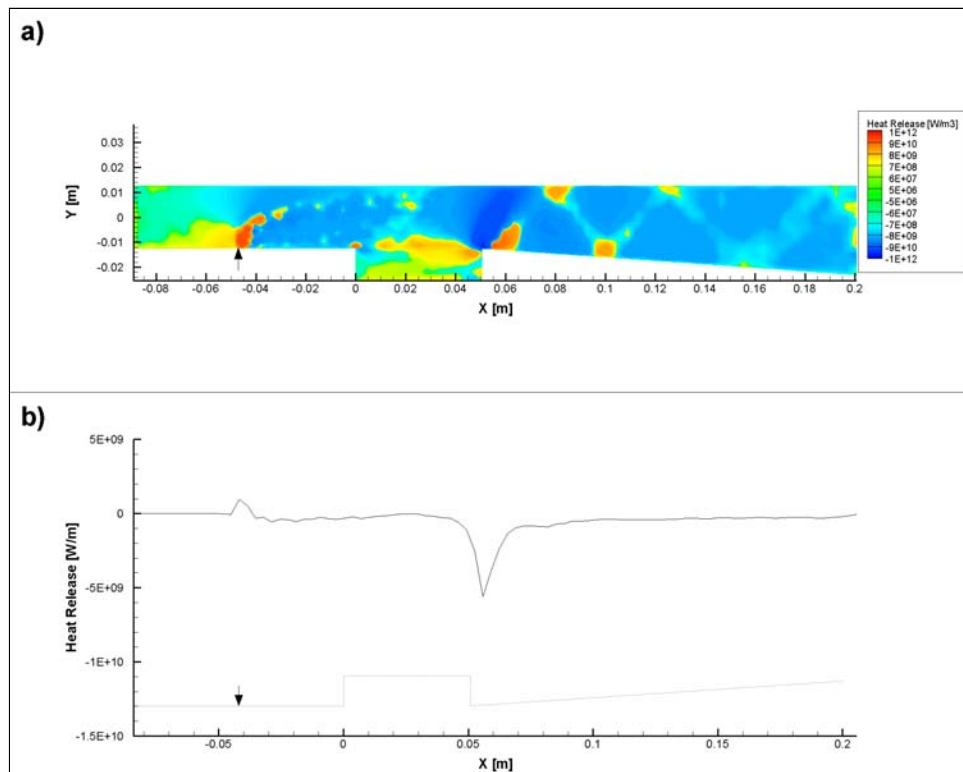
Figure A.24: Heat release distribution from CFD++ as (a) line-of-sight projection and (b) one-dimensional, planar integrated quantity, in solid line and test-section geometry in dotted line.
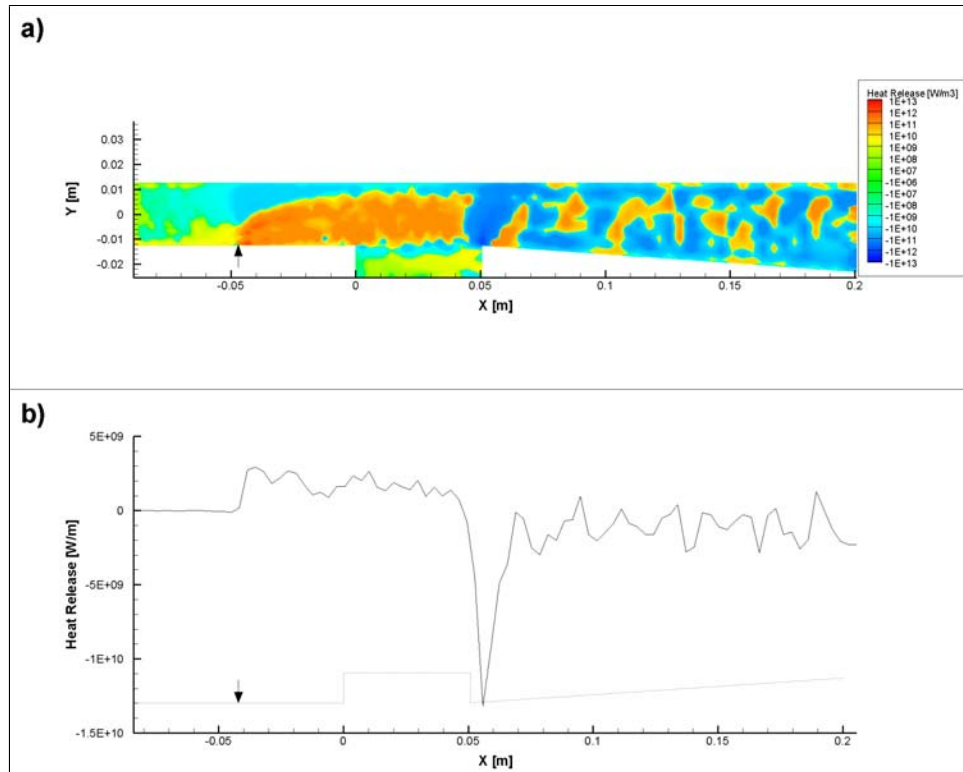
Figure A.25: Heat release distribution from Fluent as (a) line-of-sight projection and (b) one-dimensional, planar integrated quantity, in solid line and test-section geometry in dotted line.

A.3 Unsteady Simulations

Two unsteady simulations were created using the CFD++ software package. The goal of these two simulations was to evaluate how readily the code could be used to predict the unsteady behavior of the combustor. The first unsteady simulation was that of a drop in inlet stagnation pressure, while the second was a drop in fuel injector stagnation pressure.

A.3.1 Inlet Stagnation Pressure Drop

An unsteady simulation was created to examine the impact that a step-drop in stagnation pressure at the combustor inlet would have on the operation of the combustor. The stagnation pressure at the inlet was initially set to be 814 kPa and then instantaneously halved. The resulting behavior of the static pressure field within the combustor is shown in Figure A.26. While the combustor remained operating under ramjet-mode, the step-

133

drop in stagnation pressure created a static pressure wave that propagated forward to the thermal choke point in the combustor and then reflected back upstream toward the combustor entrance.

Figure A.26: Axial upper wall static pressure profile as a function of time during an inlet stagnation pressure drop. (Note: front wall of cavity is located at x = 0.45275 m).

Figures A.27 and A.28 show the pressure wave as it transits the fuel plume. The areas of locally higher pressure breakup the continuity of the jet, with sections of the fuel plume showing locally higher mole fractions of uncombusted fuel. In the simulation, it is impossible to extinguish the flame as only the constituent chemical reactions are being calculated and not the physics of the actual flame front.

The flow can be seen to remain choked as the pressure wave reflects back upstream.

The location does shift further downstream into the diverging section of the combustor as the wave reaches this location, and then return to its previous position directly after the wave leaves.
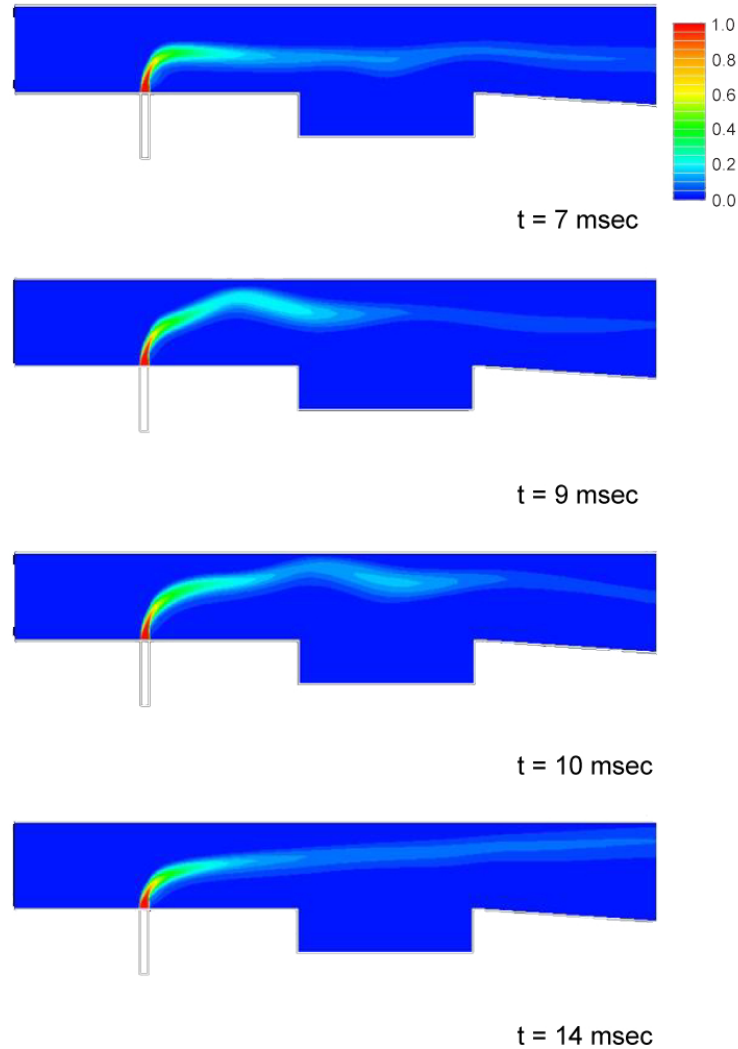
Figure A.27: Contours of mole fraction of H_2 as a function of time.

A.3.2 Fuel Pressure Drop

A second unsteady simulation was conducted in which the fuel stagnation pressure was reduced. The combustor continued to operate in ramjet-mode, however unlike the previous instance of inlet stagnation pressure reduction there was no observed pressure
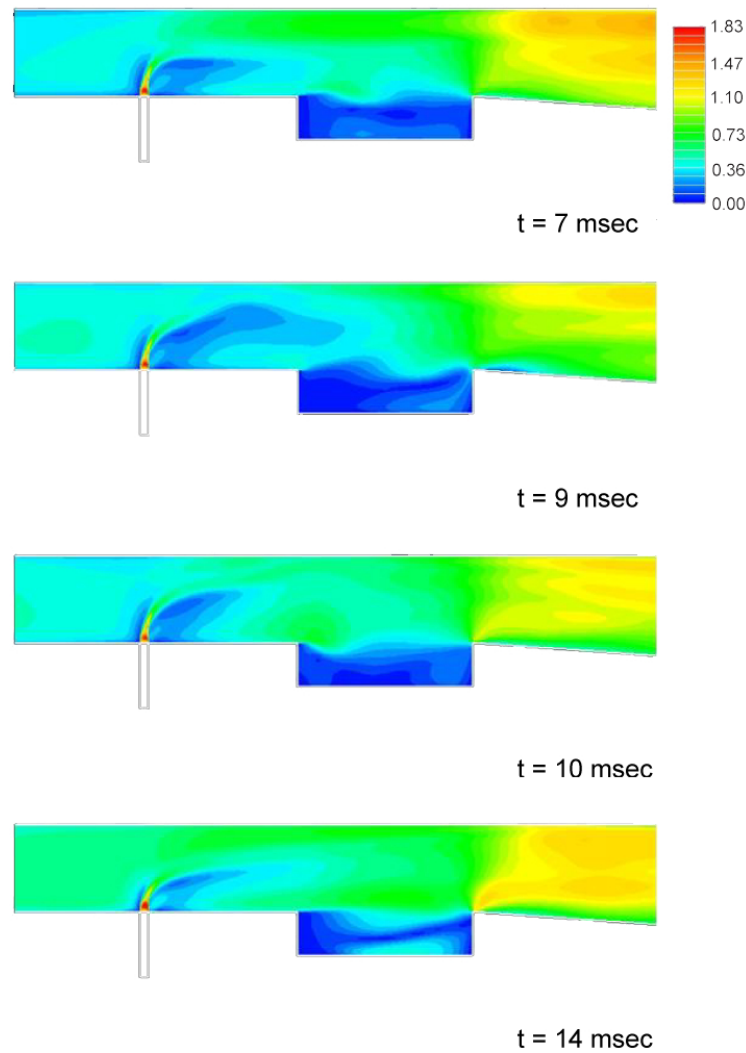
Figure A.28: Contours of Mach number as a function of time.

waves propagation through the combustor. The drop in stagnation pressure on the fuel injector reduced the amount of blockage created by jet and the combustion of the fuel itself. This is seen in Figure A.29, where the static pressure recovered forward of the injection is reduced. This is consistent with experimental observations of the isolator pressure rise in which a reduction in blockage is coupled to a proportional reduction in pseudo-shock strength. While the CFD++ simulation does not predict the shock waves that are present in the experimental case, it does capture the relationship between the combustor fueling conditions and the behavior of the coupled isolator.
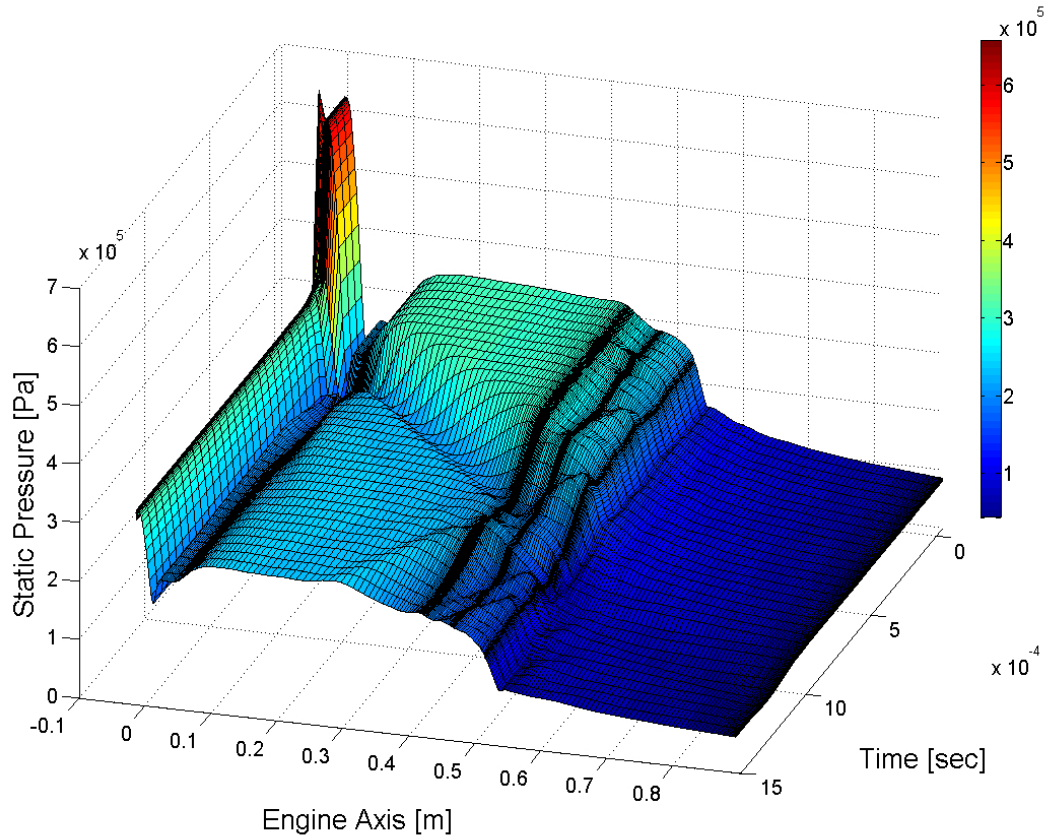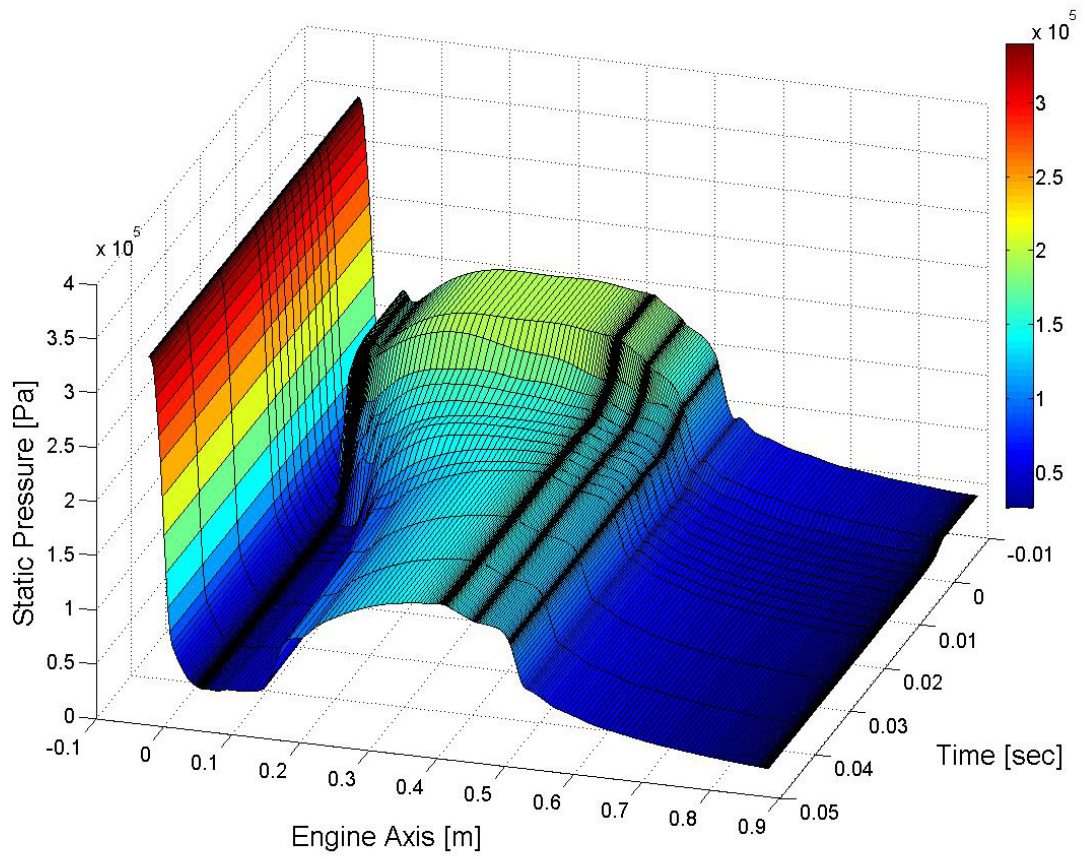
Figure A.29: Axial upper wall static pressure profile as a function of time during a fuel injector stagnation pressure drop. (Note: front wall of cavity is located at $x = 0.45275$ m).

APPENDIX B

Test-Section Viewport Alterations

2.200

0.250

Y

0

X

0

0.550

2.700   0.800   4.700   0.800   2.700   0.550

12.800

1.100   1.100   1.100   1.100

12 x R0.1875

A1 A2 A3 A4 A5 A6 A7 A8 A9 A10 A11 A12 A13 A14 A15 A16 A17 A18 A19 A20 A21 A22 A23 A24 A25 A26 A27 A28 A29 A30

TAG	X LOC	Y LOC	SIZE
A1	1.100	0.200	
A2	2.000	0.600	
A3	0.200	0.600	
A4	2.000	1.600	
A5	0.200	1.600	
A6	2.000	3.600	
A7	1.100	3.600	
A8	0.200	3.600	
A9	2.000	4.500	
A10	0.200	4.500	
A11	2.000	5.350	
A12	0.200	5.350	
A13	2.000	5.850	
A14	0.200	5.850	
A15	2.000	6.700	
A16	0.200	6.700	
A17	0.200	7.700	
A18	2.000	7.700	
A19	0.200	8.700	
A20	2.000	8.700	
A21	1.100	9.200	
A22	2.000	9.600	
A23	0.200	9.600	
A24	2.000	10.600	
A25	0.200	10.600	
A26	2.000	11.600	
A27	0.200	11.600	
A28	2.000	12.600	
A29	1.100	12.600	
A30	0.200	12.600	Ø 0.20 THRU ALL

Quantity to be Manufactured: x 2

Figure B.1: Drawing of new isolator window frame.

139
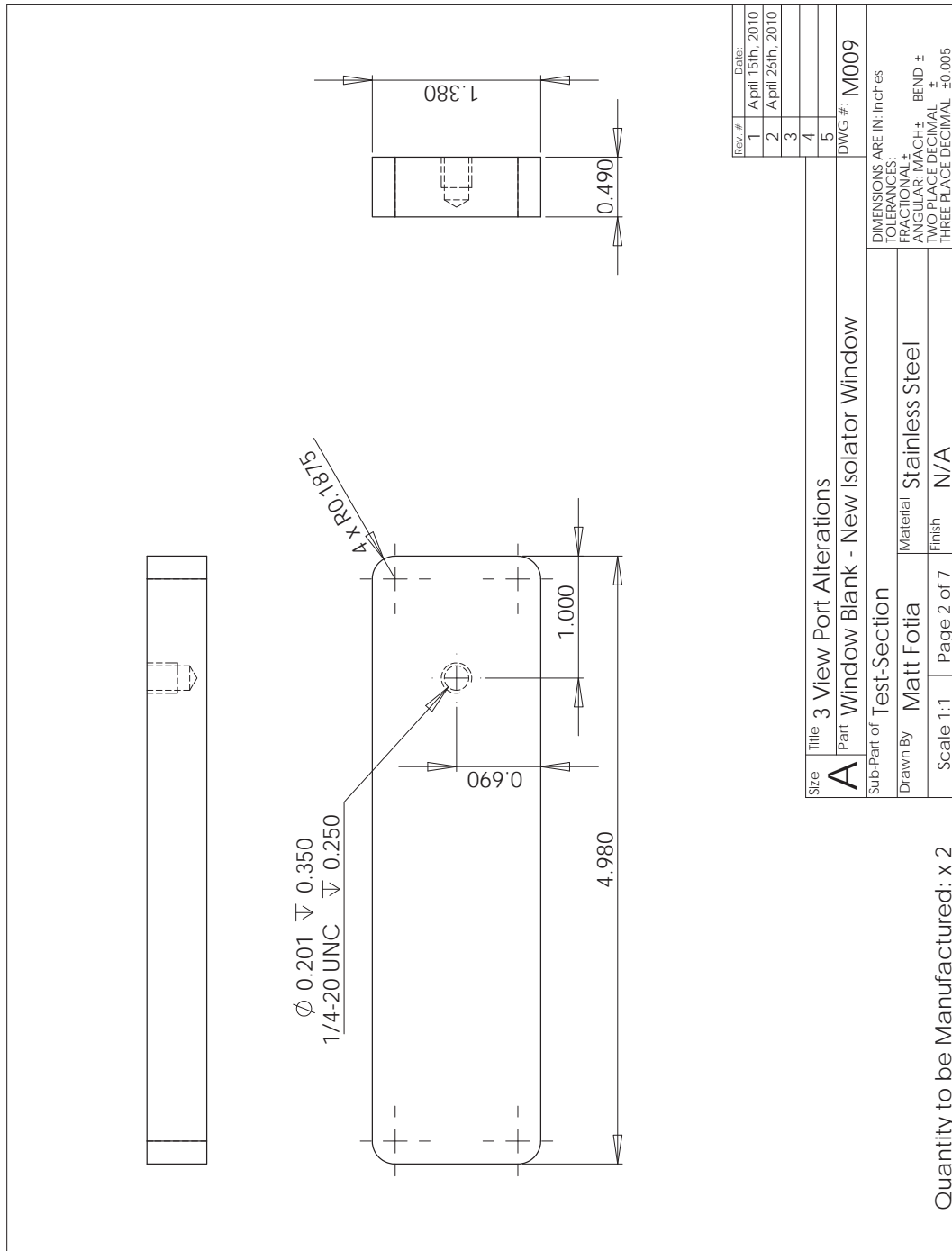
Figure B.2: Drawing of new isolator window blank.
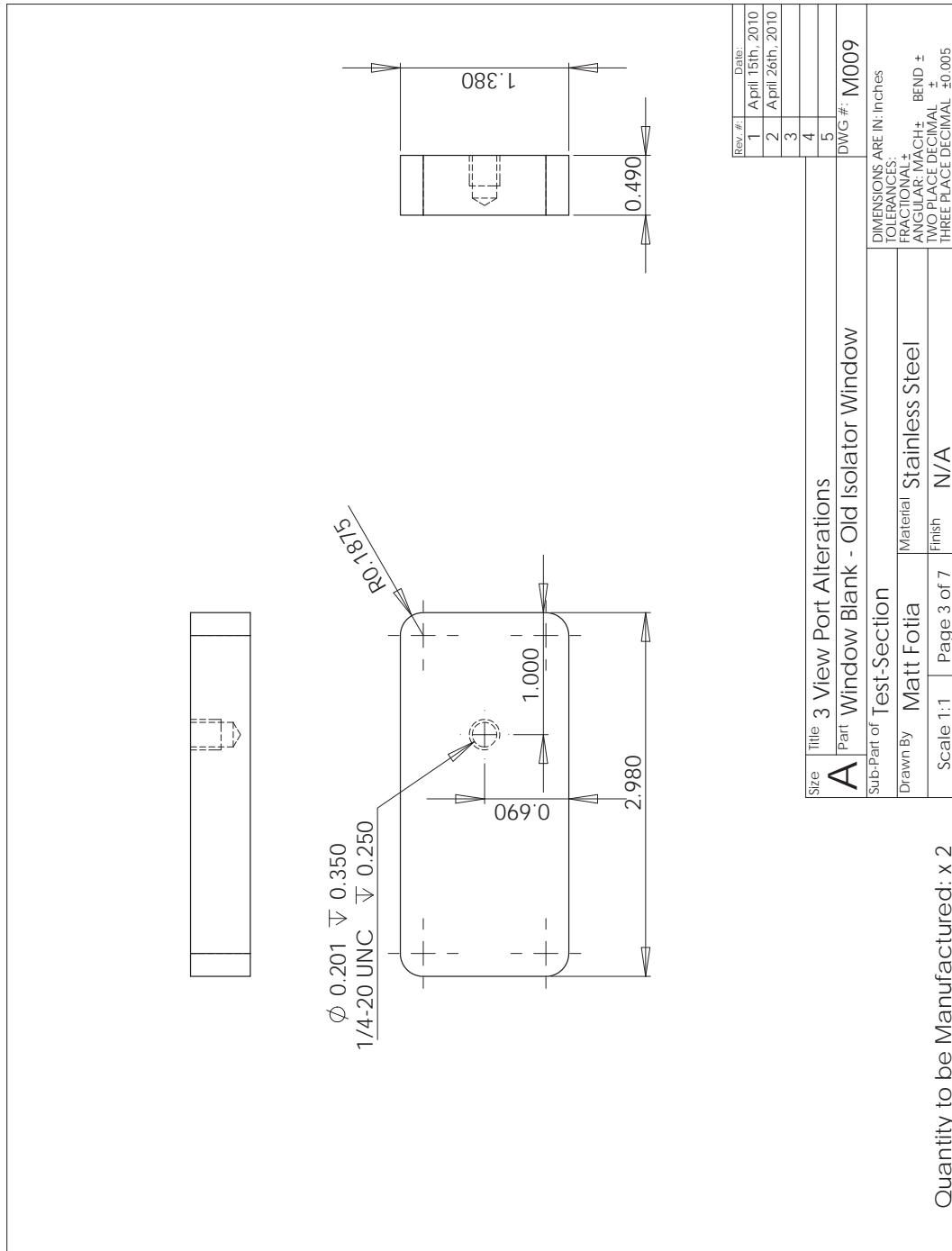
Figure B.3: Drawing of old isolator window blank.

Isometric View

Right-Side View

Top View

Left-Side View (Window Frame Removed)
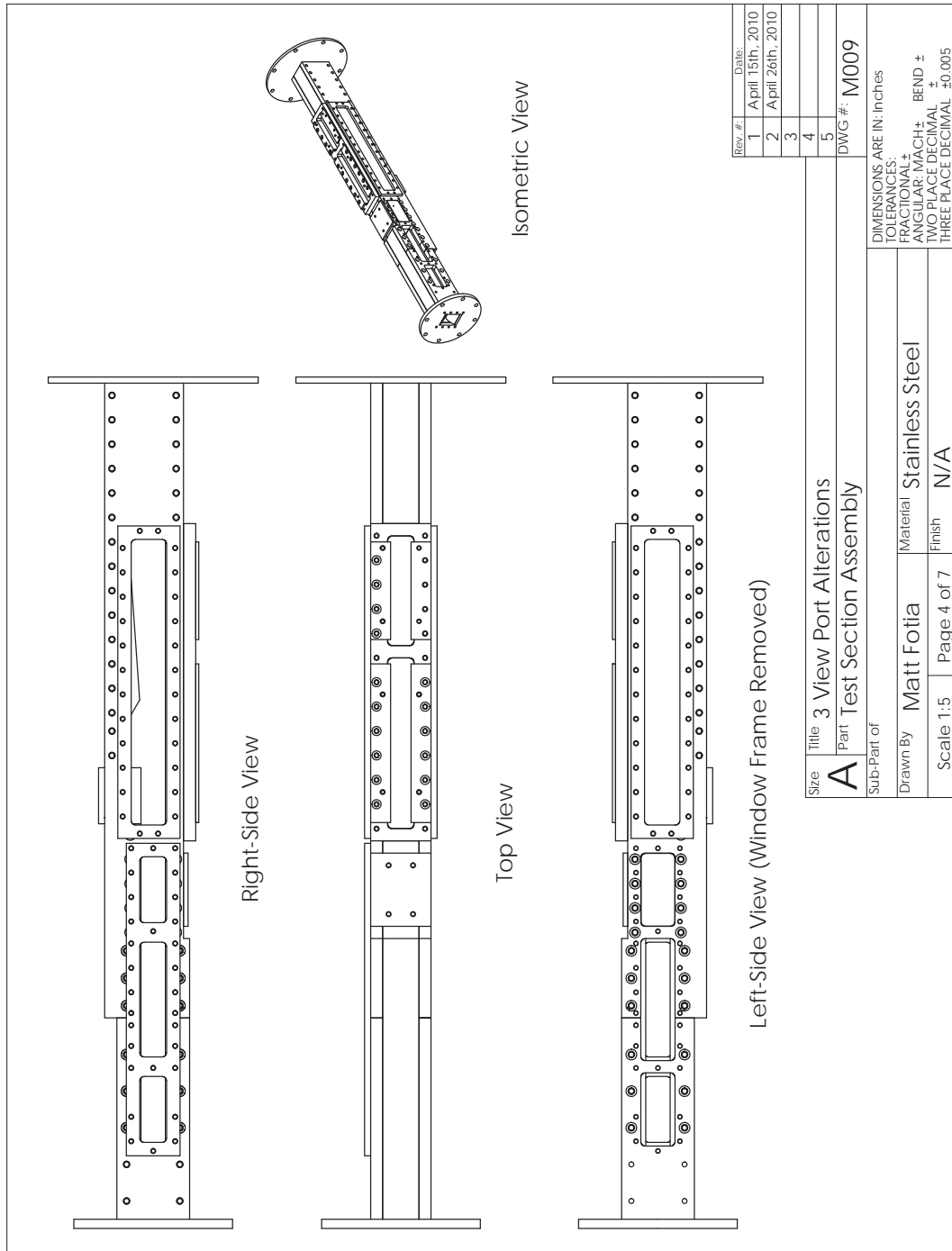
Figure B.4: Drawing of new test-section assembly.

Figure B.5: Drawing of new window detail.

Figure B.6: Drawing of side wall alterations.

Figure B.7: Drawing of side wall extension alterations.

APPENDIX C

**University of Michigan Supersonic Combustion Laboratory -
Operational Checklist**

Supersonic Combustor Experiment
Operating Checklist

1) Initialization
   a. Check that high-pressure air line is charged and not diverted to TAPS Injector Laboratory.
   b. Check that test-section in properly sealed and all flow controllers/sensors are powered.
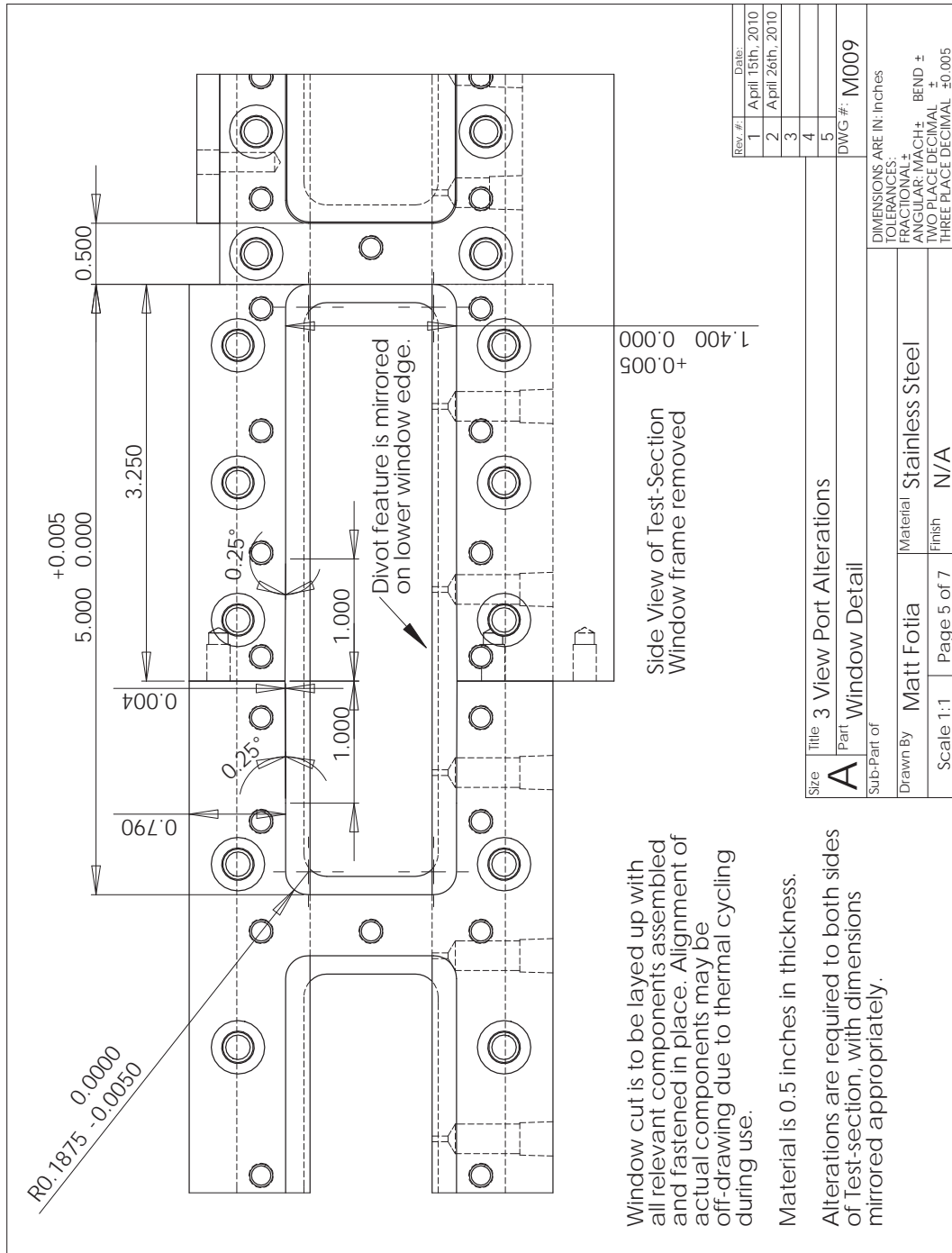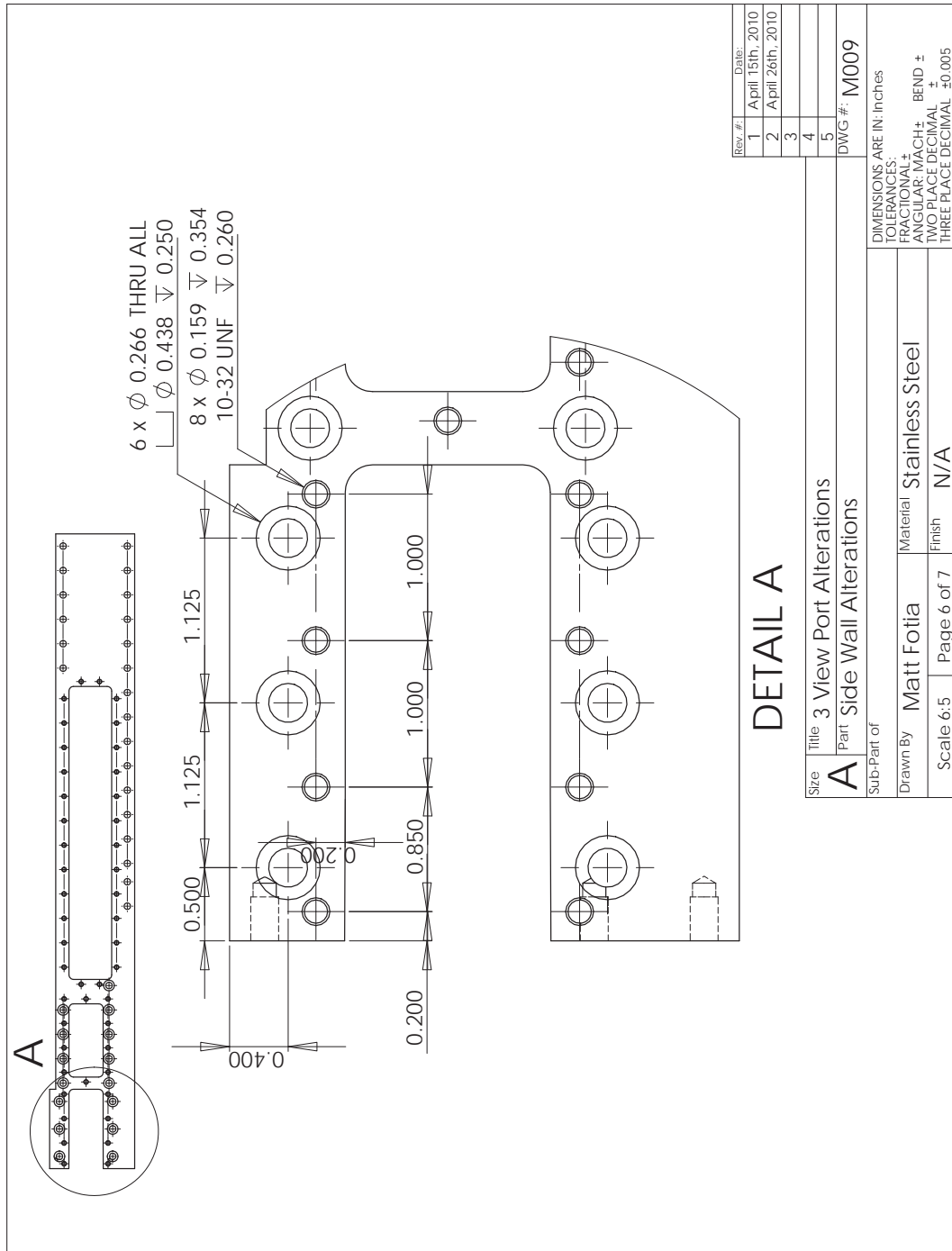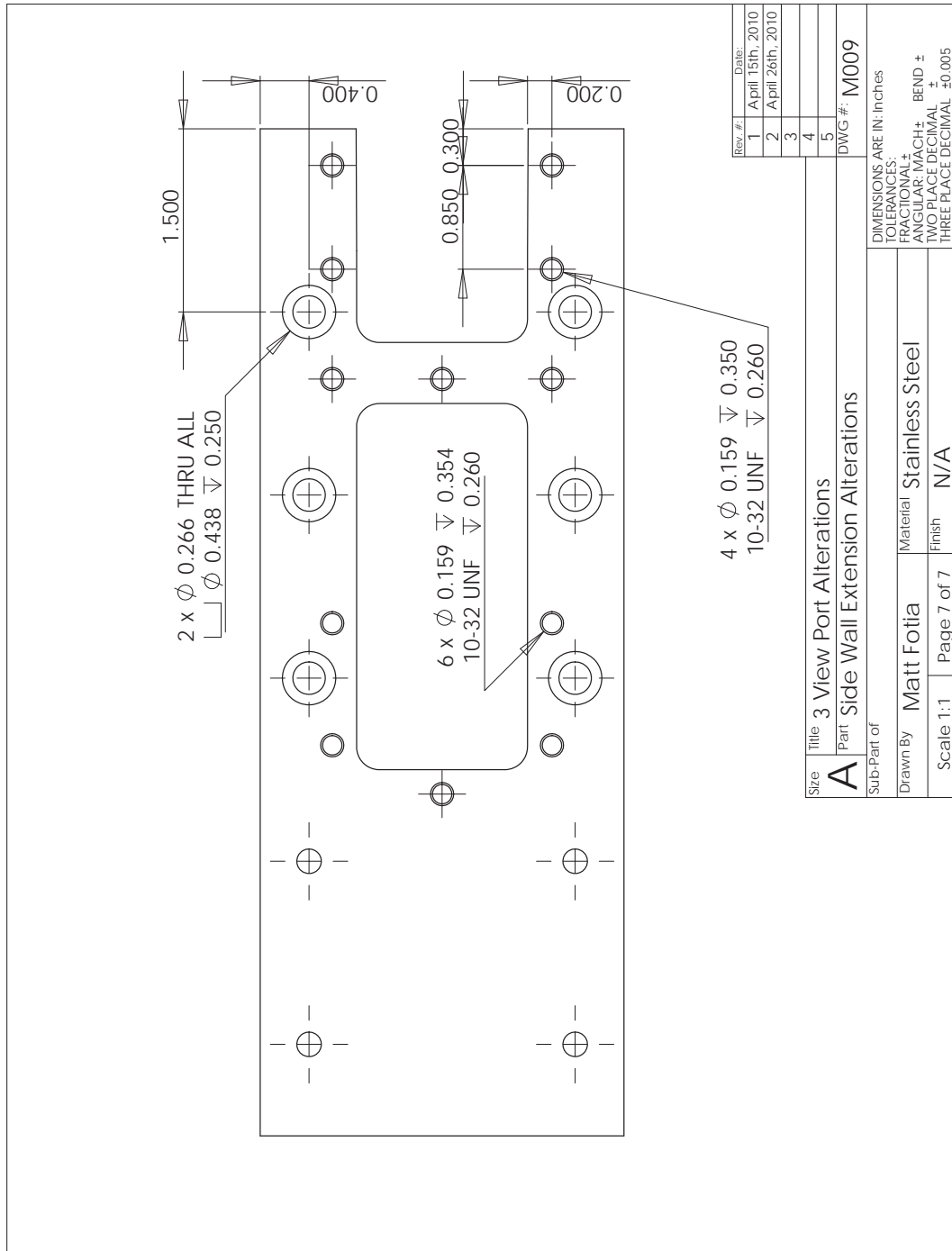   c. Check status of and open the vitiator oxidizer/fuel cylinders, and test-section fuel cylinders.
   d. Initialize Labview software and diagnostic specific equipment.
   e. Hearing protection should be worn during operation of high-pressure airline.
   f. Open high-pressure airline and bring to desired operational pressure.
   g. Test/Initialize vitiator oxidizer and fuel controllers one at a time, checking for correct controller behavior.
   h. Test/ Initialize main and pilot fuel controllers/injectors, checking for correct feed pressures.

2) Calibration
   a. Turn on Electric heater main power feed, and begin to heat high-pressure air to approximately 375 °F.
   b. Once air temperature has reached approximately 375 °F, turn off electric heater and test run the vitiator at the desired operating conditions to verify test-section inlet conditions.
   c. Allow air temperature to cool to approximately 150 °F before continuing. Change vitiator flow settings and recheck as needed.

3) Operation
   a. Turn on electric heater main power, and begin to heat high-pressure air to approximately 375 °F.
   b. Once air temperature has reached approximately 375 °F, turn off electric heater and begin full test-section operation.
   c. Allow air temperature to cool to approximately 150 °F before continuing between test runs.

4) Cool Down and Purging
   a. Once testing is complete, or when high-pressure air reservoir has reached approximately 500 psi of charge, the remaining pressurized air should be used to cool the electric heater and test-section to below 100 °F.
   b. Turn off electric heater main power.
   c. While cooling the apparatus, the vitiator oxidizer/fuel and test-section fuel cylinders should be closed.
   d. Purge the feed lines from the cylinders one at a time.
   e. Once test-section is sufficiently cooled, lower pressure of air line to approximately 14 psi and purge feed lines again.
   f. Close high-pressure air valve.
   g. Turn off controller/diagnostic specific power sources.

Figure C.1: Operational Checklist for University of Michigan Supersonic Combustion Laboratory, as of August 5th, 2009.

APPENDIX D

Laboratory Fire

Experiment goes awry on University of Michigan North Campus; lab room fire extinguished

Posted: 10:30 a.m. March 26, 2010

Ann Arbor firefighters extinguished a blaze in a University of Michigan North Campus laboratory Thursday evening.

Firefighters were called to a fire at the Francios Xavier Bagnoud Building at 1320 Beal Ave. at 6:03 p.m., a Fire Department Press release said.

Upon their arrival, a member of the University of Michigan College of Engineering Emergency Response Team led firefighters to the lab room, where seals in a chamber where a student was conducting an experiment had failed, causing a fire, the release said.

Hydrogen and oxygen gasses used to fuel the experiment as well as electrical power sources were turned off and the fire was put out with a chemical fire extinguisher.

Damage was estimated at $1,000, the press release said.

Figure D.1: Article from AnnArbor.com regarding laboratory fire on March 25th, 2010.

149

APPENDIX E
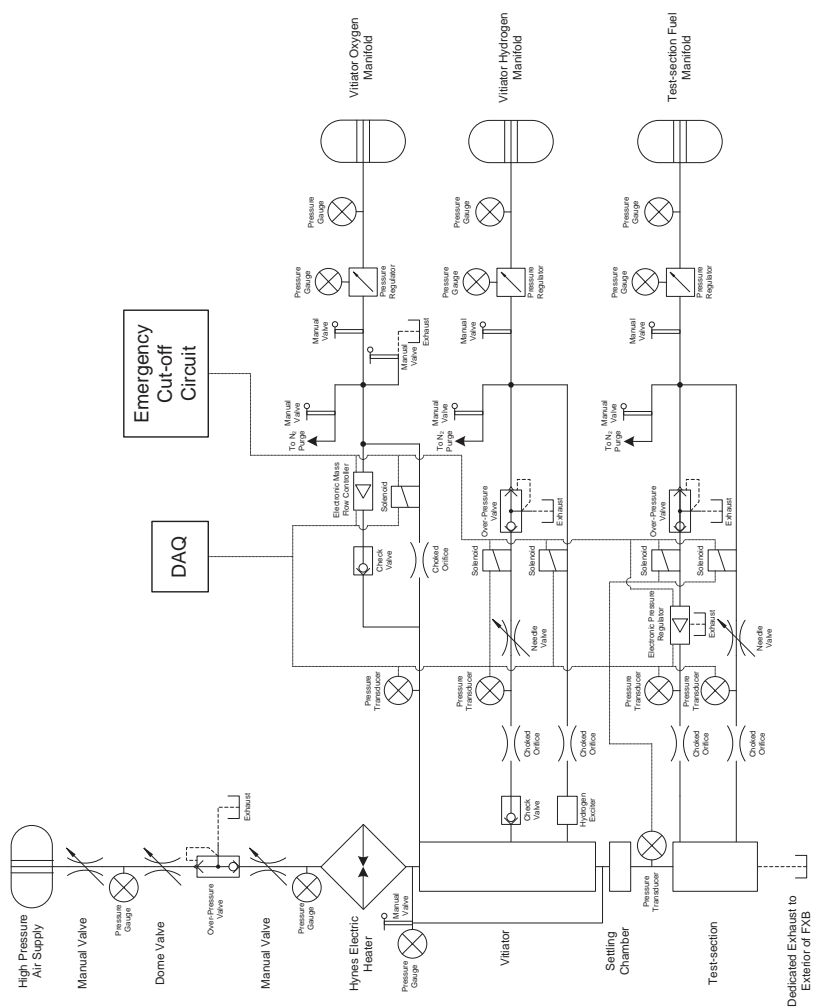
Experimental Flow Control

Figure E.1: Schematic of the flow control arrangement of the University of Michigan Dual-mode Combustor experiment, prior to April 14th, 2010.
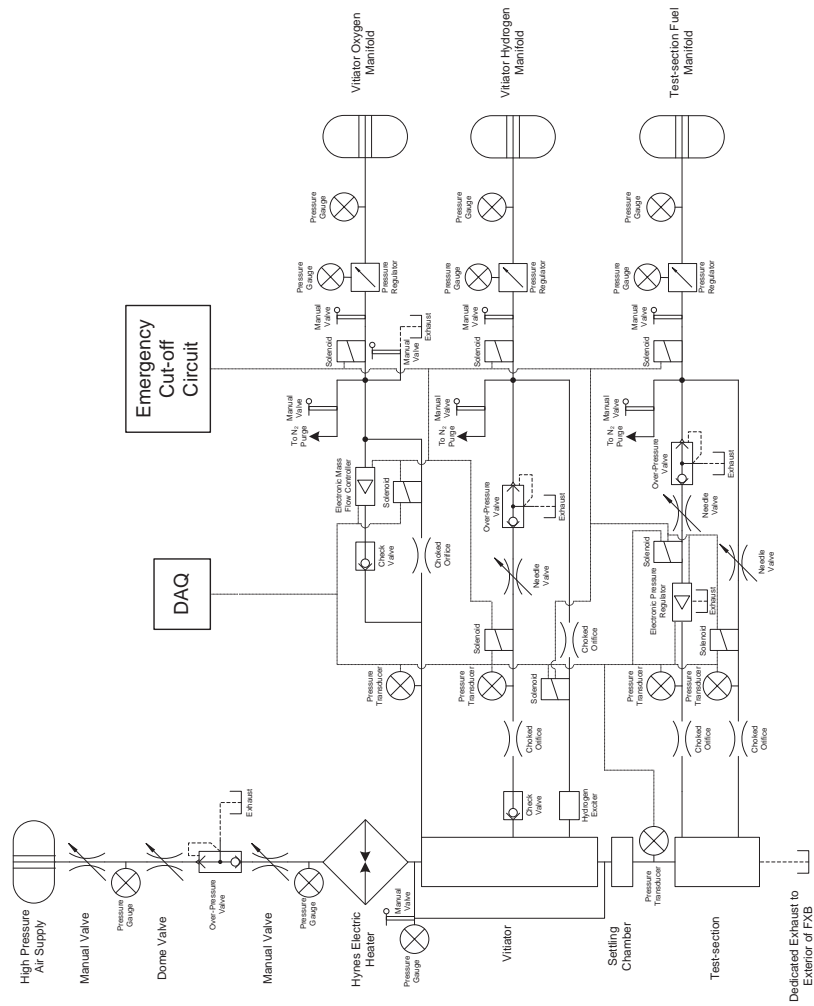
Figure E.2: Schematic of the flow control arrangement of the University of Michigan Dual-mode Combustor experiment, after April 14th, 2010.

BIBLIOGRAPHY

BIBLIOGRAPHY

[1] D. A. Bement, J. R. Stevens, and M. W. Thompson. Measured operation characteristics of a rectangular combustor/inlet isolator. In *AIAA/SAE/ASME/ASEE 26th Joint Propulsion Conference*. AIAA Paper No. 90-2221, 1990.

[2] A. Ben-Yakar, M. G. Mungal, and R. K. Hanson. Time evolution and mixing of hydrogen and ethylene transverse jet in supersonic crossflows. *Physics of Fluids*, 18(026101), 2006.

[3] F. S. Billig. Combustion processes in supersonic flow. *Journal of Propulsion*, 4(3):209–216, 1988.

[4] F. S. Billig. Research on supersonic combustion. *Journal of Propulsion and Power*, 9(4):499–514, 1993.

[5] A. Bryant. *Planar laser-induced fluorescence imaging of fuel mixing and the reaction zone in a supersonic combustor*. PhD thesis, University of Michigan, 1998.

[6] B. F. Carroll and J. C. Dutton. Characteristics of multiple shock wave/turbulent boundary-layer interactions in rectangular ducts. *Journal of Propulsion*, 6(2):186–193, 1990.

[7] B. F. Carroll and J. C. Dutton. Multiple shock wave/turbulent boundary-layer interactions. *Journal of Propulsion and Power*, 8(2):441–448, 1992.

[8] B. F. Carroll and J. C. Dutton. Turbulence phenomena in a multiple normal shock wave/turbulent boundary-layer interaction. *AIAA Journal*, 30(1):43–48, 1992.

[9] J. Chun, T. Scheuermann, J. von Wolfersdorf, and B. Weigand. Experimental study on combustion mode transition in a scramjet with parallel injection. In *14th AIAA/AHI Space Planes and Hypersonic Systems and Technologies Conference*. AIAA Paper No. 2006-8063, 2006.

[10] L. Crocco. *One-Dimensional Treatment of Steady Gas Dynamics*, pages 110–30. Princeton University Press, 1958.

[11] S. Rocci Denis and H.-P. Kau. Experimental study on transition between ramjet and scramjet modes in a duel-mode combustor. In *12th AIAA International Space Planes and Hypersonic Systems and Technologies Conference*. AIAA Paper No. 2003-7048, 2003.

[12] O. Dessornes and D. Scherrer. Tests of the japhar dual mode ramjet engine. *Aerospace Science and Technology*, 9(3):211–21, 2005.

[13] M. L. Fotia and J. F. Driscoll. Isolator-combustor interactions in a direct-connect ramjet-scramjet experiment. *Journal of Propulsion and Power*. Accepted for Publication.

[14] C. P. Goyne, J. C. McDaniel, T. M. Quagliaroli, R. H. Krauss, and S. W. Day. Dual-mode combustion of hydrogen in a mach 5, continuous-flow facility. *Journal of Propulsion and Power*, 17(6):1313–1318, 2001.

[15] M. R. Gruber, R. A. Baurle, T. Mathur, and K.-Y. Hsu. Fundamental studies of cavity-based flameholder concepts for supersonic combustors. *Journal of Propulsion and Power*, 17(1):146–153, 2001.

[16] E. F. Hasselbrink and M. G. Mungal. Transverse jets and jet flames. part 1. scaling laws for strong transverse jets. *Journal of Fluid Mechanics*, 443:1–25, 2001.

[17] E. F. Hasselbrink and M. G. Mungal. Transverse jets and jet flames. part 2. velocity and oh field imaging. *Journal of Fluid Mechanics*, 443:27–68, 2001.

[18] W. H. Heiser and D. T. Pratt. *Hypersonic Airbreathing Propulsion*. Education Series. AIAA, 1994.

[19] W. N. Heltsley, J. A. Snyder, C. C. Cheung, M. G. Mungal, and R. K. Hanson. Combustion stability regimes of hydrogen jets in supersonic crossflow. In *43rd AIAA/ASME/SAE/ASEE Joint Propulsion Conference and Exhibit*. AIAA Paper No. 2007-5401, 2007.

[20] J. P. Holman. *Heat Transfer*. Mechanical Engineering. McGraw Hill, 9th edition, 2002.

[21] H. Huh. *An experimental study of supersonic hydrogen-air flames for scramjet applications*. PhD thesis, University of Michigan, 1996.

[22] T. Ikui, K. Matsuo, and M. Nagai. The mechanism of pseudo-shock waves. *Bulletin of the JSME*, 17(108):731–739, 1974.

[23] T. Ikui, K. Matsuo, and K. Sasaguchi. Modified diffusion model of pseudo-shock waves considering upstream boundary layers. *Bulletin of the JSME*, 24(197):1920–1927, 1981.

[24] ANSYS Inc. Fluent version 12.0.16. Copyright 2009.

[25] C. J. Jachimowski. An analytical study of the hydrogen-air reaction mechanism with application to scramjet combustion. NASA Technical Paper No. 2791, 1988.

[26] T. Kanda, N. Chinzei, K. Kudo, and A. Murakami. Dual-mode operations in a scramjet combustor. *Journal of Propulsion and Power*, 20(4):760–763, 2004.

[27] T. Kanda, N. Chinzei, K. Kudo, A. Murakami, and T. Hiraiwa. Autoignited combustion testing in a water-cooled scramjet combustor. *Journal of Propulsion and Power*, 20(4):657–664, 2004.

[28] D. B. Le, C. P. Goyne, R. H. Krauss, and J. C. McDaniel. Experimental study of a dual-mode scramjet isolator. *Journal of Propulsion and Power*, 24(5):1050–57, 2008.

[29] K. Matsuo, Y. Miyazato, and H.-D. Kim. Shock train and pseudo-shock phenomena in internal gas flows. *Progress in Aerospace Sciences*, 35:33–100, 1999.

[30] W. Merzkirch. A simple schlieren interferometer system. *AIAA Journal*, 3(10):1974–1976, 1965.

[31] W. Merzkirch. Generalized analysis of shearing interferometers as applied for gas dynamics studies. *Journal of Applied Optics*, 13(2):409–413, 1974.

[32] W. Merzkirch. *Flow Visualization*. Academic Press, 2nd edition, 1987.

[33] Inc. Metacomp Technologies. Cfd++ software suite version 8.1.1. Copyright 2006.

[34] D. J. Micka. *Combustion stabilization, structure, and spreading in a laboratory dual-mode scramjet combustor*. PhD thesis, University of Michigan, 2010.

[35] D. J. Micka and J. F. Driscoll. Combustion characteristics of a dual-mode scramjet combustor with cavity falameholder. *Proceedings of the Combustion Institute*, 32:2397–2404, 2009.

[36] D. J. Micka and J. F. Driscoll. Stratified jet flames in a heated (1364 k) cross-flow with auto-ignition. In *49th AIAA Aerospace Sciences Meeting and Exhibit*. AIAA Paper No. 2011-321, 2011.

[37] M. Nakagawa. *Experimental study of compressibility effects on entrainment and mixing in supersonic planar turbulent bluff-body wakes*. PhD thesis, University of Michigan, 2001.

[38] L. D. Nill and A. T. Mattick. An experimental study of weak normal shock-wave/turbulent boundary-layer interactions in internal flows. In *AIAA 34th Aerospace Sciences Meeting and Exhibit*. AIAA Paper No. 96-0799, 1996.

[39] D. Om and M. E. Childs. Multiple transonic shock-wave/turbulent boundary-layer interaction in a circular duct. *AIAA Journal*, 23(10):1506–1511, 1985.

[40] D. Om, J. R. Viegas, and M. E. Childs. Transonic shock-wave/turbulent boundary-layer interaction in a circular duct. *AIAA Journal*, 23(5):707–714, 1985.

[41] C. C. Rasmussen. *An experimental study of flame stability in a directly-fueled wall cavity with a supersonic free stream*. PhD thesis, University of Michigan, 2007.

[42] G. B. Rieker, J. B. Jeffries, R. K. Hanson, t. Mathur, M. R. Gruber, and C. D. Carter. Diode laser-based detection of combustor instabilities with application to a scramjet engine. *Proceedings of the Combustion Institute*, 32:831–838, 2009.

[43] J. E. Rossiter. Wind-tunnel experiments on the flow over rectangular cavities at subsonic and transonic speeds. *Aeronautical Research Council Reports and Memo No. 3438*, 1964.

[44] C. W. Rowley, T. Colonius, and A. J. Basu. On self-sustained oscillations in two-dimensional compressible flow over rectangular cavities. *Journal of Fluid Mechanics*, 455:315–346, 2002.

[45] G. S. Settles. *Schlieren and Shadowgraph Techniques*. Experimental Fluid Mechanics. Springer, 1st edition, 2001.

[46] A. H. Shapiro. *The Dynamics and Thermodynamics of Compressible Flow*. Wiley, 1975.

[47] D. J. Torrez, D. J. Dalle, and J. F. Driscoll. A new method for computing performance of choked reacting flows and ram to scram transition. *Journal of Propulsion and Power*. Submitted for Publication.

[48] J. L. Wagner, K. B. Yuceil, A. Valdivia, N. T. Clemens, and D. S. Dolling. Experimental investigation of unstart in an inlet/isolator model in mach 5 flow. *Journal of Propulsion and Power*, 47(6):1528–1542, 2009.

[49] P. J. Waltrup and F. S. Billig. Prediction of precombustion wall pressure distributions in scramjet engines. *Journal of Spacecraft*, 10(9):620–22, 1973.

[50] P. J. Waltrup and F. S. Billig. Structure of shock waves in cylindrical ducts. *AIAA Journal*, 11(10):1404–08, 1973.

[51] F. M. White. *Viscous Fluid Flow*. Mechanical Engineering. McGraw-Hill, 3rd edition, 2006.

[52] Y. Yoon. *An experimental study of generic supersonic combustor*. PhD thesis, University of Michigan, 1994.

[53] V. L. Zimont and V. N. Ostras. Calculation of pseudo-shocks in a cylindrical duct. *Fluid Mec Soviet Res*, 5(2):78–87, 1979.